Doctoral Dissertations

Graduate School

12-2012

# Computer modeling and signal analysis of cardiovascular physiology

Henian Xia

hxia@utk.edu

To the Graduate Council:

I am submitting herewith a dissertation written by Henian Xia entitled "Computer modeling and signal analysis of cardiovascular physiology." I have examined the final electronic copy of this dissertation for form and content and recommend that it be accepted in partial fulfillment of the requirements for the degree of Doctor of Philosophy, with a major in Biomedical Engineering.

Xiaopeng Zhao, Major Professor

We have read this dissertation and recommend its acceptance:

Jindong Tan, Adam Petrie, Kivanc Ekici, Kwai Wong

Accepted for the Council:
Carolyn R. Hodges

Vice Provost and Dean of the Graduate School

(Original signatures are on file with official student records.)

# Computer modeling and signal analysis of cardiovascular physiology

A Dissertation Presented for the
Doctor of Philosophy
Degree
The University of Tennessee, Knoxville

Henian Xia
December 2012

# ACKNOWLEDGEMENTS

# ABSTRACT

This dissertation aims to study cardiovascular physiology from the cellular level to the whole heart level to the body level using numerical approaches.

A mathematical model was developed to describe electromechanical interaction in the heart. The model integrates cardio-electrophysiology and cardiac mechanics through excitation-induced contraction and deformation-induced currents. A finite element based parallel simulation scheme was developed to investigate coupled electrical and mechanical functions. The developed model and numerical scheme were utilized to study cardiovascular dynamics at cellular, tissue and organ levels. The influence of ion channel blockade on cardiac alternans was investigated. It was found that the channel blocker may significantly change the critical pacing period corresponding to the onset of alternans as well as the alternans' amplitude. The influence of electro-mechanical coupling on cardiac alternans was also investigated. The study supported the earlier assumptions that discordant alternans is induced by the interaction of conduction velocity and action potential duration restitution at high pacing rates. However, mechanical contraction may influence the spatial pattern and onset of discordant alternans.

Computer algorithms were developed for analysis of human physiology. The 12-lead electrocardiography (ECG) is the gold standard for diagnosis of various cardiac abnormalities. However, disturbances and mistakes may modify physiological waves in ECG and lead to wrong diagnoses. This dissertation developed advanced signal analysis techniques and computer software to detect and suppress artifacts and errors in ECG. These algorithms can help to improve the quality of health care when integrated into medical devices or services. Moreover, computer algorithms were developed to predict patient mortality in intensive care units using various physiological measures.

Models and analysis techniques developed here may help to improve the quality of health care.

# TABLE OF CONTENTS

# LIST OF TABLES

# LIST OF FIGURES

# CHAPTER 1
# INTRODUCTION AND LITERATURE REVIEW

## 1.1 Background

The heart is a crucial organ found in every animal with a circulatory system. It pumps blood to the whole body throughout the blood vessels by repeated, rhythmic contractions. The heart beats 100,000 times per day or 2.5 billion times in lifetime. The heart is supported by an electrogenic system for impulses generation and conduction. The rhythmical and conductive system of the heart can be damaged by heart disease. Cardiovascular disease is the leading cause of death in America. Table **1-1** shows the number of deaths for leading causes of death in 2009 in the USA 0. Any disease that affects the cardiovascular system is referred as a cardiovascular disease [2]. It typically involves the heart or the blood vessels, such as the arteries, capillaries and veins [3]. There are various causes of the cardiovascular disease. According to some reports [4]-[8], the nine leading causes are smoking/tobacco use, alcohol use, diet, physical inactivity, obesity, diabetes, high cholesterol, high blood pressure, and heredity, among which the first five are lifestyle or behavioral causes and the last four are health causes. Various types of cardiovascular diseases exist, such as the coronary heart disease, the cardiomyopathy, the hypertensive heart disease, the heart failure, the cor pulmonale, the cardiac dysrhythmias, the inflammatory heart disease, the valvular heart disease, the stroke and cerebrovascular disease, the peripheral arterial disease, and so on.

Although the mortality rate of cardiovascular diseases has declined significantly in some developed countries because of the improvement of the healthcare ability, the cardiovascular disease has increased fast in a lot of developing countries [9]. In addition to the mortality risk increased by the cardiovascular diseases, the cardiovascular diseases can also decrease the patient's life quality a lot. For example, the patients who have cardiovascular diseases must not get too excited.

Table 1-1: Number of deaths for leading causes of death in the US in 2009

| Cause of death | Number of death |
|---|---|
| **Heart disease** | **599,413** |
| Cancer | 567,628 |
| Chronic lower respiratory diseases | 137,353 |
| Stroke (cerebrovascular diseases) | 128,842 |
| Accidents (unintentional injuries) | 118,021 |
| Alzheimer's disease | 79,003 |
| Diabetes | 68,705 |
| Influenza and Pneumonia | 53,692 |

Due to the seriousness of the cardiovascular diseases and the importance of finding new ways to understand, to diagnose, or to treat them, I have devoted my PhD study to the investigations around the cardiovascular diseases.

The cardiovascular diseases have been studied from two aspects in this dissertation. In the first aspect, the study is focusing on the understanding of the mechanisms of the cardiac dysrhythmias, an important type of cardiovascular disease, through computer simulations. To this aim, a new model has been constructed. Compared to previously existing models, the model developed in this dissertation is more comprehensive, more realistic and more computationally efficient and scalable. Analysis is performed at cellular, tissue and organ levels using this model. In the second aspect, the study is focusing on the electrocardiography (ECG) signal analysis and related problems. The ECG signal is a very important tool for understanding and diagnosing the cardiovascular diseases. In this dissertation, several important issues about the ECG signal are tackled, such as the automatic evaluation of the quality of a 12-lead ECG record, the automatic detection of the electrode misplacement during ECG signal collection, etc. A related problem is also tackled in this dissertation, which is the mortality prediction in intensive care units (ICU). Two important types of ICUs are the coronary care unit and the cardiac surgery recovery unit. So it will make big impact on the decreasing of the cardiovascular mortality if the healthcare quality provided by the ICU can be improved. Moreover, the algorithms developed in the ICU mortality prediction problem can be effectively used in the ECG signal analysis.

## 1.2 Computer simulation of heart dynamics

### 1.2.1 Cardiac model

Computer simulation and visualization of complicated dynamics of the heart has great potentials to provide quantitative guidance for diagnosis and treatment of heart problems. The heart is a complicated electro-mechanical system. It weighs 11 ounces and has a size of a fist. The heart beats 100,000 times per day or 2.5 billion times in lifetime. Figure **1**-**1** shows a scheme of the heart. There have been intensive research efforts on developing accurate computer models to advance the understanding on the mechanisms of cardiovascular dynamics [10].

Inspired by the pioneering work of Hodgkin and Huxley [11] many mathematical models have been developed [12]. Meanwhile, a variety of mathematical models have been proposed for electromechanical simulations. Nash and Panfilov [13] presented a computational framework to couple a three-variable FitzHugh–Nagumo-type [14] excitation-tension model to governing equations of non-linear stress equilibrium employing the electromechanical and mechanoelectric feedback. Niederer et al. [15] quantitatively characterized the binding of Ca2+ to TnC, the kinetics of tropomyosin, the availability of binding

sites, and the kinetics of crossbridge binding after perturbations in sarcomere length. Gurev et al. [16] illustrated methods to construct finite element electromechanical models of heart and to develop anatomically accurate ventricular mesh based on magnetic resonance and diffusion tensor magnetic resonance imaging of the heart. The work of [16] focused on the construction of the ventricular meshes, and didn't consider the influence of the mechanical contraction on the cardiac electrophysiology. Göktepe and Kuhl [17] proposed an implicit and entirely finite element-based approach to the two-way coupled excitation–contraction problem. The electrophysiology was described by a FitzHugh–Nagumo-type (FHN) model in [17]. Doyle et al [18] applied the parallel computing to the simulation of heart mechanics. They assessed the model's performance using an unstructured mesh, and they achieved the maximum speed-up factor as 15.9 when using 32 threads. Lafortune et al [19] developed a parallel electromechanical model of the heart. Their model could run efficiently in hundreds of processors using a ventricular mesh of realistic geometry. Lafortune et al described the electrophysiology by the simple three-variable FitzHugh–Nagumo-type (FHN) model [14] or the three-variable Fenton–Karma (FK) model [20] and employed a "one-way coupling" in which the displacements don't affect the electrophysiology. Moreover, the influence of the heart's mechanical environment on its electrical behavior, which is termed as the mechano-electric feedback, has drawn researchers' attention [21]-[24]. This feedback can be through the stretch-activated channels or through the effect of stretch on the electrical signal propagation.
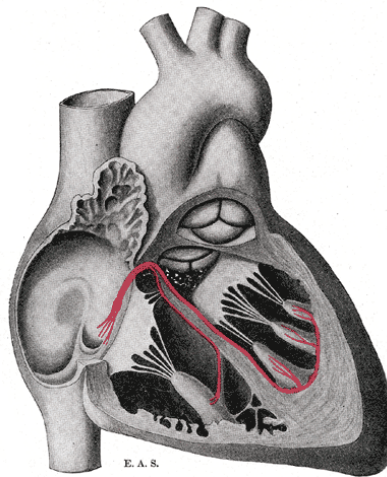


Figure 1-1. Scheme of the heart: electrical signals are generated at the sinus node; then it quickly propagates through the atrium; then it travels to the ventricle. Electrical signals induce cell depolarization and then the mechanical contraction. Image copied from [25]

### 1.2.2 Influence of ion channel blockade

According to the American Heart Association, the sudden cardiac arrest (SCA) kills over 350,000 Americans each year. The SCA is commonly caused by the random reentry that happens in the ventricles, called ventricular fibrillation (VF) [26], an arrhythmia caused when rapid, erratic electrical impulses make the ventricles fail in pumping blood. VF is frequently initiated by the ventricular tachycardia (VT) [27]. VT occurs when sustained spiral waves happen in the ventricular muscle, which are often caused by abnormal spontaneous activities like unexpected stimuli or premature impulses [28]; the breakup of such sustained spiral waves causes the VF [26]. As seen in [28], instead of radial propagation, the impulse of the premature beat was spread in a circular pathway and was maintained during tachycardia even in a small area of atrial muscle without anatomical obstacle. Premature impulses that happen during the vulnerable period (VP) can be pretty dangerous [27]. The VP is the moment that the heart is recovering from the previous cardiac cycle, when areas of refractoriesness and nonrefractoriness are likely to exist simultaneously in the heart muscle. Because of the heterogeneity of the heart muscle during the VP, impulses will spread successfully in some directions, while failing to spread in other directions, and thus can lead to spiral waves. If different regions of the heart stay in VP non-simultaneously, reentry is very probably to be induced, but if the VP is long enough relative to the conduction velocity so that a zone has not recovered from the VP before a premature impulse reaches it, the reentry might be avoided [29]. Consequently, drugs that can prolong the refractory period of a cardiac cell were assumed to be anti-arrhythmic because they reduced the likelihood of reentry [30]-[31]. For example, people have long used sodium channel blockers, which can effectively prolong the VP, to treat atrial fibrillation [32]. However, instead of being anti-arrhythmic, significant pro-arrhythmic properties of such drugs were observed in two clinical trials, in which the incidence of VF was remarkably increased in patients who were treated with drugs that primarily blocked sodium channels [33]-[34].

The pro-arrhythmic properties of such anti-arrhythmic drugs for atria fibrillation (AF) are caused by their unexpected effects on the ventricles. But the VP is also prolonged by the sodium channel blockers in ventricles [35]. So here emerges the question: why does the drug facilitate the arrhythmias in ventricles even though the VP is prolonged and thus the premature contraction is suppressed? This question will be addressed later in the dissertation. The idea is to look into the electrophysiological dynamics of heart tissues, to which much attention has been paid [36]-[37]. When stimulated by an electrical signal, cardiac cells generate an action potential, which consists of a rapid depolarization of the transmembrane voltage followed by a much slower repolarization process before returning to the resting value. The time interval during which the voltage is elevated is called the action potential duration (APD). The time between the end of an action potential to the beginning of the next one is called the diastolic interval (DI). The time interval between two consecutive stimuli is called the basic

cycle length (BCL). Under periodic stimuli, the steady-state response gives rise to a 1:1 pattern when the pacing rate is slow. When the pacing rate becomes sufficiently fast, the 1:1 pattern may be replaced by the 2:2 pattern, or the electrical alternans, where the APD alternates between short and long values. Figure **1**-**2** demonstrates the APD alternans. A causal link between alternans and ventricular fibrillation has been established by various authors in theory and experiments [38]-[40]. In particular, during spatially discordant alternans, the APD alternates out of phase in different regions of the heart, which significantly increases dispersion of refractoriness and makes ectopic beats induce reentry easier [41]. Therefore, studying the electrical alternans is a crucial step in understanding fatal arrhythmias.

### 1.2.3 Electro-mechanical coupling and cardiac alternans

It is well considered that the APD alternans is the underlying mechanism for the ECG T wave alternans (TWA) [42]. The TWA of large amplitude is suggested to be highly correlated with sudden cardiac arrest by clinical studies [43]-[44]. A relationship between discordant alternans associated with TWA and arrhythmias induction is demonstrated by [45]. When the discordant alternans is present, a small acceleration of pacing rate may produce a sequence of events: the unidirectional block of an impulse propagating against steep gradients of repolarization, the reentrant propagation and finally the initiation of the VF. Two mechanisms for the discordant alternans are demonstrated in [42] by one and two dimensional simulations of action potential propagation models in spatially homogeneous tissues. The first and the more important mechanism was the interaction of conduction velocity and action potential duration restitution at high pacing rates, and the second was the dispersion of diastolic interval produced by ectopic foci.
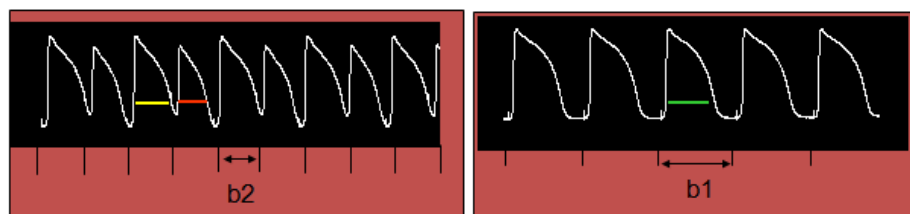


Figure 1-2: APD Alternans: Left figure shows the high heart rate (smaller pacing period) resulting APD alternans (2:2), right figure shows the low heart rate (larger pacing period) and resulting normal response (1:1)

As demonstrated in [42], when discordant alternans was caused by the first mechanism, boundaries that marked the regions of alternans with opposite phase first appeared far from the stimulus site. As simulations continued, the boundaries would move toward the stimulus site and gradually stabilize, and multiple boundaries could be induced by larger tissues and faster pacing rates. The formation of boundaries may also be facilitated or inhibited by inhomogeneity of tissue properties. It was also demonstrated in [42] that the restitution curves could dynamically split due to electrotonic coupling, and the split played a crucial role in the stability.

Despite the thorough studies for the mechanisms of discordant alternans by electrophysiological simulations, no effects of the electro-mechanical coupling have been considered so far. The mechanoelectrical feedback (MEF), a complex phenomenon studied in the clinical community for over a century, may have both pro-rhythmic and arrhythmogenic effects [46]. Stretch was shown to change the action potential, to induce stretch-activated arrhythmias, and to increase the rate of beating of the sino-atrial node. Previous researches reveal that ventricular stretch causes a shortening of APD and of the effective refractory period (ERP) [47]. In response to the stretch, the $Ca2+$ extrusion via $Na+/Ca2+$ exchange can be attenuated and the $Ca2+$ may also enter myocardium through stretch-activated channels [48]. This increase of intracellular calcium concentration could promote $Ca2+$ oscillations [49] and electrophysiological oscillations, leading to arrhythmia. On a larger scale, mechanical contractions, activated by cardiac waves, can regulate the electrical propagation in the heart which is of great importance to the formation of the arrhythmias. Mechanical external stresses may lead to cardiac instabilities too. They can either promote sudden cardiac death or cardiovert potentially lethal arrhythmias [50]. Various authors also observed that the mechanoelectrical feedback may be enhanced under pathological conditions [51]-[52]. In this dissertation, the effects of the electro-mechanical coupling on the formation of the APD alternans will be carefully examined.

## 1.3 Biomedical informatics and telemedicine

### 1.3.1 Electrode misplacement during ECG collection

Rhythmic contractions of the heart are driven by propagating electrical waves, which, when manifested on the surface of the body, is known as electrocardiography or ECG [53]. ECG can provide abundant information about the heart's activities and thus can be used to detect almost all severe abnormalities of the heart, including heart attack, inflammation, angina, and arrhythmias [27]. ECG is also used to diagnose how well medicines or mechanical devices are working and how the health of heart is influenced by conditions such as high blood pressure, high cholesterol, cigarette smoking, diabetes, and a family history of early heart disease. The 12-lead ECG has

6

become the gold standard for diagnosis of normal cardiac rhythm, arrhythmias, and myocardial ischemia [54].

It is estimated that 0.4% - 4% of all ECGs are taken with misplaced electrodes [55]. Since about 40 million ECGs are recorded annually in the United States [56], it follows that hundreds of thousands of ECGs are incorrectly recorded each year. Furthermore, mistakenly collected ECGs may mislead doctors in diagnosis. For example, a recent study at two hospitals in Switzerland [57] challenged 29 physicians from the two institutes to interpret an ECG of a healthy individual collected with the right arm-left leg electrode interchanged. Cable switch was only suspected by less than half of the doctors (13 or 45%). In contrast, eight doctors (28%) mistakenly diagnosed the ECG as supraventricular arrhythmias and nine doctors (31%) as cardiac ischemia.

Electrode placement is considered one of the most important factors that determine ECG signal quality [58]-[60]. Cable misplacements may result in ECGs that mimic various cardiac abnormalities such as ectopic rhythm [61], intraventricular conduction disturbance [62]-[63], chamber enlargement or ventricular pre-excitation [64]. Misplacements can also simulate [65]-[68] or conceal [69] myocardial ischemia or infarction.
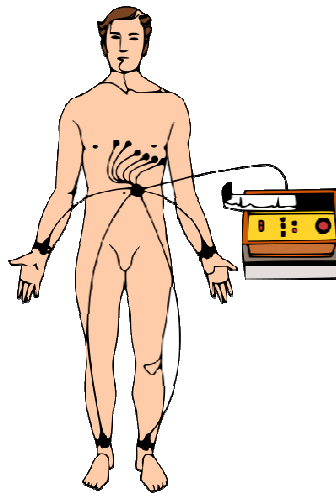


Figure 1-3: 12-lead ECG: a patient is connected to 10 electrodes for a 12-lead ECG. Image is from http://en.wikipedia.org/wiki/Electrocardiography

The standard 12-lead ECG is obtained using 10 electrodes, including 4 limb leads and 6 precordial leads [54]. Figure **1**-**3** shows a patient who is connected to 10 electrodes for collecting the 12-lead ECG. The four limb electrodes are labeled as RA, LA, RL, and LL, which are supposed to be placed on the right arm (r.a.), left arm (l.a.), right leg (r.l.), and left leg (l.l.), respectively. The arm electrodes (RA and LA) can be placed anywhere on the arms but should avoid thick muscle and should not touch the thorax. The leg electrodes (RL and LL) are best placed on the lateral calf muscle of the legs. The six precordial chest electrodes (V1 to V6) are placed at anatomically referenced landmarks on the anterior chest. Figure **1**-**4** shows examples of selected electrode placements among which one is correct and the other two are mistaken. The placement of the electrodes is crucial since the ECGs resulting from interchanged leads may result in a wrong diagnosis [61]-[62].

The reversal between the LA and RA electrodes is the most common electrode placement error, and many ECG recorders have built-in logic to recognize this problem [70]. Early algorithms use rule-based criteria to detect the reversal between LA and RA [71]-[72]. For example, the Marquette program suspects LA-RA interchange "if the QRS axis is between 90 and 270 degrees and the P axis is between 90 and 210 degrees" [72]. While the Marquette program yields accurate results (93.91% sensitivity and 100% specificity) for ECGs with clear P waves, the results are disappointing (39.34% sensitivity and 100% specificity) for ECGs without P waves [73]. Since then, a few algorithms have been developed for different types of electrode misplacement [73]-[78]. The recent review by [61] provides a systematic review and comparison of various algorithms.
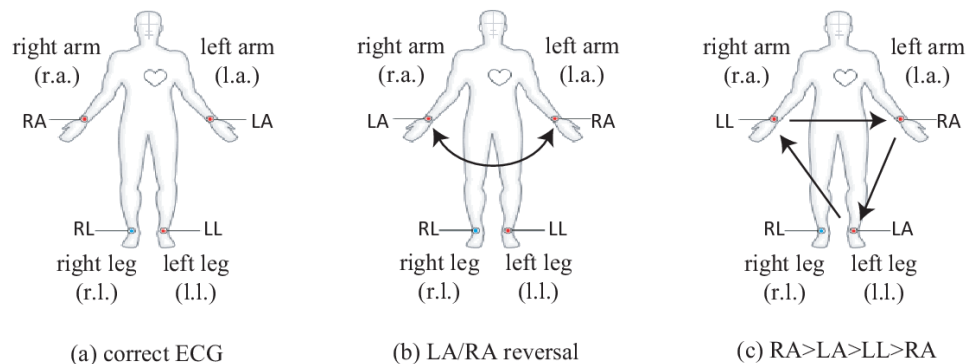


Figure 1-4: Examples of selected electrode placements: (a) the correct ECG; (b) the reversal between LA and RA electrodes; and (c) a misplacement, where RA takes the position of LA, LA takes the position of LL, and LL takes the position of RA.

In this dissertation, two well-developed algorithms will be compared and a new algorithm combining the two will be developed and evaluated. Also this dissertation will investigate automatic detection of electrode misplacement under scenarios mimicking clinical setting.

### 1.3.2 Evaluation of ECG quality

It's well known that ECG is susceptible to artifacts, which may be caused by various physiological and non-physiological sources [79]. Common physiological artifacts include muscular activities, manifested by small spikes, and patient motion, manifested by large swings. Non-physiological artifacts include electromagnetic interference by electrical devices as well as cable and electrode malfunction. Examples of malfunction include insufficient amount of electrode gel, fractured wires, inappropriate filter settings, loose connections, electrode placement error, and accumulation of static energy. It is estimated that about 4% of all ECGs are recorded with incorrect lead placements [80].

It is of great clinical challenge and significance to differentiate ECG artifacts from patterns of diseases. Poor ECG signal quality can increase the number of false alerts [81], may degrade diagnostic information [82] and can increase workload of physicians [83]. Wrong diagnosis from inaccurate ECG data may delay proper treatment or cause a wrongful, detrimental treatment [84]. For example, [69] showed that reversal of the left arm and left leg leads may produce ECG signs of inferior ischemia in normal people whereas such reversal may produce normal ECG without signs of ischemia in patients with ischemic heart diseases. Moreover, the misplacement errors were not detected by the automatic ECG analyzer [69]. Artifacts from electrode misplacement errors are frequent and hard to detect. A survey by [55] showed the frequency of electrode misplacement for ECGs is significantly higher at intensive care units (ICU) than at the outpatient clinic. The higher rate of artifacts at ICU may be due to the fact that nurses and doctors in the ICU have less experience in recording ECGs and suffer a higher workload and more distractions [55].

A computer algorithm that can automatically determine whether an ECG record's quality is good will be developed in this dissertation. Moreover, when a record is decided to be unacceptable, the algorithm may also give advice as to how to correct the problems. This algorithm has potential applications in telemedicine and can help to improve the performance of such devices.

### 1.3.3 Cloud ECG

In many countries, the increasing longevity and declining fertility rates have contributed to aging populations and thus increased medical needs [85]. If health care could be provided remotely and the patient could be monitored continuously without having to go to hospitals, expensive medical costs could be saved. Moreover, there is a large population that does not receive good health care because they live in rural communities, particularly in developing countries.

9

Their health care quality could be improved if the doctor could be "brought" to their home through the help of telecommunication technologies.

In this direction, biomedical engineers are interested in developing a distributed computing system that will collect people's medical data and store it securely in a web server [86]. Towards this aim, new techniques and concepts are proposed, such as Body Area Network (BAN) and cloud computing. Jones et al. [87] developed a BAN and investigated its potentials for management of chronic conditions and detection of health emergencies. The BAN was composed of a central unit called MBU (mobile base unit) and a set of body-worn devices including sensors, actuators, etc. The MBU was responsible for local computations, communication amongst BAN devices and communication with remote servers. The m-health service platform was developed on remote servers or workstations, and handled BAN registration, BAN discovery, BAN data storage, BAN data monitoring, etc. They have tested the system in remotely monitoring patients with ventricular arrhythmia and women with high-risk pregnancies, etc.

The cloud computing has gained more and more popularity in recent years [88]. A cloud-based health care provider bears many important features [89]. First, it can be accessed using any device such as a web browser or a mobile phone from anywhere. Users no longer need to install the software at their local machines. Second, the cost for cloud-computing is greatly reduced based on the pay-per-usage scheme. Regarding the costs of using utility grids such as the Amazon EC2 cloud and the Amazon S3, Deelman et al. [90] studied the tradeoffs between cost and performance when using different execution and resource provisioning plans on the Amazon cloud. They found that the cost could be remarkably reduced without significantly influencing the performance by providing the right amount of storage and compute resources. Third, computing resources are provided in an elastic way so that additional resources will be automatically provided only when they are needed, which is often referred to as the horizontal scalability. Besides, the cloud computing system is designed to be geographically scalable, which means the performance and usefulness of the system can be maintained regardless of the geographic pattern. Fourth, development and maintenance of cloud software has become ever so much easier, more reliable, and safer. Although the cloud computing has advantages in lots of aspects, there are still challenges. The greatest challenge was security, according to a survey [91] of 263 IT executives in 2009 conducted by International Data Corporation (IDC). Measures suggested [92] will be ensured to be taken by cloud providers. For example, data should be prevented from being accessed by unauthorized users; data should be properly encrypted for segregation; data should be regularly replicated so that they could be recovered in case of disaster.

Several cloud based health care systems have been proposed in previous publications. Hoang and Chen [93] proposed a Mobile Cloud for Assistive Healthcare (MoCAsH) as an infrastructure for assistive healthcare. McGregor et al [94] presented a web service framework which enables real-time physiological data transmission for local and remote Neonatal Intensive Care. They later developed a cloud computing based Software-as-a-Service and Data-as-a-Service approach for remote real-time patient monitoring and support for clinical research and a neonatal intensive care unit case study was provided for demonstration.

Pandeya et al. [95] designed a scalable and economical cloud-based system for hosting ECG analysis services. It was designed to collect ECG data from mobiles and then to transmit the data to remote servers for simple analyses. A prototype system was developed for demonstration. However, significant obstacles still remain before such system could be applied in practical use. One big challenge is regarding the usefulness of the ECG data collected. As introduced in previous sections, the ECG data is often disqualified by artifacts and electrode misplacements, especially if the person who collects the data is not well trained. In this dissertation, a cloud-based system for real time ECG monitoring and analysis will be developed. Previously developed algorithms for ECG enhancement, ECG quality evaluation and ECG parameter extraction will be implemented in the system.

### 1.3.4 ICU mortality prediction

An intensive care unit (ICU) is a special department of a hospital for patients with the most serious diseases or injuries. Most patients in an ICU need support from equipment like the medical ventilator to maintain normal body functions. Normally they are also constantly and closely monitored. For decades, the number of ICUs has increased worldwide [96] because of their capabilities of reducing the mortality rate for patients in critical situations. However, while the intensive care improves the outcome for seriously ill patients, it comes with an expensive cost. In 2005, the mean intensive care unit cost is as high as 31,574±42,570 dollars for patients requiring mechanical ventilation and 12,931±20,569 dollars for those not requiring mechanical ventilation [97].

During the ICU stay, different types of physiological parameters are measured and analyzed. Those parameters can be used in scoring systems to gauge the severity of the patients. By providing evaluation of patients' situations, the intensive care can be restricted to patients most at need. Also the evaluation gives doctors a way to judge the treatment method. If a cure method leads to a significant decrease in the mortality rate, it might be considered as an effective; otherwise the doctor should consider other methods.

Many types of scoring systems have been developed, such as the acute physiology and chronic health evaluation (APACHE) system [98], the APACHE II

11

[99], the simplified acute physiology score (SAPS) [100], the mortality probability model (MPM) [101] and so on.

Let's take the APACHE II [99] as an example. The APACHE II system calculates a score from 12 routine physiological measurements. These measurements include the blood pressure, body temperature, heart rate, etc. Only measurements obtained during the first 24 hours after admission are considered. An integer score from 0 to 71 will be computed, and higher scores represent more severe diseases. Similarly, the SAPS [100] scoring system uses 14 easily measured biologic and clinical variables. The MPM [101] model consists of 5 variables measured at the time of admission and 8 variables measured every 24 hours. This model performs particularly well on the good-of-fit tests.

Most of those systems were developed using linear regression over a score computed from physiological variables. For example, the SAPS II examined 37 variables, and chose 17 that were found to be associated with the hospital mortality most significantly. The 17 variables include 12 physiology variables, age, type of admission (scheduled surgical, unscheduled surgical, or medical), and three underlying disease variables (acquired immunodeficiency syndrome, metastatic cancer, and hematologic malignancy). A score is computed using the 17 variables and is converted to a probability of hospital mortality using a linear regression equation.

More recently, the data mining techniques have been proved to be useful in the ICU mortality prediction [102]-[103]. The data mining techniques are used to discover patterns hidden in large clinical data [104]. The volume of clinical data is increasing every single day. It is difficult for human experts to extract information from the data by looking at them manually. In contrast, the data mining techniques can automatically extract information from the raw data [105].

Among the different types of data mining techniques, the artificial neural network is one of the most successful methods. It is widely used because of its capabilities like nonlinear learning, multi-dimensional mapping and noise tolerance [107]. Previous studies reported that the neural network models were better than [102][103][107] or at least similar to [108] the linear regression models.

In this dissertation, a scoring system using data collected during the first two days of an ICU stay based on artificial neural network will be developed and evaluated.

# CHAPTER 2
# A FULLY COUPLED MODEL FOR ELECTROMECHANICS OF THE HEART

## 2.1 Overview

In this chapter, a fully coupled electromechanical model of the heart will be presented. The model integrates the cardiac electrophysiology and the cardiac mechanics through excitation-induced contraction and deformation-induced current. The coupled equations will be numerically solved by an implicit, finite element-based approach. Simulations will be performed on a thin cardiac tissue and a dog ventricle with realistic geometry to test the model. The scaling ability of the model in a distributed computing system will also be investigated.

## 2.2 Physiological models

Hearts beats are the result of a sequence of electrochemical excitation waves that are initiated from the sinoatrial node. The electrical impulses induce intracellular calcium cycling, which in turn causes heart muscle to contract. This process, known as excitation-contraction coupling (ECC), is essential to understanding of the heart. On the other hand, mechanical changes that response to neural and hormonal influences also impact on the electrical properties. This complementary concept is called mechano-electric feedback. See Figure **2**-**1** for the relation between electrical activation, chemical homeostasis, and mechanical contractions.
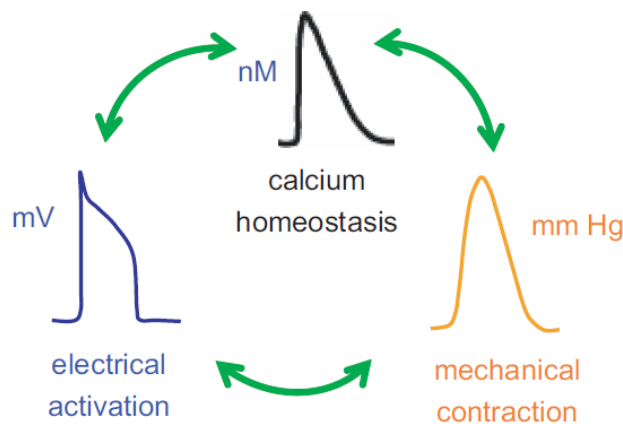


Figure 2-1: Schematic representation of the coupling between electrical, chemical, and mechanical functions of the heart

### 2.2.1 Cardiac electrophysiology

Dozens of models have been proposed over years to simulate cardiac electrophysiology [12]. Most of those models are drawn from the pioneering work of Hodgkin and Huxley [11]. In this work, the Beeler-Reuter (BR) model [109] is adopted for numerical illustrations. The transmembrane voltage is governed by the following equation:

$$\frac{dv}{dt} = -(1/C_m)(I_{Na} + I_{K1} + I_{x1} + I_{Ca} + I_{sac} - I_{stim}) \tag{2.1}$$

In Equation 2.1, $v$ represents transmembrane voltage, $C_m$ represents membrane capacity, $I_{stim}$ represents external stimulation, $I_{sac}$ represents the stretch-activated channel, and ionic currents considered include $I_{Na}$, $I_{K1}$, $I_{x1}$, and $I_{Ca}$. Note that the original BR model does not include stretch-activated channel, details of which will be discussed later. The stimulus current $I_{stim}$ is selected to be a square wave pulse of -80μA/μF for 1ms for each stimulation. The voltage-gated current $I_{Na}$ is represented as follows:

$$
\begin{aligned}
I_{Na} &= (\overline{G_{Na}}m^3hj + G_{N_aC})(v - E_{Na}) \\
\frac{dm}{dt} &= \alpha_m(1 - m) - \beta_m m \\
\frac{dh}{dt} &= \alpha_h(1 - h) - \beta_h h \\
\frac{dj}{dt} &= \alpha_j(1 - j) - \beta_j j
\end{aligned}
\tag{2.2}
$$

In Equation 2.2, $v$ is the membrane potential; m, h and j are voltage-dependent gate parameters; $\overline{G_{Na}}$ is the fully activated sodium conductance and $G_{N_aC}$ is the background sodium conductance; $E_{Na}$ is the $Na^{2+}$ equilibrium potential; $\alpha_m$, $\beta_m$, $\alpha_h$, $\beta_h$, $\alpha_j$ and $\beta_j$ are parameters that are dependent on the voltage. See [109] for detailed descriptions for these currents.

The cardiac electrophysiology is modeled using the reaction-diffusion equation:

$$\frac{\partial v}{\partial t} + \frac{I_{ion}}{C_m} - \nabla_x \cdot (D \cdot \nabla_x v) = 0 \tag{2.3}$$

In Equation 2.3, x represents the spatial coordinate of each material point in the heart; $D$ is the diffusion tensor, which controls the transduction orientation and speed of the electrical wave of excitation in the cardiac tissue; $C_m$ is the membrane capacitance and is set as 1μF/cm.

### 2.2.2 Cardiac mechanics

We denote the initial configuration (diastole) of the heart by Ω0 and the deformed configuration (systole) by Ω. The position vector of a material point in

the initial configuration is given by $X = X_i e_i$, where $e_i$ are the unit base vectors of a rectangular Cartesian coordinate system. Denote the position of the material point X at time t by $x = x_i e_i$. Then, the spatial coordinate of a material point X can be represented by $x = \Phi(X, t)$. The function $\Phi$ can be regarded as a map between the initial configuration and the configuration at time t. The two measures, $x$ and $X$, are related by the deformation gradient, as shown in Equation 2.4.

$$F = \frac{\partial x}{\partial X} \tag{2.4}$$

There are two approaches in describing the deformation of a continuum: the Lagrangian description uses the material coordinates $X$ as independent variables and the Eulerian description uses the spatial coordinates $x$ as independent variables [110]. The Eulerian description is often adopted for fluid dynamics. In this work, the Lagrangian description approach is utilized. There are two formulations for the Lagrangian approach: total Lagrangian formulation and updated Lagrangian formulation. In the total Lagrangian formulation, equations are discretized with respect to the original configuration. In contrast, the updated Lagrangian formulations are based on the current configuration, and is commonly used for nonlinear, large deformations. Thus we use the updated Lagrangian formulation in this work.

For each time step $\Delta t$, the displacement of a material point, denoted by $u(X, t)$, is defined by the difference between its current position and its previous position (Equation 2.5). The displacement $u(X, t)$ is governed by the equilibrium of the linear momentum, and the equation is described as Equation 2.6. In Equation 2.6, $\sigma$ is the Kirchhoff stress tensor; $b$ accounts for the body force or externally applied stresses. The Kirchhoff stress $\sigma$ is composed of a passive component $\sigma_{pass}$ and an active component $\sigma_{act}$. The active force $\sigma_{act}$ is generated from the electrical excitation and will be explained later in detail. The passive component $\sigma_{pass}$ is determined by the equation of the elementary mechanics (Equation 2.7). In Equation 2.7, $\chi = 0.5 MPa$ and $\zeta = 0.2 MPa$ are the Lame constants which govern the isotropic stress response; $\xi = 0.1 MPa$ represents the passive stiffness of myofibers. The left Cauchy-Green tensor is denoted as $p$, and is defined as Equation 2.8. The parameter values were referred to the work of Nash and Panfilov (2004) [13] and Göktepe and Kuhl (2010) [17].

$$u(X, t) = \Phi(X, t) - \Phi(X, t - \Delta t) \tag{2.5}$$
$$\nabla_x \cdot \sigma + b = 0 \tag{2.6}$$
$$\sigma_{pass} = \left(\frac{\chi}{2} \ln A - \zeta\right) + \zeta p + 2\delta\xi(B - 1)\kappa \tag{2.7}$$
$$p = FF^T \tag{2.8}$$

Let us denote the local orientation of a myofiber at initial configuration by a unit vector $a_0$ and that at deformed configuration by vector $a$. In Equation 2.7, $\kappa$

represents the deformed structural tensor and is defined as Equation 2.9. In Equation 2.9, $\kappa_0$ is the structural tensor at initial configuration. The structural tensors $\kappa_0$ at initial configuration and $\kappa$ at deformed configuration represent dominating directions in a specified neighborhood of a node [111]-[112].

$$\kappa = a \otimes a = F\kappa_0 F^T \tag{2.9}$$

In Equation 2.7, the symbol $\delta$ denotes the coefficient that determines whether or not the stiffness of the myofibers is in effect. It indicates that when there is stretch at a material point, $\delta$ will be 1, otherwise it is 0. Mathematically, it's defined as Equation 2.10. In Equation 2.10, $|a|$ represents the stretch at a material point of the heart. At initial configuration, $|a_0| = 1$, while at deformed configuration, there may be stretch at some material points that causes $|a| > 1$. Moreover, the scalars A and B in Equation 2.7 are defined as Equations 2.11.

$$\delta = \begin{cases} 1, & \text{if } |a| > 1 \\ 0, & \text{otherwise} \end{cases} \tag{2.10}$$

$$\begin{cases} A = \det(F^T F) \\ \quad B = |a|^2 \end{cases} \tag{2.11}$$

### 2.2.3 Electromechanical coupling

In summary, the coupled problems are governed by the following equations:

$$\begin{cases} \frac{\partial v}{\partial t} - \nabla_x \cdot (D \cdot \nabla_x v) + \frac{I_{ion}}{C_m} = 0 \\ \qquad \nabla_x \cdot \sigma + b = 0 \end{cases} \tag{2.12}$$

$$\begin{cases} \frac{\partial v}{\partial n} = \nabla_x \cdot n = 0 \\ \qquad \sigma \cdot n = 0 \\ \qquad x = \bar{x} \end{cases} \tag{2.13}$$

Equations 2.12 show the full coupling of the cardiac electrophysiology and the cardiac mechanics. The membrane potential and the spatial coordinates of each node are solved simultaneously from Equations 2.12. The first equation of Equations 2.13 represents the no-flux boundary condition imposed on the surface domain of the heart denoted by $\partial\Omega$. The symbol n is the outward surface normal on $\partial\Omega$. The second equation of Equations 2.13 defines the natural boundary condition imposed on $\partial\Omega$. The third equation of Equations 2.13 shows the essential boundary condition imposed at points which are fixed to ensure that the mechanical problem is well defined. The domain where the essential boundary condition is imposed on is denoted by $\partial$.

In section 2.2, we introduced the active Kirchhoff stress $\sigma_{act}$. $\sigma_{act}$ is generated by the excitation induced contraction. From the perspective of

geometry, the direction of the active Kirchhoff stress should be determined by the structural tensor $\kappa$, and its magnitude is controlled by the transmembrane potential $v$. Let the magnitude of the active stress be $f(v)$, we have $\sigma_{act} = f(v)\kappa$. Quite a few models have been proposed to simulate the voltage-dependent active fiber tension $f(v)$ [13]. In this work, we adopt the simplified equation proposed by [13]:

$$\begin{cases} \dot{f} = \varepsilon(v)[k_f(v - v_r) - f] \\ \varepsilon(v) = \varepsilon_0 + (\varepsilon_\infty - \varepsilon_0)\exp\left[-\exp\left(-l(v - \overline{v})\right)\right] \end{cases} \tag{2.14}$$

In Equations 2.14, the symbol $k_f = 0.005\ \text{MPa/mV}$ is the maximum active fiber tension, and $v_r$ is the resting potential which is about -94.7mV for cardiac cells in the BR ionic model. The switch function is denoted by $\varepsilon(v)$ and it determines how fast the active fiber tension will change with respect to the transmembrane potential $v$. Parameters' values are $\varepsilon_0 = 0.1/\text{mV}$, $\varepsilon_\infty = 1/\text{mV}$, $l = 1/\text{mV}$, $\overline{v} = 0\text{mV}$. When $v$ changes from -94.7mV to 20mV, the function is as Figure 2-2.

Note that, the calcium fluctuation is not studied in this work and the active fiber tension is controlled by the membrane potential directly for simplification, as shown in Equations 2.14.

In Equation 2.3, the interconnection between cells is regulated by the diffusion tensor D. It controls the transduction speed of the electrical wave of excitation in the cardiac tissue. Due to the anisotropic properties of the heart tissue, it is observed in experiments that the conduction is obviously faster in the myofiber directions than in other directions. To consider the additional speed along the fiber orientations, the diffusion tensor is split into two parts: $D = d_{iso}I + d_{ani}\kappa$. The symbol I denotes an identity matrix. The coefficient $d_{iso} = 0.001\text{cm}^2/\text{ms}$ controls the speed of the isotropic transduction to all directions and the coefficient $d_{ani} = 0.0001\text{cm}^2/\text{ms}$ denotes the additional speed along the fiber orientations. Since the structural tensor $\kappa$ is dependent on the spatial coordinate, the diffusion tensor at each material point will change with the reshaping of the heart.

In Equation 2.3, the total ionic transmembrane current $I_{ion}$ consists of a component $I_{sac}$. The stretch activated channels are the ion channels which open their pores in response to mechanical deformation of the cell membrane [112]. According to what mechanisms the current is induced, there are different kinds of formulations for the stretch activated channels. In this work, we employ the formulation proposed by [113]:

$$I_{sac} = \delta G_s(|a| - 1)(v - v_s) \tag{2.15}$$
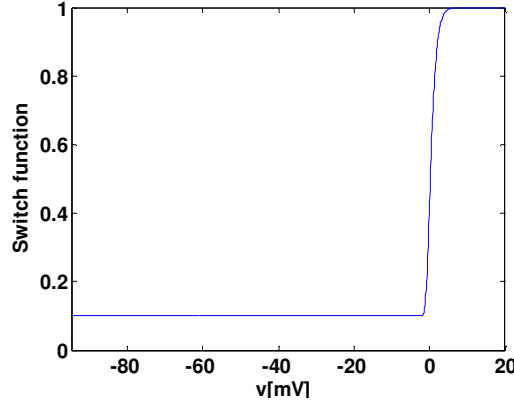
Figure 2-2: Illustration of the switch function with the following parameters:
$\varepsilon_0 = 0.1/\text{mV}, \varepsilon_\infty = 1/\text{mV}, l = 1/\text{mV}, \bar{v} = 0\text{mV}.$

In Equation 2.15, $G_s = 10\ \text{mS}/\mu\text{F}$ is the maximum conductance; $v_s = -20\text{mV}$ is the resting potential of the stretch-activated channels; $\delta$ is the coefficient that determines whether or not the stiffness of the myofibers is in effect, as defined in Equation 2.10; $|a|$ is the stretch at a material point of the heart.

## 2.3 Numerical computation approach

The governing equations 2.12 are solved using the operator splitting method [114]. First, we solve the following nonlinear ordinary differential equation using the forward Euler method [115]:

$$\frac{dv}{dt} + \frac{I_{ion}}{C_m} = 0 \tag{2.16}$$

Then, the solution from Equation 2.16 is used to solve the following partial differential equation 2.17 using the implicit Euler method. These two equations are solved iteratively for each time step.

$$\begin{cases} \frac{\partial v}{\partial t} - \nabla_x \cdot (D \cdot \nabla_x v) = 0 \\ \nabla_x \cdot \sigma + b = 0 \end{cases} \tag{2.17}$$

Weak forms of Equations 2.17 are constructed following the classical Galerkin procedure [116]. The weak form is obtained by taking the product of Equations 2.17 with the test functions $\delta x$ and $\delta v$ and integrating them over the domain. The time independent test functions are required to be C0, and satisfy the essential boundary conditions on $\partial\Omega$. Multiplying the test function $\delta x$ and $\delta v$ with the two equations in Equations 2.18 and carrying out integration by part yield:

18

$$
\begin{cases}
G_x = \int_\Omega \nabla_x(\delta x) : \sigma dV - \int_{\partial\Omega} \delta x \cdot \sigma \cdot n da - \int_\Omega \delta x \cdot b dV = 0 \\
G_v = \int_\Omega \left[ \delta v \frac{\partial v}{\partial t} + \nabla_x(\delta v) \cdot (D \cdot \nabla_x v) \right] dV - \int_{\partial\Omega} \delta v D \cdot \nabla_x v \cdot n da = 0
\end{cases}
\tag{2.18}
$$

Applying the natural boundary conditions to Equations 2.18 leads to Equation 2.19.

$$
\begin{cases}
G_x = \int_\Omega \nabla_x(\delta x) : \sigma dV - \int_\Omega \delta x \cdot b dV = 0 \\
G_v = \int_\Omega \left[ \delta v \frac{\partial v}{\partial t} + \nabla_x(\delta v) \cdot (D \cdot \nabla_x v) \right] dV = 0
\end{cases}
\tag{2.19}
$$

Linearizing Equations 2.19, we get:

$$
\begin{cases}
G_x(x_{n+1}, v_{n+1}) = G_x(x_n, v_n) + \Delta G_x(x_n, v_n; x_{n+1} - x_n, v_{n+1} - v_n) \\
G_v(x_{n+1}, v_{n+1}) = G_v(x_n, v_n) + \Delta G_v(x_n, v_n; x_{n+1} - x_n, v_{n+1} - v_n)
\end{cases}
\tag{2.20}
$$

We can then solve for $\Delta x = x_{n+1} - x_n$ and $\Delta v = v_{n+1} - v_n$ from the linearized equations.

The conventional isoparametric Galerkin procedure is followed to discretize the continuous weak form equations. The domain of the heart $\Omega$ is decomposed into subdomains $\Omega_e^h$, and each subdomain is an element. Then the field variables $x$ and $v$, and the two associated test functions are interpolated in each subdomain as

$$
\begin{cases}
x_e^h(X, t) = \sum_{j=1}^{n_{en}} N^j(X) x_j^e(t) \\
v_e^h(X, t) = \sum_{j=1}^{n_{en}} N^j(X) v_j^e(t)
\end{cases}
\tag{2.21}
$$

In Equation 2.21, $n_{en}$ is the number of nodes per element and $N^j(X)$ is the C0 interpolants, often called shape functions in finite element literatures. The implicit Euler method is utilized when discretizing time derivative terms in Equations 2.18. Finally, we achieved a linear system equation in form of:

$$
\{A\}_{4N*4N} \begin{pmatrix} \Delta x_n \\ \Delta y_n \\ \Delta z_n \\ \Delta v_n \end{pmatrix}_{n=1\sim N} = \{b\}_{4N}
\tag{2.22}
$$

The linear system equation has a degree of 4*N, where N is the number of the nodes in the mesh. For each node, $(\Delta x, \Delta y, \Delta z, \Delta v)$ are solved. They are then used to update the membrane potential and the spatial coordinate of each node.

The model was implemented in C++ and was parallelized using the message passing interface (MPI) [117]. An open source software package called

METIS [118] was used to partition the heart mesh so that computational loads are balanced among CPUs. The algorithms in METIS were based on multilevel recursive-bisection, multilevel k-way, and multi-constraint partitioning schemes.

Two parallel solvers were used to solve the final linear system. The two solvers are the hierarchical iterative parallel solver (HIPS) [116] and the solver from the Trilinos package [119]. Both of them implemented the generalized minimal residual method [120]. When using the Trilinos, the linear system was preconditioned by the Jacobi preconditioner. Simulations were run on the supercomputer, Kraken [121]. The open source software VisIt [122] was used for visualization.

## 2.4 Numerical results

### 2.4.1 A thin cardiac tissue

We first conducted simulations in a thin square cardiac tissue of the size 0.4*0.4*0.001cm3. In simulations, the top-left and the bottom-right corners were fixed and the fiber orientation was along vertical direction. We used the Forward Euler method to solve the ODE in Equation 2.16 at a time step of 0.005ms. The PDEs in Equation 2.17 are solved using the implicit Euler method with a time step of 0.1ms.

Action potential of a node at (-0.2cm, -0.2cm, 0.0005cm) as shown in Figure **2**-**3** was obtained using different mesh sizes. The numerical results show that consistent action potential responses are obtained using different mesh sizes. Because the cardiac tissue is very thin, it is treated like a 2d tissue. The mesh size is with respect to the x and y directions which are each 0.4cm in length.
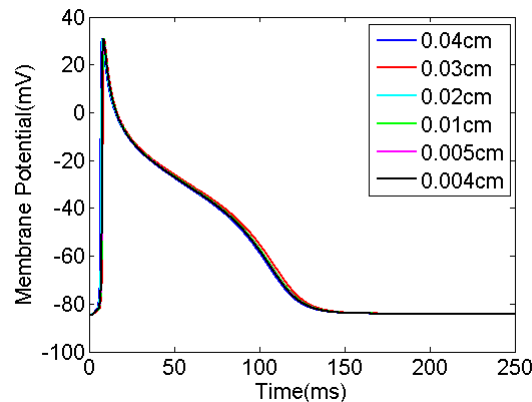


Figure 2-3: Action potential of a node at (-0.2cm, -0.2cm, 0.0005cm). Mesh size was decreased from 0.04cm (blue) to 0.004cm (black).

We then performed an electro-mechanical simulation in the tissue (0.4cm*0.4cm*0.001cm) with mesh size=0.004cm. The stimulation was imposed at the center of the tissue. Figure **2**-**4** shows the electrical wave propagation without considering the contraction. The electrical wave propagated symmetrically from the center to the whole tissue. This test validates the part of "reaction-diffusion" in our model by reproducing the basic phenomenon of electrical wave propagation in a square tissue. Note that, the coefficient $d_{ani}$ was set to 0 in this simulation so that the tissue was isotropic.

Figure **2**-**5** shows the electrical propagation as well as the excitation induced contraction in a tissue. In this test, the fibers of the tissue were aligned vertically. Thus the tissue deformed in vertical direction, as clearly shown at time t=7ms in Figure **2**-**5**. Moreover, in contrast to the previous test, we considered the additional speed along the fiber orientations, as indicated by $D = d_{iso}I + d_{ani}\kappa$. The coefficient $d_{ani}$ was set to $0.0001 \text{cm}^2/\text{ms}$. It's easily observed from Figure **2**-**5** that the propagation was obviously faster in vertical direction.

### 2.4.2 Dog ventricle with realistic geometry

We also simulated the contraction of a dog ventricle with realistic geometry. Two meshes were examined. The first mesh consisted of 880 Hexahedron elements. The second mesh which had 190080 hexahedron elements was refined from the first one using the software CUBIT which was developed at Sandia National Laboratories [123]. See Figure **2**-**6** for the original mesh and the refined one. The ventricle mesh was obtained from [124].
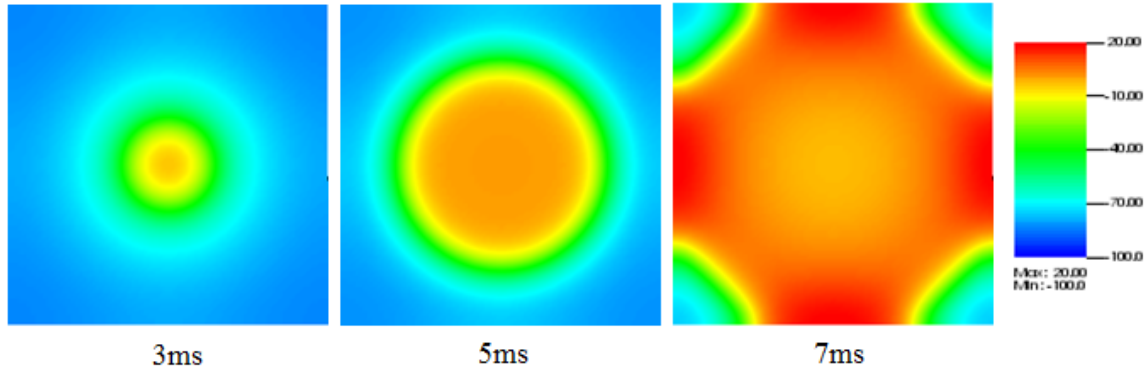


Figure 2-4: Electrical wave propagation in a piece of heart tissue

3ms       5ms       7ms
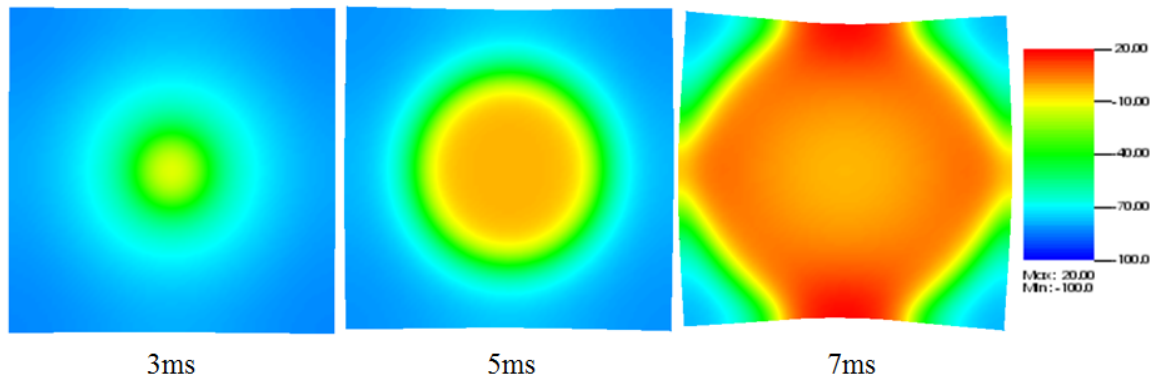
Figure 2-5: Electrical wave propagation and excitation-induced contraction in a piece of heart tissue. Although these tests are simple and straightforward, they demonstrate the model's capability of performing fully-coupled electro-mechanical simulations.
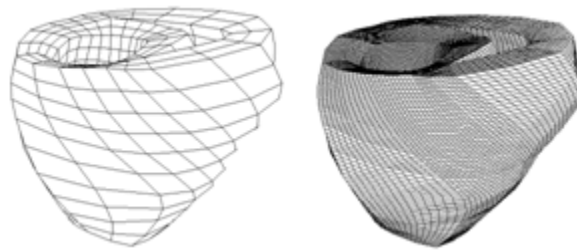


Figure 2-6: Dog ventricle mesh: original (left) and refined (right)

The constitutive and coupling models, the anisotropic electrical conductivity, and other parameters were the same as used earlier. The stimulus was imposed on the superior section of the ventricle as shown in Figure **2**-**7**. Some nodes on the upper surface were restrained so that the problem would be well defined. We assumed that the normal of the fiber at any point is pointing to the geometric center.

Under this assumption, the fibers form layers of muscle in the heart. We note that this assumption may not be close to realistic fiber layouts in the heart. However, the assumed structure allows us to test the efficiency and robustness of the computational algorithms on a heart, on which fiber orientation changes from point to point.

Figure **2**-**8** shows an electromechanical simulation of a dog ventricle with realistic geometry. Electrical stimulation was imposed on the upper surface of the septum. The contraction state kept for about 100ms and then slowly recovered to the resting state.
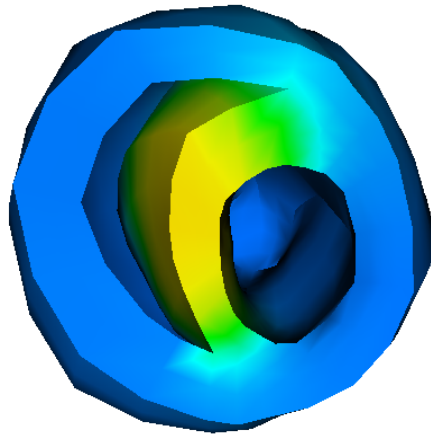
Figure 2-7: Initial stimulus: the stimulus was imposed on the superior section of the ventricle



5ms          10ms          15ms

20ms          25ms          150ms
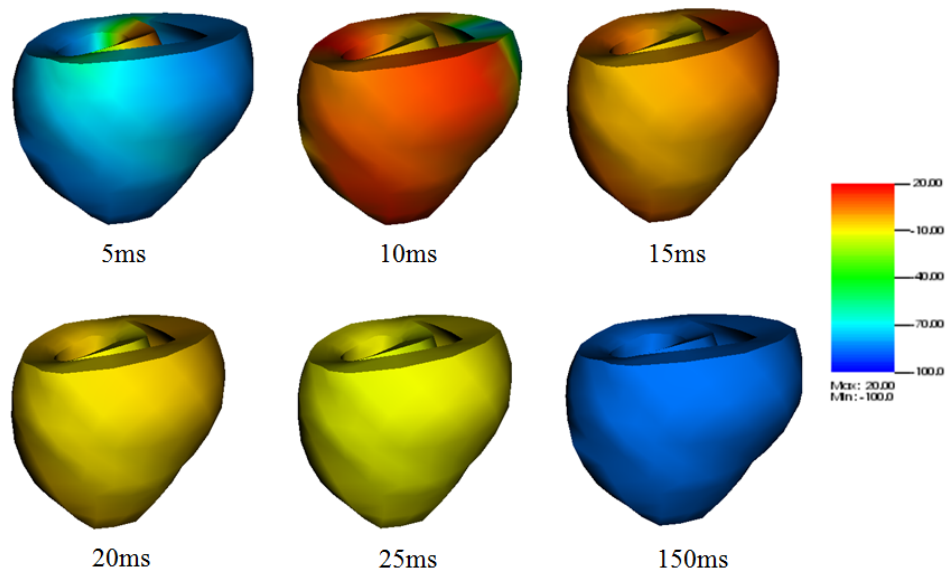
Figure 2-8: Electromechanical simulation of a dog ventricle with realistic geometry

We also simulated a ventricle with a scar near the outer surface. We have adopted a simplified description of scar. Specifically, we assumed the scar has no conduction capability and can maintain passive mechanical contractions like other cells. The scar had a size as shown in Figure **2**-**9**. The scar has a radius of about 1cm in the surface area and its thickness was similar to the ventricle wall.

Figure **2**-**9** shows the shapes of the contracting ventricle and the spatial distribution of membrane potentials at six moments. Comparing Figure **2**-**9** with Figure **2**-**8**, obvious difference can be observed. When the scar was present the membrane potentials was evidently smaller, and this could cause smaller active fiber tension and thus weakened pumping ability. Although no serious physiological conclusion could be given in this study since our simulations ware preliminary and lacked experimental validation, the simulations demonstrated the capability of our model to study the real heart.
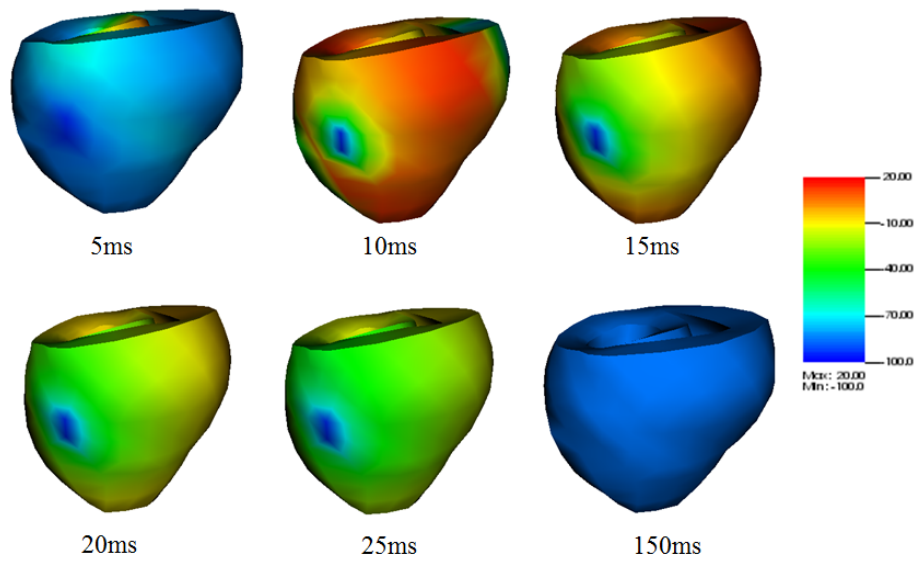
Figure 2-9: Electromechanical simulation of a dog ventricle with a scar near the outer surface.
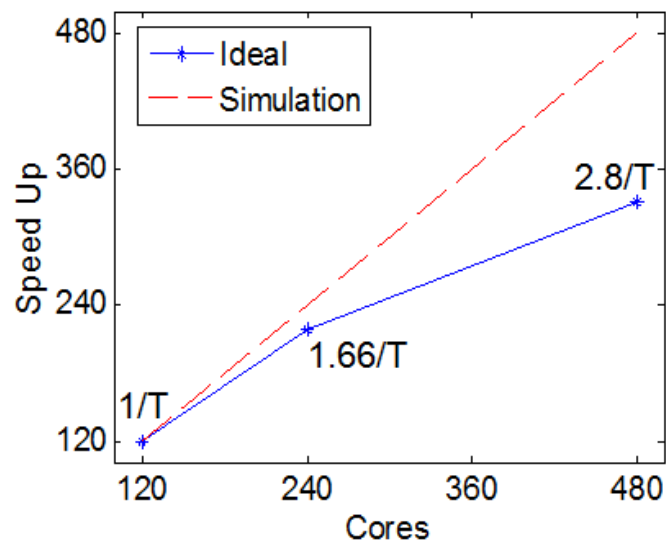


Figure 2-10: Scalability up to 480 CPUs on the Kraken system

### *2.4.3 Performance analysis*

Parallel efficiency is crucial for our model. The requirements of using meshes with hundreds of thousands of elements to achieve high accuracy and resolution make the computational efficiency a great challenge. The parallel efficiency is measured by the analysis of the scalability. A mesh with 1.56 million Hexahedron elements was used. In this analysis, we used 120, 240 and 480 cores. The time spent when using 120 CPUs was taken as the reference value. Figure **2**-**10** shows the strong scalability up to 480 cores on the Kraken supercomputer. In this case, the scalability for 240 cores was about 90% of the ideal and the scalability for 480 cores was about 70% of the ideal. The decrease of the scalability was due to the increase of the proportion of amount of communications per iteration and the increase of the proportion of the number of ghost nodes. The scaling ability was limited by the performance of the PDE solver from the Trilinos package [119]. In future studies, the performance will benefit from choosing a better parallel solving algorithm. Also the performance may be improved if we take use of the CUDA® [125] which is a parallel computing platform and programming model invented by NVIDIA®.

## 2.5 Summary

It is a common approach in the literature to solve the electromechanics problem in an iterative manner. In each step, the electrical problem is solved first and then the results from the electrical solution are submitted into the mechanical problem, whose solution is then used to solve the electrical problem in the next step. Since the electrical problem and the mechanical problem are solved separately, it is also a common practice to adopt a fine mesh for the electrical field and a much coarser mesh for the mechanical field.

The contribution of this work is to develop a fully coupled scheme to accurately solve the electromechanics of the heart. We have developed a cardiac electromechanics model, which integrates cardiac electrophysiology, mechanical contraction, as well as their interactions. Realistic physiological models have been adopted to describe the electrical and mechanical functions in the heart. The model has been numerically solved using an implicit, finite element-based approach. Numerical simulations have been conducted using parallel simulation in tissues of different geometries. The cardiac mechanics is described by the updated Lagrangian approach, which views the problem from the current configuration and takes derivatives and integrals with respect to the spatial coordinates. In perspective of mesh description, the updated Lagrangian description is characterized by making the material points remain coincident with mesh points. Therefore, the Lagrangian description simplifies the imposition of

boundary conditions since the element boundaries of the mesh remain coincident with material boundaries. The developed model and computer codes have been validated at each step using simple test examples to ensure accuracy in numerical computations. Multiple simulations have been conducted using various meshes and parameters to ensure numerical robustness of the developed model.

# CHAPTER 3
## INFLUENCE OF ION CHANNEL BLOCKADE ON CARDIAC ALTERNANS

## 3.1 Overview

Investigating the mechanisms that can suppress abnormal heart rhythms is of great importance in preventing fatal cardiac arrhythmias, such as ventricular fibrillation, atrial fibrillation and so on. In this chapter, the effects of channel blockers will be studied through mathematical modeling of cardiac electrophysiological phenomena. The model developed in Chapter 2 is taken into sue. Several different electrophysiological models will be utilized to understand how sodium blockers affect the initiation of alternans in single cells, fibers, and tissues.

The majority of anti-arrhythmic drugs were designed to target specific ion channels corresponding to a certain abnormality in the heart [29]. One example is the sodium channel blockers, which can be used for preventing atrial fibrillation (AF) by extending the refractory period in atria [30]. However, significant promotion of the inclination for VF was observed in two clinical trials in patients who were treated with class IC drugs [33]-[34]. Class IC drugs are compounds that inhibit Na+ channels without any significant impact on the action potential morphology and duration. Since the sodium channel blockers were shown to be effective in preventing AF, it is valuable to investigate the influence of the drugs on healthy ventricular tissues so that we can judge the safety of the treatment for a patient who is predisposed to AF, but possesses normal ventricles.

Based on the above consideration, we will incorporate the pure sodium channel blockers into three ventricular action potential models. The three models are the Beeler-Reuter model [109], the FMG model [126] and the Shiferaw-Fox model [127]. The first is a generic model which has been introduced in Chapter II, while the latter two are both canine models. As the drugs are supposed to treat human beings, it is obviously best to use human ventricular models for simulation. Unfortunately, however, human heart studies suffer from a lot of limitations, including the difficulty of obtaining healthy heart data [128]. Consequently, in order to achieve more valid conclusions, we simulated three non-human models and compared their simulation results.

Some interesting findings will be presented in this chapter, which include: 1) a significant difference between simulations at multiple scales, indicating the necessity of a multi-scale study upon cardiac issues; 2) that the drugs change the critical pacing period corresponding to the onset of alternans as well as the alternans' amplitude. However, the drugs' effects are not consistent in the three models, which indicate the importance of developing a human cardiac model. On

the whole, the drugs promote the inclination for arrhythmias; 3) that the changes in the onset of alternans are dependent on the length of a fiber or the size of a tissue, and particularly, that the influence of a fiber's length on the onset of alternans is promoted by the sodium channel blockers; 4) a coexistence of multiple solutions in the tissues of the Shiferaw model.

## 3.2 Method

### 3.2.1 Electrophysiological Models

The model developed in Chapter II is used in this study. Since we are only concerned about the electrophysiology, the excitation induced contraction and the mechano-electric feedback are ignored. But it will be an interesting study to consider the mechanical contraction and the feedback in the future. For completeness, the electrophysiological model will be shortly reviewed first.

As introduced in Section 2.2.1, the cardiac electrophysiology is modeled using the reaction-diffusion equation:

$$\frac{\partial v}{\partial t} + \frac{I_{ion}}{C_m} - \nabla_x \cdot (D \cdot \nabla_x v) = 0 \qquad (3.1)$$

In Equation 3.1, x represents the spatial coordinate of each material point in the heart; $D$ is the diffusion tensor, which controls the transduction orientation and speed of the electrical wave of excitation in the cardiac tissue; $C_m$ is the membrane capacitance and is set as $1\mu F/cm$.

The Beeler-Reuter model [109] is a generic ventricular model of mammals including 8 variables. It is made up of four individual components of ionic current in terms of Hodgkin-Huxley type equations [11], comprising the sodium, potassium and calcium currents, among which the sodium current primarily determines the rapid upstroke of the action potential, while the configuration of the plateau and the re-polarization phase is determined by the other currents. This model explains the calcium dynamics in a simplified way without involving intricate calcium dynamics. It showed the spiral waves for the first time, and it also showed the breakup of the spiral waves which represents the induction of ventricular fibrillation [12]. The Fox-McHarg-Gilmour model is based on the Winslow-Rice-Jafri-Marban-O'Rourke model (1999) [129], which is the first canine model. The Fox-McHarg-Gilmour model is used with modification to ensure that alternans occurs at a high paced rate. The Shiferaw model improves the FMG model by describing the intracellular calcium dynamics in a more detailed way. It reproduces the experimentally observed "graded release" and makes the total release of calcium from the sarcoplasmic reticulum (SR) equal the sum of local releases.

### 3.2.2 Tissue simulation

For a single cell, the partial differential equation 3.1 reduces to an ordinary differential equation by dropping the diffusion term. A strand of cells is simulated by applying sealed boundary conditions (dv/dx=0) to the first and the last cells of the fiber. We simulated fibers with 25 cells, 50 cells, 75 cells, 100 cells and 125 cells. The length of each grid is set as dx=0.015 cm. Similarly, we simulated tissues with size of 25cell×25cell, 50cell×50cell, 75cell×75cell, 100cell×100cell and 125cell×125cell.

### 3.2.3 Incorporation of pure sodium channel blockers

Usually, the sodium current takes the form of Equation 3.2, where v is the membrane potential; m, h and j are voltage-dependent gate parameters; $\overline{G_{Na}}$ is the fully activated sodium conductance and $G_{N_aC}$ is the background sodium conductance; $E_{Na}$ is the $Na^{2+}$ equilibrium potential; $\alpha_m$, $\beta_m$, $\alpha_h$, $\beta_h$, $\alpha_j$ and $\beta_j$ are parameters that are dependent on the voltage.

$$I_{Na} = (\overline{G_{Na}}m^3hj + G_{N_aC})(v - E_{Na})$$
$$\frac{dm}{dt} = \alpha_m(1-m) - \beta_m m$$
$$\frac{dh}{dt} = \alpha_h(1-h) - \beta_h h \tag{3.2}$$
$$\frac{dj}{dt} = \alpha_j(1-j) - \beta_j j$$

A gate variable typically has two states: open and closed. It varies between 0 (closed) and 1 (open). It can be modeled in terms of first-order transition between closed and open states [11]:

$$Closed \underset{\beta}{\overset{\alpha}{\longleftrightarrow}} Open$$
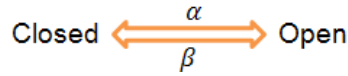
The dynamics can be described by Equation 3.3, in which $\alpha_a(v)$ and $\beta_a(v)$ are voltage sensitive transition rates, and a is the possibility of the channel being open.

$$\frac{da}{dt} = \alpha_a(v)(1-a) - \beta_a(v)a \tag{3.3}$$

Sodium blockers will block the sodium channels by reducing the conductance. In addition to the original open and closed states, channels bounded to blockers will have a "blocked" state. Following the model by Starmer et al. 2002 [35], we describe the states of channel blockade as

$$Closed \underset{\beta}{\overset{\alpha}{\longleftrightarrow}} Open \underset{l}{\overset{k[Drug]}{\longleftrightarrow}} Blocked$$
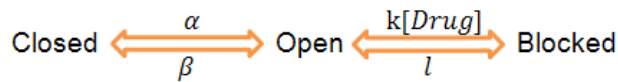
Let us denote the probability of the channels being blocked by b. The kinetics of b can be written as [35] Equation 3.4, in which *Drug* represent the drug concentration, k and l represent the rates of block and unblock.

$$\frac{db}{dt} = k[\text{Drug}](1 - b) - lb \qquad (3.4)$$

As a result of blockade, the current of sodium channel is changed to Equation 3.5.

$$I_{Na} = (\overline{G_{Na}}m^3hj + G_{N_aC})(1 - b)(v - E_{Na}) \qquad (3.5)$$

### 3.2.4 Pacing Protocols

In the simulation of fibers, the first five cells are stimulated by current of -80μA/μF for 1ms. In the simulation of tissues, an area of 5cell×5cell in the left bottom corner is paced. The basic cycle length (BCL) is crucial for cardiac dynamics, playing a critical role in determining whether the electrical alternans will occur; for example, in the FMG model, alternans occurs at a high paced rate, corresponding to a short BCL. For each action potential model, fibers and tissues are simulated from a long BCL to a short one. For example, we simulated the B-R model incorporated with blockers from BCL=950ms to BCL=750ms, decreasing in the interval of 25ms, while the same action potential model without blockers is simulated from BCL=450ms to BCL=250ms. At each BCL, we repeated the pacing until the cardiac dynamics reached the steady state.

## 3.3 Results

### 3.3.1 Parameters and figures of interest

The action potential duration (APD) restitution relation, defined as the relationship between APD and the previous diastolic interval (DI), is an important determinant of cardiac dynamics [132]. If the slope of the restitution relation is ⩾ 1, an alternation of APD, known as electrical alternans, may occur [133]. It commonly develops during high-frequency pacing. Consequently, when we pace tissues from a long BCL to a short one, no sustained alternans will occur at first, but will emerge after a critical BCL. We define such a BCL as "alternans onset BCL." Now that the occurrence of the alternans implies a substrate that is more likely to induce arrhythmias, we may expect a small "alternans onset BCL," since that would make the alternans less likely to be induced in situations like ventricular tachycardia (VT).

At the fiber level, the APD in each cell is calculated at every beat. If we simulate a fiber with 175 cells at BCL=775ms for 200 beats and the difference between APDs in the last 10 beats can be neglected in all the cells, we say the fiber at that BCL is in the state of "no alternans." If alternans appears, and the APDs alternate in a consistent manner in all of the 175 cells, we say the fiber at

that BCL has "concordant alternans." In contrast, if APDs alternate in a long-short pattern in some cells but in a short-long pattern in other cells, the pattern is defined as "discordant alternans." Moreover, if the number of APDs in any of the 175 cells is less than the corresponding beat number, we say that the "conduction block" occurs.

### 3.3.2 Results from simulating B-R Model

Figure **3**-**1** shows the results of simulations at the cellular and fiber levels by the B-R model. In a single cell, the alternans start to appear at the BCL=350ms when the drug is applied, while no alternans occur when it is not blocked. The sodium channel blocker obviously increases the "alternans onset BCL".

In fibers, when the blocker is absent, concordant alternans first happens at BCL=330ms, but when the model is incorporated with drugs, concordant alternans starts to happen at BCL=735ms. This difference indicates the adverse effect of the drugs. A "J" shaped curve is observed, which shows that the length of the fiber also plays an important role in determining the onset of the alternans, as the BCL does.

Figure **3**-**2** shows the results of simulations at the tissue level. The onset of alternans comes much earlier when the sodium channel is blocked (right of Figure **3**-**2**).
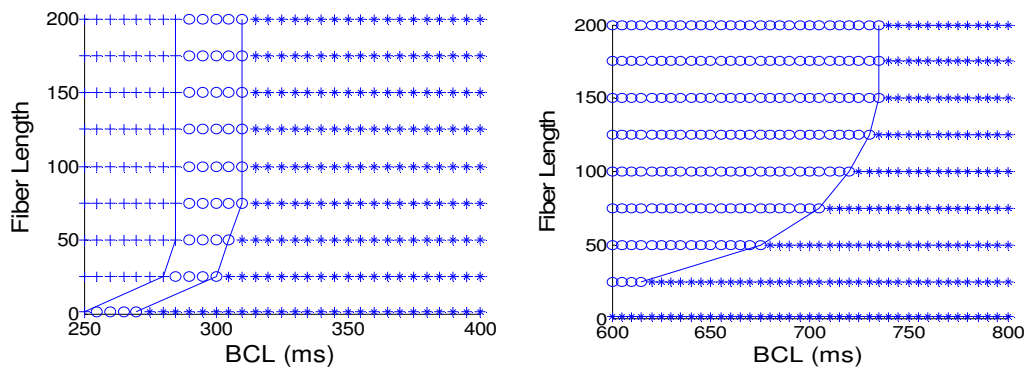
Figure 3-1: Results from simulations in single cells (when y-coordinate is 1) and fibers by B-R model. Left: the blockers are absent; right: the drugs are incorporated into the model. The x-coordinate represents the BCL, and the y-coordinate represents the cell number of each fiber. The "*", "o", square, and "+" respectively stands for "no alternans", "concordant alternans", "discordant alternans", and "conduction block".
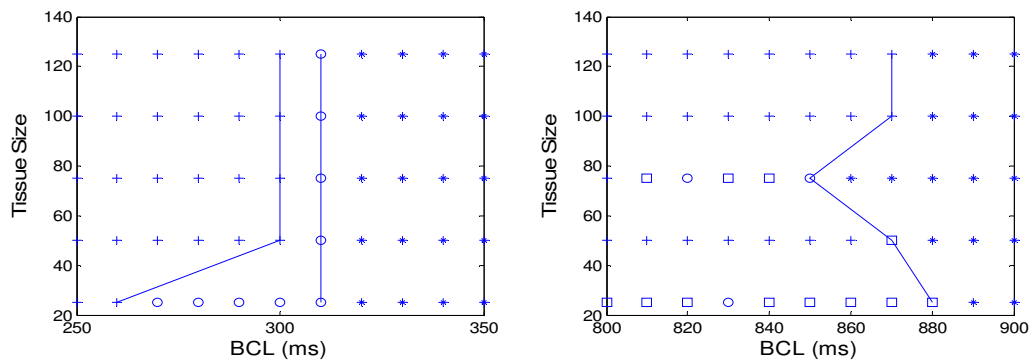


Figure 3-2: Results from simulations in tissues by the B-R model. Left: the blockers are absent; right: the drugs are incorporated into the model. The x-coordinate represents the BCL, and the y-coordinate represents the number of cells at one side of the tissue. The "*", "o", square, and "+" respectively stands for "no alternans", "concordant alternans", "discordant alternans", and "conduction block". The onset of alternans comes much earlier when the sodium channel is blocked

34

### 3.3.3 Results from simulating FMG Model

At the cellular level, the sodium channel blockers increase the alternans' amplitude, but in fibers the alternans' amplitude was suppressed by the drugs; as shown in Figure 3-3. Figure **3**-**4** shows the results from simulating the FMG model. The right of Figure **3**-**4** shows the fibers' responses to BCLs at 200ms to 400ms, because almost no alternans was observed below BCL of 200ms. Figure **3**-**4** also shows the supression of alternans by the drugs.

At the tissue level (Figure **3**-**5**), the alternans onset BCL tends to increase with the tissue's size, but the tendency is weak. The drug doesn't have influence in this case.

### 3.3.4 Results from simulating Shiferaw Model

Figure **3**-**6** shows the results of the simulations at the cellular and fiber levels using the Shiferaw model. At the cellular level, the drug has no significant influence. At the fiber level, when the drug is absent, the "alternans onset BCL" does not change with the fiber length, fixed at about 410ms. But when the drug is incorporated into the model, a significant "J" curve is seen. We supposed that the drug enhances the contribution of the fiber length to the initiation of the electrical alternans.

Figure **3**-**7** shows the results from simulations on tissues when drug is not present. At BCL around 410ms, alternans appears in each tissue. Unlike the simulations in fibers, the drug shows little impact.
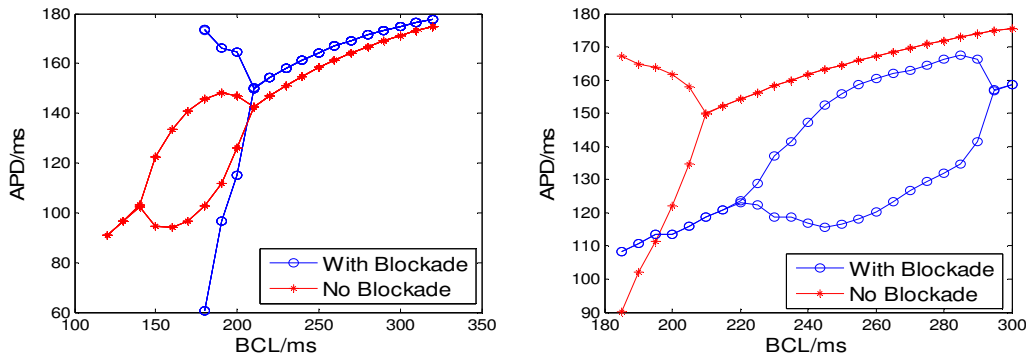


Figure 3-3: Influence of sodium channel blockers in FMG model is different at the cellular level from that at fiber level. Left: in a single cell, the alternans amplitude was enlarged by the drug; right: in a fiber with 25 cells, the alternans amplitude was diminished after the blocker was incorporated.
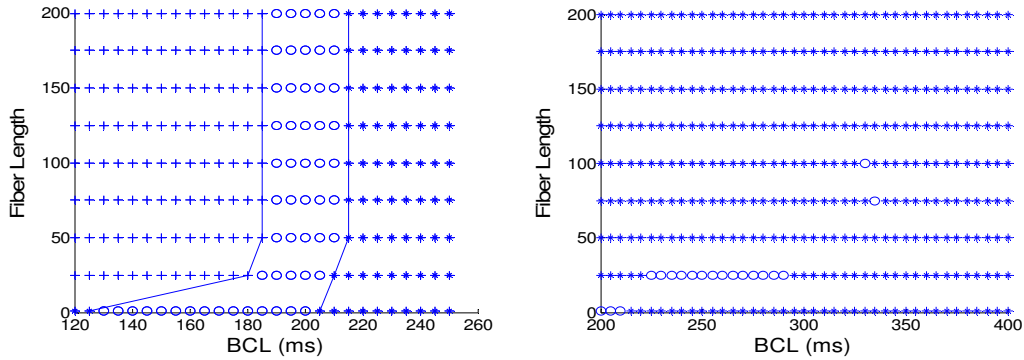
Figure 3-4: Results from simulating single cell (when y-coordinate is 1) and fibers of FMG model when drug is absent (left) and present (right). The x-coordinate represents the BCL, and the y-coordinate represents the cell number of each fiber. The "*", "o" and "+" respectively stands for "no alternans", "concordant alternans", and "conduction block".
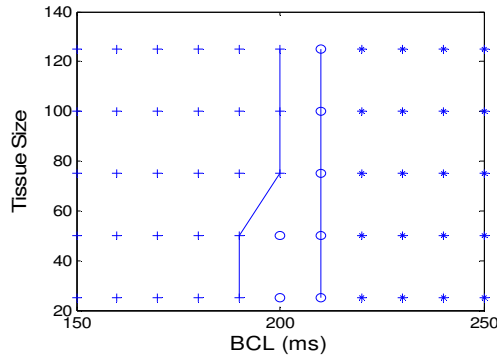


Figure 3-5: Results from simulating tissues of FMG model when drug is absent. The x-coordinate represents the BCL, and the y-coordinate represents the number of cells at one side of the tissue. The "*", "o" and "+" respectively stands for "no alternans", "concordant alternans", and "conduction block"
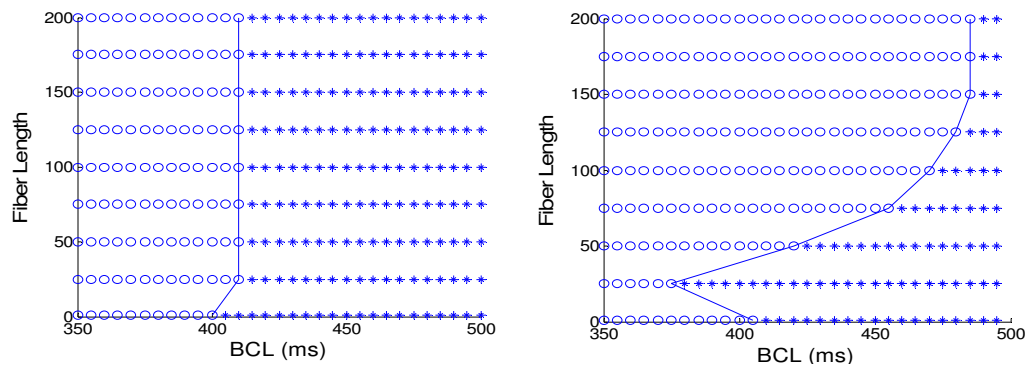
Figure 3-6: Results from simulations in fibers by the Shiferaw model. Left: the blockers are absent; right: the drugs are incorporated into the model. The x-coordinate represents the BCL, and the y-coordinate represents the number of cells of each fiber. The "*", "o" and "+" respectively stands for "no alternans", "concordant alternans", and "conduction block".
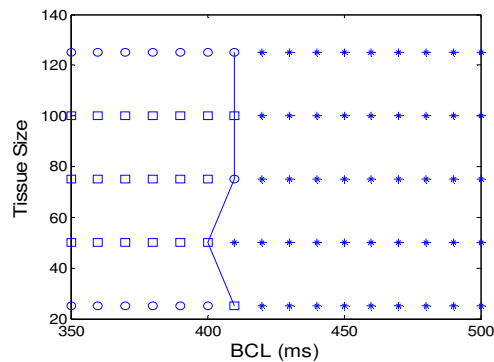


Figure 3-7: Results from simulations in tissues by the Shiferaw model when blockers are absent. The x-coordinate represents the BCL, and the y-coordinate represents the number of cells at one side of the tissue. The "*", "o" and "+" respectively stands for "no alternans", "concordant alternans", and "conduction block".

### 3.3.5 Multiple solutions in tissues of the Shiferaw model

We considered a homogeneous tissue of 10*10 cells of Shiferaw model with negative Cain→Vm coupling. Similar to what was found in [36], numerical simulations show that when the tissue is in alternans, there coexist multiple solutions for a given pacing period.

First, we paced the tissue with the downsweep protocol [38][134] from BCL=500ms to BCL=375ms. We found that the solution of the downsweep protocol in a tissue was not influenced by the initial conditions.

Two types of initial conditions are used in this work: 1) all cells of the tissue are uniformly assigned the same resting voltage, gating variables, and ionic concentrations; 2) the [Cain] and [Cas] are randomly assigned for cells in the tissue according to a uniform distribution in the interval of 0.45–0.75μM, and the [Caj] and [Cajp] are randomly assigned for cells in the tissue according to a uniform distribution in the interval of 79.5–132.5 μM.

Figure **3**-**8** and Figure **3**-**9** show the distribution of APD and [Cain] along a fiber in the tissue. The tissue is paced in a downsweep protocol in Figure **3**-**8** and the downsweep steps are 25ms in Figure **3**-**8**a and 5ms in Figure **3**-**8**b. The distribution of APD and [Cain] along the same fiber is shown in Figure **3**-**9**. The tissue is paced at BCL=375ms for Figure **3**-**9**, and initial conditions are uniformly assigned in Figure **3**-**9**c but randomly assigned in Figure **3**-**9**d.

Similar results are observed when we look into the distribution of APD and [Cain] along other fibers in the tissue. These results demonstrate that the alternans in a tissue is not uniquely determined by the pacing period, but the solution is also sensitive to the pacing protocol and the initial conditions.
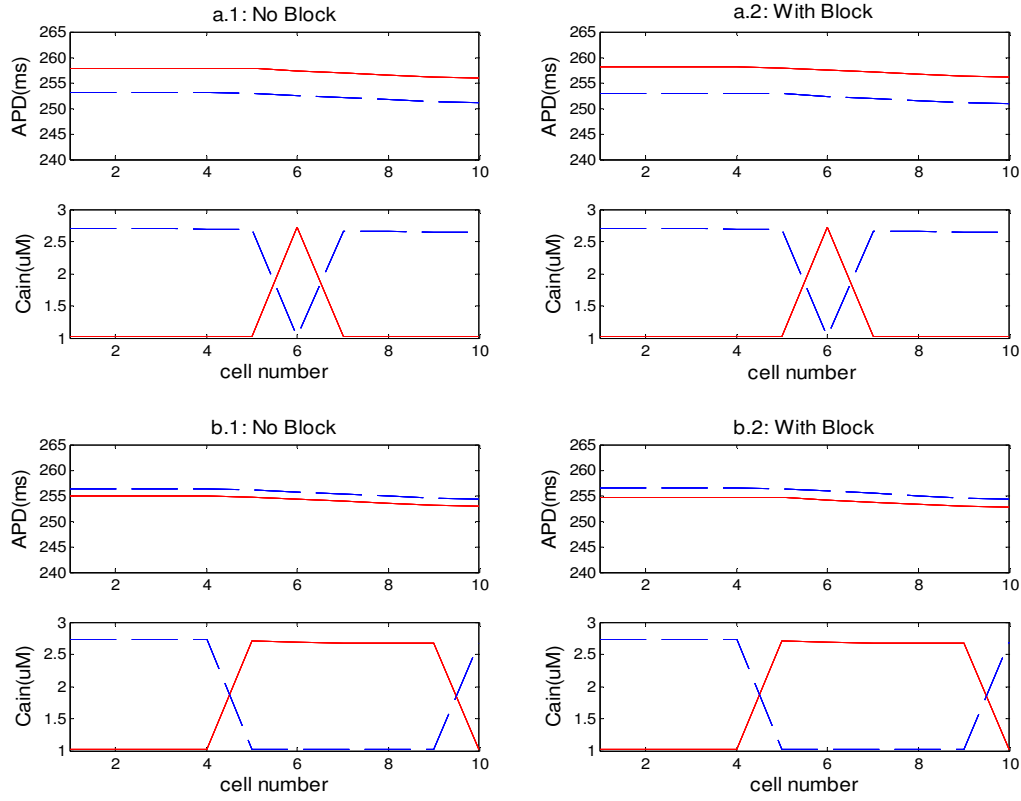
Figure 3-8. (a): the APD and [Cain] distribution along an arbitrary fiber in the tissue at BCL=375ms, and the tissue is paced from BCL=500ms to BCL=375ms in downsweep protocol, with ΔB=25ms. (b): the APD and [Cain] distribution at BCL=375ms along the same fiber as in (a) in the tissue, and the tissue is paced from BCL=500ms to BCL=375ms in downsweep protocol, with ΔB=5ms.
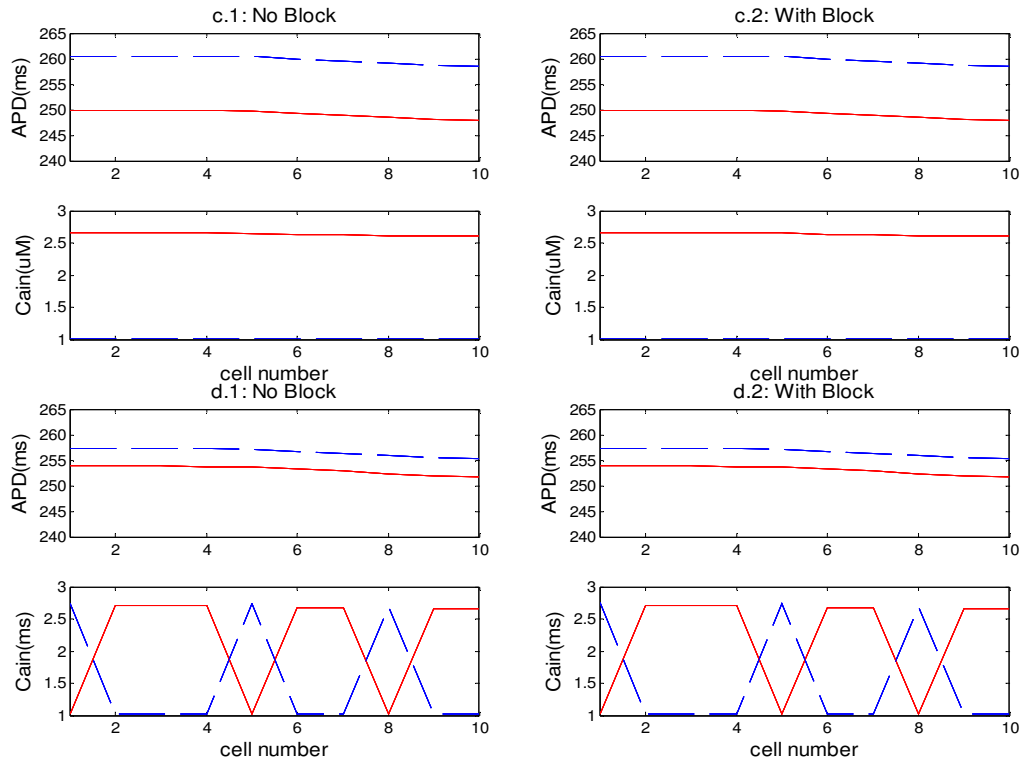
Figure 3-9. (c): the APD and [Cain] distribution at BCL=375ms along the same fiber as in Figure 3.8, and the initial condition is uniformly assigned; (d): the APD and [Cain] distribution at BCL=375ms along the same fiber as in Figure 3.8, and the initial condition is randomly assigned

## 3.4 Summary

In this chapter, a study has been presented for the investigation of the effects of sodium channel blockers through mathematical modeling of cardiac electrophysiological phenomena. Multi-scale simulation has been accomplished, and we have observed significant differences between different scales, indicating the necessity of a multi-scale study upon cardiac issues. We have found that the drugs changed the critical pacing period corresponding to the onset of alternans as well as the alternans' amplitude, but the effect of the drugs was not consistent in the three models. On the whole, the drug has shown an adverse effect upon the electrical alternans. In addition, the changes in the onset of alternans were found to be dependent on the length of a fiber or the size of a tissue. Moreover, coexistence of multiple solutions in the tissues of the Shiferaw model was observed.

Starmer et al. contributed a lot to the understanding of the pro-arrhythmic properties of the sodium channel blocker. They studied the influence of the sodium channel antagonists on the vulnerable period (VP), and found that the antagonists increase the duration of the VP by both slowing conduction velocity and reducing the gradient of excitability [32]. This work addresses the same problem but from a different perspective: the blocker's effect on the initiation of alternans.

The relation of the electrical alternans to the sodium channel current was also shown by Fox et al. 2002 [126] earlier as they found the increase of the alternans' amplitude could be obtained by reducing $I_{Na}$, but we have extended that to the fiber and tissue levels and have found interesting phenomena.

In addition, Blas Echebarria and Alain Karma achieved an equation that governed the spatiotemporal dynamics of small amplitude alternans in paced cardiac tissue [135]-[136]. Alternans' amplitude, pacing period, and fiber length are related in that equation and the relationship between them was predicted by incorporating the equation with a two variable model. The results they obtained are similar to what we achieved. And in this work, we have found that the sodium channel blockers modified that relationship, as we see that the role of the fiber length in determining the onset of alternans was promoted by the sodium channel blockers.

41

# CHAPTER 4
## INFLUENCE OF ELECTRO-MECHANICAL COUPLING ON CARDIAC ALTERNANS

## 4.1 Overview

Two mechanisms for the discordant alternans were demonstrated by one and two dimensional simulations of action potential propagation models in spatially homogeneous tissues. The first and the more important mechanism was the interaction of conduction velocity and action potential duration restitution at high pacing rates. The second was the dispersion of diastolic interval produced by ectopic foci.

Though the theory is very well proved by simulation of cardiac electrophysiology, no effects of the electro-mechanical coupling have been considered so far. In this chapter, we carefully examined the effects of the electro-mechanical coupling on the formation of the APD alternans.

As will be shown in the chapter, this study supported that the discordant alternans is induced by the interaction of conduction velocity and action potential duration restitution at high pacing rates, no matter whether contraction is considered or not. However, when contraction is considered, the formation of the discordant alternans is in a very different way, and it's dependent on the boundary conditions.

## 4.2 Method

The electro-mechanical model developed in Chapter 2 is taken into use in this chapter. For completeness, the model is shortly reviewed. The Beeler-Reuter (BR) ion channel model [109] was applied to the cardiac tissue. The transmembrane current $I_t$ can be written as Equation 4.1, in which $C_m$ is the membrane capacity, v is the transmembrane voltage, $I_{ion}$ represents the current through ion channels, $I_s$ represents the current through stretch activated channels, and $I_{ext}$ represents external stimulation.

$$I_t = C_m \frac{\partial v}{\partial t} + I_{ion} + I_s + I_{ext} \tag{4.1}$$

Consider a cardiac fiber stimulated at the left end. Let X represent the original, undeformed configuration and let x represent the deformed position. Consider a small element on the fiber as shown in Figure **4**-**1**. Here, "I" represents the current along the fiber and $I_t$ represents the transmembrane current. It follows the Kirchhoff's circuit law (Equation 4.2).

Following the approach in Keener and Sneyd (1998), one can obtain the Equation 4.3. Substituting Equations 4.2 and 4.3 to 4.1 leads to Equation 4.4.

$$I_t dx = I(x + dx) - I(x) \tag{4.2}$$

$$I(x) = K \frac{\partial v}{\partial x} \tag{4.3}$$

$$C_m \frac{\partial v}{\partial t} + I_{ion} + I_s + I_{ext} = K \frac{\partial^2 v}{\partial x^2} \tag{4.4}$$

The same ionic equations are applied to all cardiac tissues of one dimension and two dimensions. The forward Euler method was utilized to solve the partial differential equations in the model, with step-sizes of 0.25 mm and 0.02 msec. The APD restitution refers to the dependence of APD on preceding diastolic interval (DI), and the conduction velocity restitution refers to the dependence of conduction velocity on preceding DI. The APD and DI were measured as the time interval above and below the membrane potential of -60mv respectively at a specific location.

Although the cardiac mechanics was introduced thoroughly in Chapter 2, I'd like to give a short review overly it for completeness. It is a common approach to neglect inertial force and viscous damping when describing mechanical deformation. Then, the balance of linear momentum leads to the following equilibrium equation:

$$\frac{\partial \sigma}{\partial X} = 0 \tag{4.5}$$

$$\sigma_{pass} = Y(\frac{\partial x}{\partial X} - 1) \tag{4.6}$$

$$\frac{d\sigma_{act}}{dt} = \varepsilon(v)[k_\sigma(v - v_r) - \sigma_{act}] \tag{4.7}$$

$$\varepsilon(v) = \begin{cases} 0.1, \text{if } v < \bar{v} \\ 1.0, \text{if } v > \bar{v} \end{cases} \tag{4.8}$$

In Equation 4.5, $\sigma$ represents the total stress along the fiber. Note that $\sigma$ consists of two components: the passive mechanical stress $\sigma_{pass}$ and active fiber tension $\sigma_{act}$ due to contraction of cardiac cells. Assuming linear elastic materials, the mechanical stress is related to deformation of the fiber as shown in Equation 4.6.
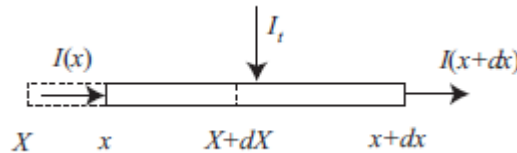


Figure 4-1. Fiber element

In Equation 4.6, Y represents the Young's modulus. Various models have been developed for active stresses. Here, we adopt a simple differential equation model proposed by Nash and Panfilov (2004) [13] as shown in Equation 4.7, where $v_r$ represents the resting action potential and $k_\sigma$ controls the saturated value of cell contraction stress. Nash and Panfilov (2004) [13] adopted a Heaviside form for $\varepsilon(v)$ as shown in Equation 4.8.

Combing equations (4.4, 4.5, 4.6, 4.7), we obtain the coupled electro-mechanical model of the cardiac tissue. For numerical simulations, we can adopt the following parameters in Table 4-1. Note that parameters are adopted from [13] [137], where the 2-variable Aliev-Panfilov (1996) [138] electrical model is adopted.

Two types of boundary conditions are imposed to ensure that the mechanical problem is well defined. We assume the left end is always fixed. It follows that $x(0) = 0$. For the right end, we consider two different scenarios: fixed or free.

# 4.3 Results and Discussion

### 4.3.1 Relationship between number of APD nodes, BCL, and cable length at steady state

It was shown in [42] that interaction of conduction velocity and action potential duration restitution at high pacing rates could induce spontaneously formed discordant alternans in spatially homogeneous tissues. Define the boundaries that mark the regions of alternans with opposite phase as APD nodes. They showed that longer cable lengths and higher pacing rates would allow more nodes in general. In this work, we observed similar phenomenon, as shown in Figure **4**-**2**. To study the effects of the mechanical contractions, two different scenarios were considered: contracting fiber with either fixed right end or free right end, as shown in Figure **4**-**3**.

**Table 4-1: Parameters used in numerical simulations**

| Parameter | Value |
|-----------|-------|
| $\bar{v}$ | 0.05 [20] (we take $\bar{v}$ = –30 mV in simulations using BR model) |
| $k\sigma$ | 5 Kpa mV–1 [20] |
| vr | resting potential |
| Y | 1 Mpa |
| Gs | vary from 0.1 to 0.5 [21] |
| Es | 1 [21] |

Comparing Figure **4**-**2** and Figure **4**-**3**, the APD alternans appears at bigger BCL when the contraction is considered. When both ends are fixed, the discordant alternans first appears at BCL=335ms at the fiber of 12cm. When the right end is free, discordant alternans is not observed until BCL decreases to 305ms. Lower pacing rate of the onset of APD discordant alternans implies more stable cardiac dynamics. Thus when both ends are fixed, the mechanical contraction may destabilize the electrical stability of the cardiac dynamics, while when one end is free, the cardiac dynamics will more likely to be stabilized by the contraction.

The dependence of the number of APD nodes on BCL and fiber length is also affected by the mechanical contraction. When mechanical contraction is not considered, number of APD nodes always increases as fiber length increases or BCL decreases (Figure **4**-**2**). Similar phenomenon is observed for right of Figure **4**-**3** too. However, when both ends are fixed, number of APD nodes may decrease as BCL decreases for a given fiber length, for example when fiber length is 6, 7, 8, 9, 10, 11, 12, 13, or 14cm in left of Figure **4**-**3**.
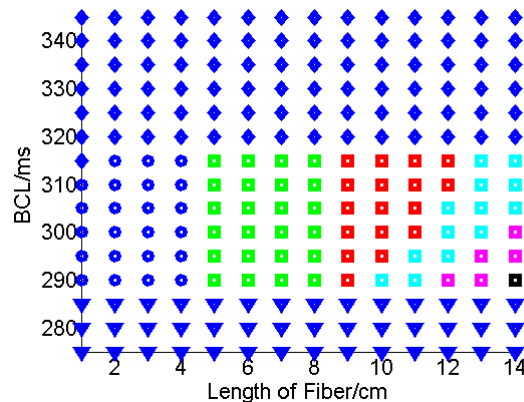


Figure 4-2. Without considering contraction, as cycle length is shortened for a given cable length, the number of nodes increases, and as cable length increases for a certain cycle length, the number of nodes also increases. Parameter space is divided into conduction block (triangle), no alternans (diamond), concordant (circle), 1 node (square-mark and green), 2 nodes (square-mark and red), 3 nodes (square-mark and cyan), 4 nodes (square-mark and magenta) and 5 nodes (square-mark and black) regimes.
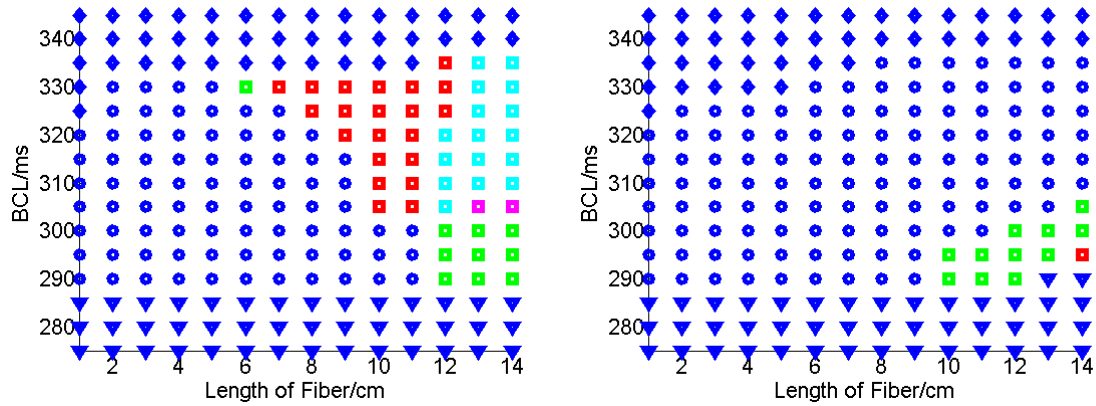
Figure 4-3. Notations are similar to Figure 4-2. Left: when considering contraction and both ends of the fiber are fixed, number of APD nodes may decrease as BCL decreases for a given fiber length (for example, at 6, 7, 8, 9, 10, 11, 12, 13, or 14cm). Right: when contraction is considered and the right end is free, similar to Figure 4-2, the number of nodes increases when BCL decreases or cable length increases. But the onset BCL of APD discordant alternans is 305ms, much smaller than what's observed in Figure 4-2.

### 4.3.2 Evolution of spatial distributions with continued stimulation

After APD nodes arise far away from stimulus site, they will typically move toward the stimulus site as simulations continue (Watanabe et al 2001). Similar phenomenon was observed when contraction was not considered in this work, as shown in Figure **4**-**4**. In Figure **4**-**4**, the cable was paced at the left edge at a rate of 315ms, and the fiber length was 10cm. The spatial distribution for even (red) and odd (blue) beats were shown for stimulus numbers 2, 3 (first), 15, 16 (second), 50, 51 (third), and 300, 301 (fourth). One new APD node was formed at the right end after about 20 beats and it moved leftward too.

But when the contraction was considered, the APD node may move rightward during the stabilization (Figure **4**-**5** and Figure **4**-**6**). In Figure **4**-**5** where both ends were fixed, one APD node was first formed at the left end and moved rightward. After about 10 beats, another node was formed close to the right end, and then both ends moved rightward. In Figure **4**-**6** where right end was free, an APD node moved rightward and finally disappeared. Whenever the right end was fixed or free, APD nodes typically move rightward, opposite to the phenomenon observed when no contraction was considered.

Moreover, when the contraction is considered and both ends are fixed, quasiperiodic solutions are often obtained after a long time of simulation. For example, when a 10cm fiber was paced at BCL=320ms, a quasiperiodic solution was observed, as shown in Figure **4**-**7**.

46
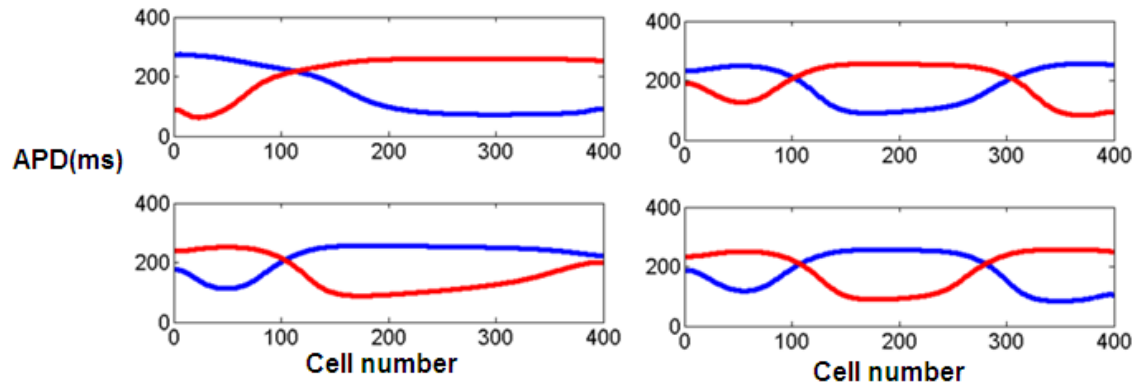
Figure 4-4. Evolution of spatial distributions of APD nodes when no contraction is considered. The cable was paced at the left edge. The spatial distribution for even (red) and odd (blue) beats are shown for stimulus numbers 2, 3 (left-up), 15, 16 (left-down), 50, 51 (right-up), and 300, 301 (right-down). The APD nodes move leftward as simulation goes on. New APD nodes may be formed at right end during the process, as shown in this example. The fiber is paced at BCL=315ms, and fiber length is 10cm.
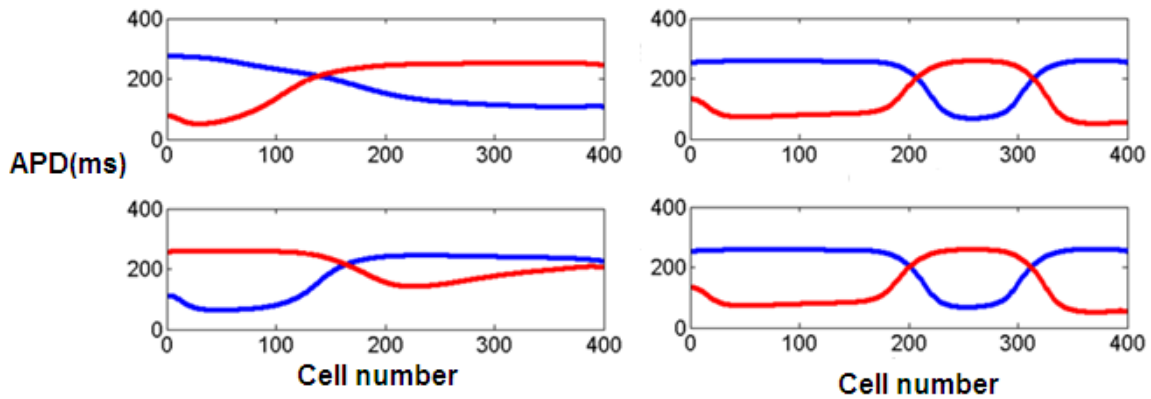


Figure 4-5. Evolution of spatial distributions of APD nodes when contraction is considered and both ends are fixed. The cable was paced at the left edge. The spatial distribution for even (red) and odd (blue) beats are shown for stimulus numbers 2, 3 (left-up), 5, 6 (left-down), 50, 51 (right-up), and 300, 301 (right-down). Opposite to Figure 4.4, the APD nodes move rightward as simulation goes on. The fiber is paced at BCL=315ms, and fiber length is 10cm.

47
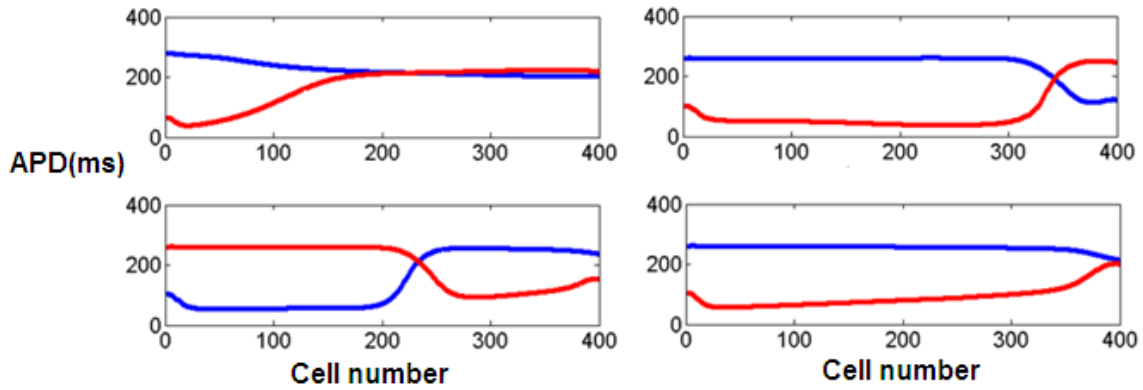
Figure 4-6. Evolution of spatial distributions of APD nodes when contraction is considered and right end is free. The spatial distribution for even (red) and odd (blue) beats are shown for stimulus numbers 2, 3 (left-up), 15, 16 (left-down), 30, 31 (right-up), and 300, 301 (right-down). The APD nodes move rightward as simulation goes on. The fiber is paced at BCL=315ms, and fiber length is 10cm.
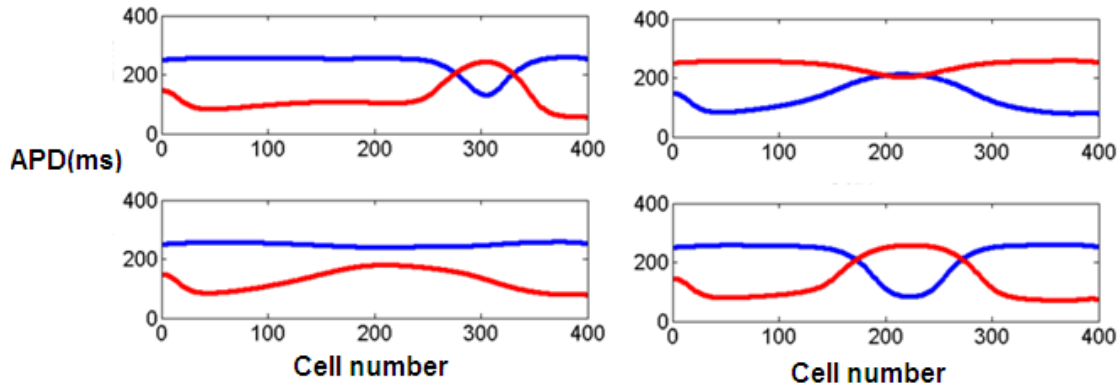


Figure 4-7. Quasiperiodic solutions found when both ends are fixed. Spatial distribution for even (red) and odd (blue) beats are shown for stimulus numbers 330 and 331 (left-up), 350 and 351 (left-down), 355 and 356 (right-up), 360 and 361 (right-down)

In addition, in Figure **4-8**, the rightmost node always kept stationary while the other two moved rightward. This phenomenon is commonly observed when contraction is considered and both ends are fixed, and such node is called "hard node". Figure **4-8** demonstrated this phenomenon with a fiber of 14cm paced at BCL=320ms.

## 4.4 Summary

In this chapter, the effects of the electro-mechanical coupling on cardiac alternans have been investigated. The results showed that, the discordant alternans is induced by the interaction of conduction velocity and action potential duration restitution at high pacing rates, no matter whether contraction is considered or not; however, when contraction is considered, the formation of the discordant alternans is in a very different way, and it's dependent on the boundary conditions.

In the future, the studies can be extended to tissues and the difference in the APD distributions as well as in the formation of APD nodal line between tissues with and without mechanics can be investigated.
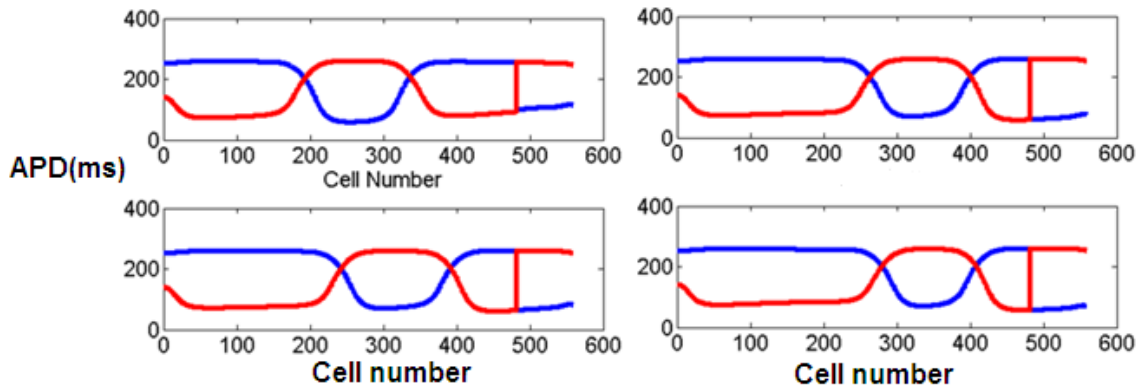


Figure 4-8. Hard nodes found when both ends are fixed. Fiber is 14cm and BCL is 320ms. Spatial distribution for even (red) and odd (blue) beats are shown for stimulus numbers 310 and 311 (left-up), 350 and 351 (left-down), 370 and 371 (right-up), 390 and 391 (right-down)

# CHAPTER 5
# ELECTRODE MISPLACEMENT DURING ECG COLLECTION

## 5.1 Overview

Artifacts in ECG due to electrode misplacement can lead to wrong diagnoses. Various computer methods have been developed for automatic detection of electrode misplacement.

In this chapter, we will review and compare the performance of two algorithms with the highest accuracies on several databases from Physionet. These algorithms will be implemented into four models. As will be shown in this chapter, for clean ECG records with clearly distinguishable waves, the best model can produce excellent accuracies (>=0.984) for all misplacements except the LA/LL interchange (0.874); however, the accuracies will be significantly lower for records with noises and arrhythmias. Moreover, this study will show that when the algorithms are tested on a database that is independent from the training database, the accuracies may be poor. For the worst scenario, the best accuracies for different types of misplacements can range from 0.361 to 0.784.

Given that a large number of ECGs of various qualities and pathological conditions are collected every day, more robust and accurate algorithms shall be developed for automatic detection of electrode misplacement to improve the quality of health care. Very importantly, the model shall be developed and tested using a database of extensive ECG records. Towards that aim, we developed an algorithm for automatic detection of electrode misplacement and evaluated its performance under various practical considerations.

As will be explained in the chapter, the algorithm consists of two discrimination steps. Step 1 determines whether an ECG has been correctly collected. If the prediction of Step 1 is misplacement, Step 2 then determines what the type of misplacement is. Previous algorithms reported their performances on a database including equal number of misplaced and correct records. We will show that those algorithms may have high false alarm rate on misplacement prediction. Resampling will be conducted at both the training and test sets for faithful evaluation and for optimal performance. The performance of Step 1 is 99.6% accuracy, 91.7% sensitivity, 99.9% specificity, 98.9% positive predictive value and 99.7% negative predictive value. The overall accuracy of Step 2 is 90.4%.

## 5.2 Electrode misplacement

Various types of electrode misplacement are first reviewed here. The misplacement of precordial electrode cables occurs much less frequently than

the misplacement of limb electrodes [80]. In this work, we considered only misplacements of limb electrodes. Recall that, we use RA, LA, LL, and RL to represent the electrodes that are supposed to be placed on the right arm (r.a.), left arm (l.a.), left leg (l.l.), and right leg (r.l.), respectively. A few selected examples of electrode placements are shown in Figure 5-1. Panel (a) shows the correct placement. Panel (b) shows the misplacement where LA and RA are reversed. We denote this misplacement by LA/RA. Panel (c) shows the misplacement where RA takes the supposed place of LA, LA takes the supposed place of LL, and LL takes the supposed place of RA. We denote this misplacement by RA>LA>LL>RA. Note this misplacement can be regarded as a one-step clockwise rotation of RA, LA, and LL from the correct placement.

The 4 limb cables have 24 different permutations of placement on the 4 limbs. Table 5-1 shows all 24 types of placement and their shorthand representations using the abbreviated notations introduced in Figure 5-1. Note that all cable reversals are derived from operations on the correct electrode placement. Moreover, certain types of misplacement are obtained using two simultaneous operations. For example, the placement type 8 involves the interchange between LL and RL as well as the interchange between LA and RA. In the standard 12-lead ECG, leg electrodes ought to be placed at the ankles. The potential difference between the two ankles is essentially zero. Therefore, reversing the two electrodes on the ankles will not change the ECG. As a result, the 24 different types of electrode placement yield 12 different ECGs. The last column of Table 5-1 shows the equivalent relationships between the different types of placement.
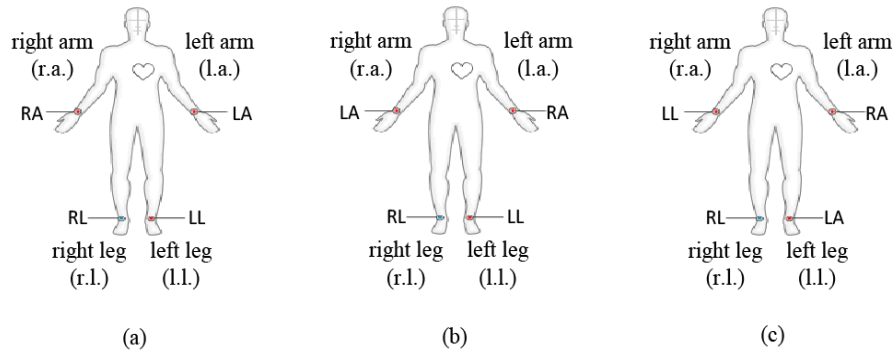


Figure 5-1. Examples of selected electrode placements. We use RA, LA, LL, and RL to represent the electrodes that are supposed to be placed on right arm (r.a.), left arm (l.a.), left leg (l.l.), and right leg (r.l.), respectively. Panel (a) shows the correct placement. This layout can be represented by RARLHLLLA. Panel (b) shows the misplacement where LA and RA are reversed. This reversal operation is denoted by LA/RA and the resulting layout is represented by LARLHLLRA. Panel (c) shows the misplacement where RA takes the supposed place of LA, LA takes the supposed place of LL, and LL takes the supposed place of RA.

Table 5-1. List of all 24 permutations of 4 limb electrodes. See Figure 5-1 for definitions of the abbreviations and explanations of the shorthand notations.

| Limb | | r.a. | l.a. | r.l. | l.l. | Cable Reversal | Layout | 👤 |
|---|---|---|---|---|---|---|---|---|
| Electrode placement | 1 | RA | LA | RL | LL | None | $^{RA}_{RL}\mathbf{H}^{LA}_{LL}$ | 13 |
| | 2 | LA | RA | RL | LL | LA/RA | $^{LA}_{RL}\mathbf{H}^{RA}_{LL}$ | 14 |
| | 3 | LL | LA | RL | RA | RA/LL | $^{LL}_{RL}\mathbf{H}^{LA}_{RA}$ | 15 |
| | 4 | RA | LL | RL | LA | LA/LL | $^{RA}_{RL}\mathbf{H}^{LL}_{LA}$ | 16 |
| | 5 | LL | RA | RL | LA | RA>LA>LL>RA | $^{LL}_{RL}\mathbf{H}^{RA}_{LA}$ | 17 |
| | 6 | LA | LL | RL | RA | RA>LL>LA>RA | $^{LA}_{RL}\mathbf{H}^{LL}_{RA}$ | 18 |
| | 7 | RA | RL | LL | LA | LA/RL, LA/LL | $^{RA}_{LL}\mathbf{H}^{RL}_{LA}$ | 19 |
| | 8 | LA | RL | LL | RA | LA/RL, RA>LL>LA>RA | $^{LA}_{LL}\mathbf{H}^{RL}_{RA}$ | 21 |
| | 9 | LL | RL | RA | LA | LA/RL, RA>LA>LL>RA | $^{LL}_{RA}\mathbf{H}^{RL}_{LA}$ | 20 |
| | 10 | RL | RA | LL | LA | RA/RL, RA>LA>LL>RA | $^{RL}_{LL}\mathbf{H}^{RA}_{LA}$ | 22 |
| | 11 | RL | LA | LL | RA | RA/RL, RA/LL | $^{RL}_{LL}\mathbf{H}^{LA}_{RA}$ | 24 |
| | 12 | RL | LL | RA | LA | RA/RL, LA/LL | $^{RL}_{RA}\mathbf{H}^{LL}_{LA}$ | 23 |
| | 13 | RA | LA | LL | RL | LL/RL | $^{RA}_{LL}\mathbf{H}^{LA}_{RL}$ | 1 |
| | 14 | LA | RA | LL | RL | LL/RL, LA/RA | $^{LA}_{LL}\mathbf{H}^{RA}_{RL}$ | 2 |
| | 15 | LL | LA | RA | RL | LL/RL, RA/LL | $^{LL}_{RA}\mathbf{H}^{LA}_{RL}$ | 3 |
| | 16 | RA | LL | LA | RL | LL/RL, LA/LL | $^{RA}_{LA}\mathbf{H}^{LL}_{RL}$ | 4 |
| | 17 | LL | RA | LA | RL | LL/RL, RA>LA>LL>RA | $^{LL}_{LA}\mathbf{H}^{RA}_{RL}$ | 5 |
| | 18 | LA | LL | RA | RL | LL/RL, RA>LL>LA>RA | $^{LA}_{RA}\mathbf{H}^{LL}_{RL}$ | 6 |
| | 19 | RA | RL | LA | LL | LA/RL | $^{RA}_{LA}\mathbf{H}^{RL}_{LL}$ | 7 |
| | 20 | LL | RL | LA | RA | LA/RL, RA/LL | $^{LL}_{LA}\mathbf{H}^{RL}_{RA}$ | 9 |
| | 21 | LA | RL | RA | LL | LA/RL, LA/RA | $^{LA}_{RA}\mathbf{H}^{RL}_{LL}$ | 8 |
| | 22 | RL | RA | LA | LL | RA/RL, LA/RA | $^{RL}_{LA}\mathbf{H}^{RA}_{LL}$ | 10 |
| | 23 | RL | LL | LA | RA | RA/RL, RA>LL>LA>RA | $^{RL}_{LA}\mathbf{H}^{LL}_{RA}$ | 12 |
| | 24 | RL | LA | RA | LL | RA/RL | $^{RL}_{RA}\mathbf{H}^{LA}_{LL}$ | 11 |

Table 5-2 shows the lead readings of the ECGs from various types of misplacement compared to those of the correct ECG. The 24 types of placement yield 12 different ECGs since the left and right ankles have the same potential; see Table 5-1. Thus, Table 5-2 shows only the results of the 12 different ECGs. Type 1 placement corresponds to the correct ECG placement, and the reading of each lead is the correct reading. Readings of ECGs of misplacement are compared to the readings of the correct ECG. In theory, the last 6 rows of Table 5-2 are trivial to detect since one of the leads in these ECGs is a flat line since one of the arm electrodes is placed on the right leg.

## 5.3 Data

Three open-source databases from Physionet [139] were adopted for numerical studies. The St.-Petersburg (StP) Institute of Cardiological Technics 12-lead Arrhythmia Data includes 75 annotated recordings extracted from 32 Holter records [139][141]. Each record is 30 minutes long and is sampled at 257 Hz. The ECGs were collected from 46 patients, among which 2 were with Acute MI, 5 were with Transient Ischemic Attack, 4 were with Prior MI, 7 were with Coronary Artery Disease with Hypertension, 1 was with Sinus Node Dysfunction, 18 were with Supraventricular Ectopy, 3 were with Atrial Fibrillation or SVTA, 2 were with WPW, 1 was with AV Block, and 3 were with Bundle Branch Block. For each record, we removed the first two seconds and the last two seconds and then we divided each of record into 10-second segments, which produces 13,425 10-second records.

Table 5-2. ECGs from various types of misplacement compared to the correct ECG.

| | | | Lead Reading | | | | | | |
|---|---|---|---|---|---|---|---|---|---|
| | | Cable Reversal | "I" | "II" | "III" | "AVR" | "AVL" | "AVF" | "V1-V6" |
| Electrode placement | 1 | None | I | II | III | AVR | AVL | AVF | V1-V6 |
| | 2 | LA/RA | -I | III | II | AVL | AVR | AVF | Unchanged |
| | 3 | RA/LL | -III | -II | -I | AVF | AVL | AVR | Unchanged |
| | 4 | LA/LL | II | I | -III | AVR | AVF | AVL | Unchanged |
| | 5 | RA>LA>LL>RA | III | -I | -II | AVL | AVF | AVR | Unchanged |
| | 6 | RA>LL>LA>RA | -II | -III | I | AVF | AVR | AVL | Unchanged |
| | 7 | LA/RL, LA/LL | II | II | 0 | -II | II/2 | II/2 | Distorted |
| | 8 | LA/RL, RA>LL>LA>RA | -II | 0 | II | II/2 | -II | II/2 | Distorted |
| | 9 | LA/RL, RA>LA>LL>RA | 0 | -II | -II | II/2 | II/2 | -II | Distorted |
| | 10 | RA/RL, RA>LA>LL>RA | III | III | 0 | -III | III/2 | III/2 | Distorted |
| | 11 | RA/RL, RA/LL | -III | 0 | III | III/2 | -III | III/2 | Distorted |
| | 12 | RA/RL, LA/LL | 0 | -III | -III | III/2 | III/2 | -III | Distorted |

The records in the Physikalisch-Technische Bundesanstalt (PTB) Diagnostic ECG Database were collected from healthy volunteers and patients with different heart diseases [139][140]. The ECGs were obtained using a non-commercial PTB prototype recorder at a sampling rate of 1000 samples per second. The recorder has 16 input channels, among which 14 are used for ECGs, 1 for respiration, and 1 for line voltage. The resolution of the recorder is 16 bit with 0.5 μV/LSB, and the bandwidth is 0-1 kHz. The PTB Diagnostic ECG Database consists of 549 records from 290 subjects (148 Myocardial Infarction, 18 Cardiomyopathy/Heart failure, 15 Bundle Branch Block, 14 Dysrhythmia, 7 Myocardial Hypertrophy, 6 Valvular Heart Disease, 4 Myocarditis, 4 Miscellaneous, 52 Healthy Controls, and 22 subjects unclassified). The record lengths varied from 32 to 120 seconds, and we divided each record into 10-second long segments. The resulting 5520 records were used in studies below.

The Computing in Cardiology/Physionet 2011 Challenge provided 3 data sets for participants of the event to develop computer algorithms that could improve the quality of ECGs. Records from set A of the Challenge were selected to be used here. This set consists of 1000 standard 12-lead ECG recordings. Each record is 10 seconds long and is sampled at 500 Hz with 16-bit resolution. According to the signal quality, Physionet annotators labeled 775 of the records as acceptable, 223 records as unacceptable, and 2 records as indeterminate. Note that a record with noises and other artifacts may have been labeled as acceptable if the Physionet annotators believed the record quality to be sufficient for doctors to make accurate diagnosis [142]. In order to obtain a database of clean and clear signals, we have reexamined the acceptable records and excluded those records with significant artifacts. The following criteria were adopted for selection of records that are to be included: 1.) a record cannot have significant flat-line segments or segments that are off the chart; 2.) a record cannot have large measurement noises; and 3.) amplitudes of the leads cannot be too small. Using these criteria, each author independently reviewed the 775 acceptable records, and only the 383 records that had been accepted by all authors were included in a database for the study shown below.

The three databases are significantly different. The Physionet 2011 Challenge dataset contains only clean and clear signals. Both the PTB Database and the StP Database contain many episodes of arrhythmias. All of the StP records were collected from patients with certain heart disease, whereas part of the PTB records were from healthy subjects. Moreover, the StP records were recorded with Holter recorders from ambulatory patients at a low sampling rate of 257Hz, whereas the PTB records were recorded at a high rate of 1000Hz and were recorded with the specially designed non-commercial PTB prototype recorder.

# 5.4 Distinction between correct and wrong placements

## 5.4.1 Overview

Figure 5-2 shows the flowchart of the overall algorithm. During the preprocessing stage, artifacts will be removed from the ECG and then the ECG is delineated to detect the heartbeats. Then features are extracted from each record. During the stage of classification, the artificial neural network is used to report the possibility of an ECG record being collected with certain type of misplacement.

## 5.4.2 Preprocessing: ECG enhancement

ECG signals are often contaminated by powerline interference and baseline wandering [146]-[147]. Before testing an ECG against a detection algorithm, we first enhanced the signal quality of the ECG. Specifically, a low-pass filter was adopted to suppress high-frequency powerline noises and a high-pass filter was applied to remove low-frequency baseline wander.

Common ECG artifacts include 50 or 60 Hz power-line frequency noise [151], baseline instability, muscle noise, and large swings in baseline due to electrode movement [152][153]. Many techniques have been developed to enhance ECG signals. A few authors demonstrated that signal-to-noise ratio (SNR) can be improved by simple frequency-selective filtering [154]-[156]. To overcome the difficulties due to partial overlap of signals and noise bandwidths [157]-[159] proposed a method based on a Kalman filter with adaptive noise-covariance estimation, which is able to improve the SNR and at the same time preserve important morphological variations.
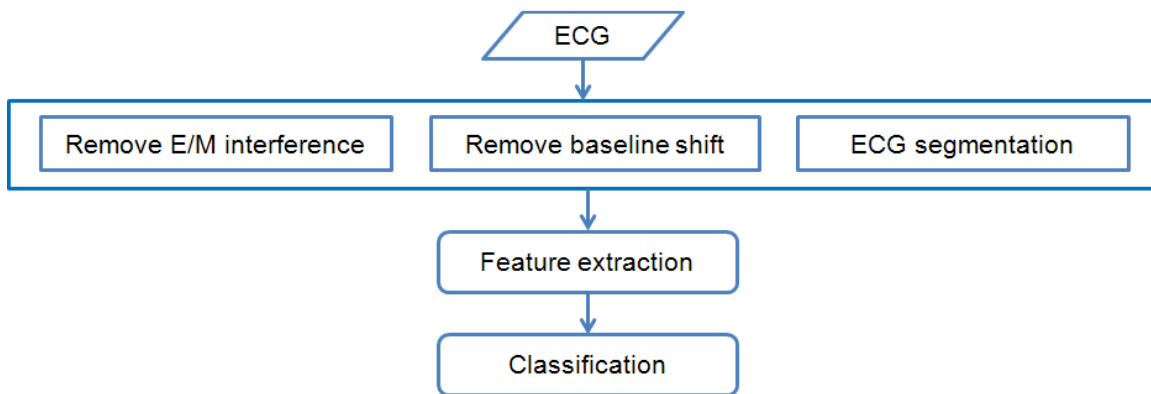


Figure 5-2: Flowchart of the algorithm for distinction between correct and wrong placements

The preprocessing operation is motivated to more accurately detect electrical waves in the ECG to provide basic physiological and rhythmic information. Such information may be crucial for monitoring states of a patient and online diagnosis of diseases.

The ECG signal is often contaminated by 50 or 60 Hz powerline (AC) interference. Typically, a fixed or adaptive notch filter [160]-[162] is used to reduce the AC interference. Causes for the baseline wander include breath, patient's movement and varying electrode-skin impedance [163]. The frequency range of baseline wander is usually less than 1.0 Hz. Because of the very low frequency range of the baseline wander, a simple and frequently used method for reducing baseline wander is the high-pass filtering based on a moving average filter [164].

We first apply a low-pass filter to suppress high-frequency noises and then further enhance the signal by applying a high-pass filter to remove baseline wander. We adopt a low-pass moving average filter [146] to reduce the AC interference:

$$y_n = \frac{1}{2M + 1} \sum_{i=-M}^{M} x_{n+i}$$

where $x_n$ represents the original signal and $y_n$ represents the enhanced signal. The length of the moving average window is $2M+1$ and $M=4$ is chosen to filter high frequency noises. Then, we adopt a modified moving average (MA) filter for the baseline wander reduction [147]:

$$\bar{y}_n = \frac{1}{2N + 1} \sum_{i=-N}^{N} y_{n+i}$$
$$z_n = y_n - \bar{y}_n$$

where $y_n$ is the processed signal after removal of AC interference, $\bar{y}_n$ represents a moving average of $y_n$, and $z_n$ is the final enhanced signal. Signal samples with extreme amplitudes in the observation window may cause the filter to introduce signal distortion, so we first exclude samples with extreme amplitudes in each window. Because of the possible overlapping between the ECG signal and the disturbance spectra, signals might be distorted after the filtering. To balance the performance of the removal of the baseline wander and the signal distortion, we choose N=100. Figure **5**-**3** shows a sample ECG signal to demonstrate the enhancement of quality.

To compare with the diagnostic ECG bandwidth, we conduct a frequency response analysis of the moving average filters [165]. For the low pass filter, the pass-band and the stop-band frequencies are 25Hz and 55Hz, respectively. For the high pass filter, the pass-band and the stop-band frequencies are 0.6Hz and

0.01Hz, respectively. Since the filters may change the bandwidth of the ECG signal and cause discrepancy such as ST segment shifts [166], one shall apply filtering with caution. We suggest that the raw ECG record be presented to doctors for medical diagnosis after the quality evaluation is done.

### 5.4.3 Physiological Features and ECG wave measurements

A typical ECG tracing consists of various waves and intervals, including peak-to-peak amplitude, P axis, QRS axis, QRS area, QRS amplitudes with various delays after QRS onset, T sum, as well as the amplitudes of Q, R, S and T [54]. These waves and intervals represent important physiological measurements and have been used by various authors to detect electrode misplacements [61].

A variety of algorithms have been developed for delineation of P wave, QRS-complex, and T wave; see introduction in Clifford et al. (2006) [148]. In this work, we adopted a delineation method based on wavelet transform [149]. Another commonly used algorithm is available in the GPL software, ecgpuwave, from PhysioToolkit [150].

Standard, important features of an ECG include the P wave, the QRS complex, and the T wave. For clinical diagnosis, RR interval and QR interval are the two most important intervals [148]. Many techniques have been developed to detect various ECG waves. One of the earliest algorithms was developed by Pan and Tompkins (1985) [167], which recognizes QRS complexes based upon digital analyses of slope, amplitude, and width of the signal. Other common wave detection algorithms include signal matched filters [168], time-frequency decomposition methods [169], neural networks [170], genetic algorithms [171], and hidden Markov models [148].

More recently, wavelet transform has proven to be a reliable method for ECG segmentation. With the multiscale feature of wavelet transform, the QRS complex can be distinguished from high P or T waves, noise, baseline drift, and artifacts, and various parts of the ECG signals can be measured, especially the location of onset and offset of QRS complex and P and T waves [172]-[173]. Analyses based on wavelet transform has been used in ECG signal processing for the determination of timing intervals, the detection of abnormalities, the analysis of heart rate variability and cardiac arrhythmias, and the signal compression [174].

57
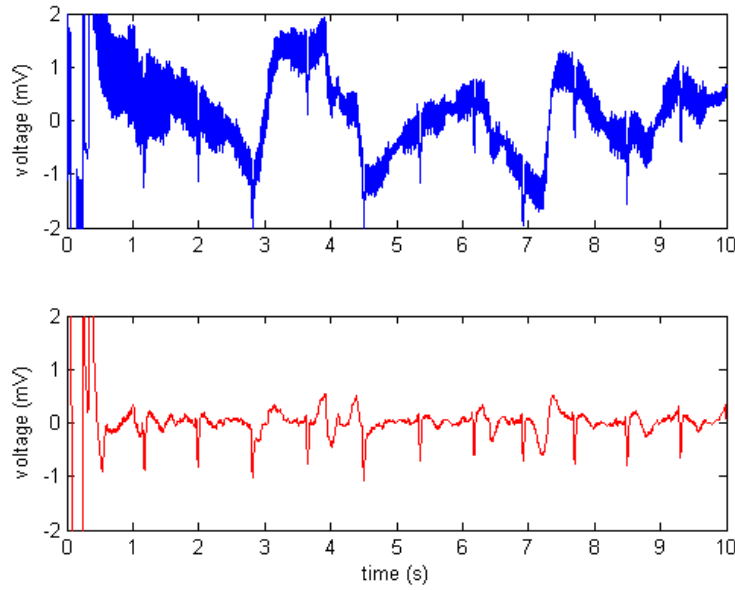
Figure 5-3. A sample ECG showing the quality of a signal with powerline interference and baseline instability (top) can be significantly improved by enhancement approaches (bottom).

To facilitate subsequent tests, we first segment a record into beats and identify the important waveforms. Methods based on wavelet transform [149] are selected for this purpose due to their convenience and reliability. Wavelet transform is a form of time-frequency representation of time series signals. Unlike Fourier transform, which extracts global information based on time averaging, wavelet transform can simultaneously capture both global and localized information in time and frequency domains. The continuous wavelet transform of a continuous, square-integrable function x(t) can be expressed by the following integral [175]

$$T(a, b) = \frac{1}{\sqrt{a}} \langle x(t), \varphi^* \left( \frac{t - b}{a} \right) \rangle = \frac{1}{\sqrt{a}} \int_{-\infty}^{+\infty} x(t) \varphi^* \left( \frac{t - b}{a} \right) dt$$

where the mother wavelet $\varphi(t)$ is a continuous function in both the time domain and the frequency domain, $\varphi^*$ represents the complex conjugate of $\varphi$, and a and b represent the scale and translational value of the transform, respectively.

Standard approaches for ECG segmentation consist of several successive stages to find the ECG waveform feature boundaries [176]. In the first stage, the R peaks are located in the ECG signal utilizing a QRS detection algorithm such as the Pan and Tompkins algorithm [167]. The next stage is to search forwards and backwards from the location of the R peak in each ECG beat to estimate the

58

location of the onset and offset boundaries for other ECG features like the P wave, T wave and U wave.

Several steps are taken for the QRS detection: First, we divide the whole signal to several segments each of which has a length of 1 second. Each segment is then examined to search for QRS complexes. Next, the CWT is computed within a selected frequency interval of 20.8Hz – 25Hz, which is chosen by parameter studies. Then, the modulus maxima of the CWT are extracted. The modulus maxima are defined as the maxima of the $|T(a,b)|^2$ averaged over the frequency interval. We chose a preset threshold corresponding to a fixed percentage of the maxima, and values below the preset threshold are reset to zero. The threshold is chosen to be 20% based on parameter studies. Separated bands of survived values will remain. Note that, when the heart rate is larger than 60 beats per minute, more than one band will remain in some segments. In the top of Figure **5**-**4**, the red points indicate the locations of the R peaks detected. The middle of Figure **5**-**4** shows those bands represented by bright colors, and in the bottom of Figure **5**-**4**, the squared WT coefficients $|T(a,b)|^2$ that are averaged over frequency only exist at locations of the QRS complexes. In this way, we will be able to identify the ranges of the QRS complexes. Then we pick out the R peaks from each QRS complex by the amplitudes. After we have obtained the R peaks, we drop the beats with significantly smaller R peaks, so that when the heart rate is smaller than 60 beats per minute, we wouldn't mistakenly detect any beats. An example of segmentation result is shown in Figure **5**-**4**.
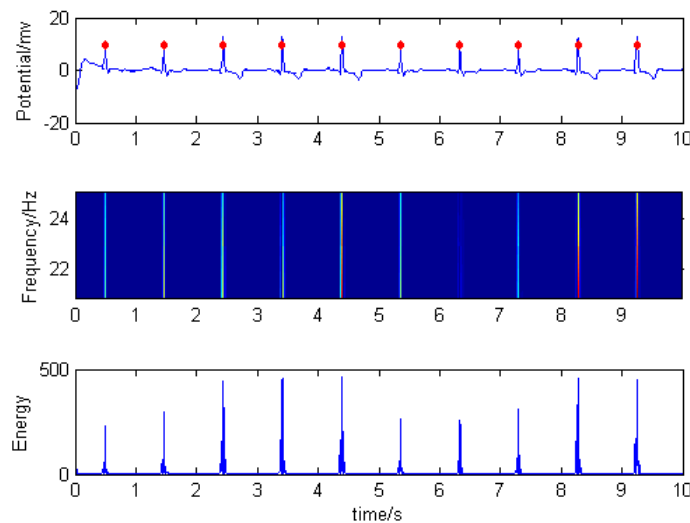


Figure 5-4. An example of ECG segmentation using wavelet transform.

To compute the CWT, we have used the Mexican hat wavelet. The Mexican hat wavelet is the second derivative of a Gaussian function, defined as

$$\varphi(t) = (1 - t^2)e^{\frac{t^2}{2}}$$

Similar approaches are taken to identify T and P waves. To identify the T wave between two subsequent beats, we assume that the T wave exists between 0.2 s after the first R wave and the middle of the two R waves. We find the modulus maximum in the frequency range of 3.9063-7.8125Hz and mark the corresponding time as the peak of the T wave. Then, we assume the P wave exists between the T wave of the previous beat and the R wave of the next beat. The frequency interval for the detection of the P wave is 3.9063-7.8125Hz. Numerical studies show the detected waves are reliable.

To ensure accurate estimation of these physiological parameters, we cross validated the lineation results from an open-access software ecgpuwave [150] and the results from our wavelet-based in-house method described above.

We extracted all available waves and intervals in an ECG as physiological features, which were used in the following classification approach.

### 5.4.4 Correlation-based Features

Inter-lead correlations are important parameters for ECG analysis [148]. The standard 12-lead ECG has 6 limb leads and 6 precordial leads. Among the 6 limb leads, only 2 are independent. One can arbitrarily choose 2 out of the 6 limb leads and then the other 4 leads can be exactly computed from linear combinations of the chosen 2. The 6 precordial leads are generally independent of each other and independent to the limb leads. Therefore, the 12-lead ECG can be reduced to a set of 8 independent leads (6 precordial and 2 limb leads). Apparently, there are multiple ways to reduce the 12-lead ECG to an 8-lead counterpart. Nevertheless, all the reductions are equivalent to one another. Now, any lead in the 8-lead reduction can be predicted from the other 7 leads using a regression model. Moreover, it is hypothesized that this regression model is a universal model for all records that are correctly collected. Based on this hypothesis, parameters of this universal model can be estimated by fitting it to all correct ECGs in the database. Various types of regression models can be adopted for this purpose [179][182]. Here, we used a simple linear regression model. The correlation between a lead and its reconstruction would tend to be high if the ECG is correctly collected or otherwise the correlation would tend to be low. For example, Figure 5-5 shows the reconstruction of lead II of a correct ECG (left) and the reconstruction of lead II of a misplaced ECG (right). While the reconstruction and the original signals in the left panel are consistent, the reconstruction and the original signal in the right panel clearly have opposite

phases. Since inter-lead correlations do not rely on specific ECG waves and intervals, we call correlation-based features non-physiological.
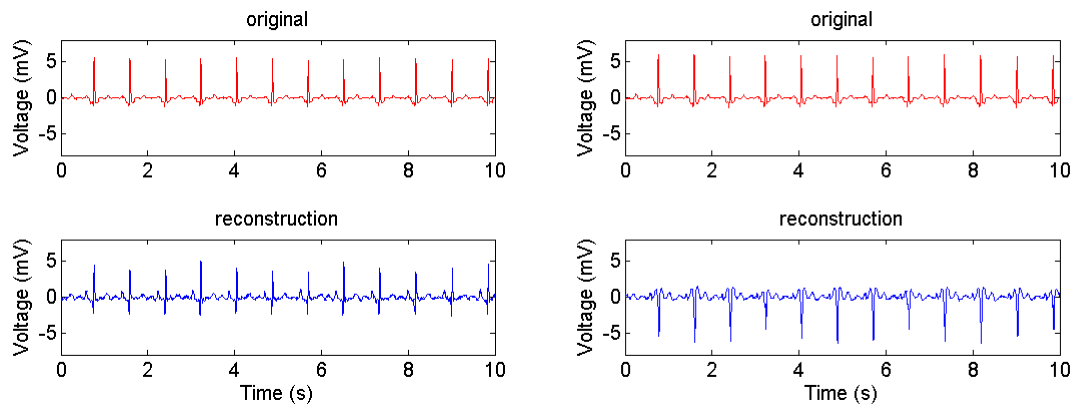


Figure 5-5: Left: reconstruction of lead II of a correctly collected ECG. Note the reconstruction and the original signals have highly correlated patterns. Right: reconstruction of lead II of an ECG collected with LA/RA reversal. Note waves in the reconstruction are opposite to those in the original signals, indicating poor correlation.

### 5.4.5 Models for detection of electrode misplacement

We compared the algorithm of Heden et al. (1995, 1996) [143]-[144] which used the physiology based features and that of Kors and Herpen (2001) [145] which used correlation based features on their performance for detection of limb electrode misplacement. As indicated in Table **5**-**2**, the interchange between right leg and an arm electrode results in an ECG with a flat line lead. We did not consider such scenarios since they are trivial to identify using derived misplacement data. Instead, we investigated only the placement types 1-6 shown in Table 5-2. We aim to distinguish between the correct ECG and each of the 5 types of misplacement.

Heden et al. (1995) [143] were the first to use artificial neural network models of automatic detection of electrode misplacement. Their models used the physiology based features as explained in 5.4.3. Their studies were based on a database of 11,432 ECGs from patients at the university hospital in Lund during 1992 and 1993. Approximately 500 ECGs were further excluded because they were either technically deficient or were collected with lead reversals. When P waves were present, they measured the P axis, peak-to-peak amplitude (maximal positive amplitude – |maximal negative amplitude|), QRS axis, QRS area in lead I and lead V6, QRS amplitude 35, 40 and 45 ms after QRS onset, and T sum in lead I and V6, and used these measurements as features for classification. When P waves were absent, they used measurements including QRS axis, QRS area in lead I, Q and R amplitudes in lead I, etc., as features. When classifying the reversal of LA/RA, they obtained a specificity of

0.9995±0.00017 and sensitivity of 0.9911±0.00080 when the P wave was present, and a specificity of 99.92± 0.023 and sensitivity of 94.5 ± 0.52 when the P wave was absent. Heden et al. (1996) [144] later extended the neural network model to detect more misplacements, including the interchanges LA/LL, V1/V2, V2/V3, V3/V4, V4/V5, and V5/V6. They used the Q, R, S and T amplitudes and the QRS axis as features, and input these features into an artificial neural network. They then obtained a specificity of 57.6% and sensitivity of 99.97% for the reversal of left arm and left leg, and a specificity of 71.76% and sensitivity of 99.92% on average for the precordial lead reversals.

Kors and Herpen (2001) [145] proposed to detect ECG electrode misplacement using the correlation based features explained in 5.4.4. They developed a set of decision rules using an induction algorithm based on Classification and Regression Trees [183].  Kors and Herpen investigated 14 types of misplacement including the 5 types of limb cable reversals and 9 types of precordial cable reversals. On a set of 3,305 ECGs, they demonstrated excellent specificities (>=99.5%) for all 14 types of misplacement and very good sensitivities (>=93%) for all interchanges except the LA/LL reversal (sensitivity = 17.9%, specificity = 99.5%).

The algorithm of Heden et al. (1995, 1996) [143]-[144] and that of Kors and Herpen (2001) [145] were implemented in 4 models; see description in Table **5-3**. In model 1, we directly applied the decision rules presented in [145]. In model 2, we developed a neural network classification model using features derived according to [145]. In model 3, we developed a neural network classification model using features according to Heden et al. (1995, 1996) [143]-[144]. In model 4, we combined the features from Kors and Herpen (2001) [145] and the features from Heden et al. (1995, 1996) [143]-[144] into a neural network classification model.

Table 5-3. Description of the models used in this work

| Model | Description |
|---|---|
| Model 1 | Direct application of the decision rules from Kors and Herpen (2001) [145] |
| Model 2 | A neural network model using features from Kors and Herpen (2001) [145] |
| Model 3 | A neural network model using features from Heden et al. (1995, 1996) [143]-[144] |
| Model 4 | A neural network model using combined features from Kors and Herpen (2001) and from Heden et al. (1995, 1996) [143]- [145] |

### 5.4.6 Neural network classification

We implemented the algorithm of Heden et al. (1995, 1996) and that of Kors and Herpen (2001) [143]- [145] using artificial neural network models for comparison. An artificial neural network is a model inspired by biological neural networks. It is widely used in many problems, including signal filtering [170], adaptive control [177], optimization [178], physiological signal reconstruction [179], and pattern detection [180].

The neural network toolbox in Matlab [181] was utilized in this work. We used a two-layer pattern recognition network. When implementing the algorithm of Kors and Herpen (2011), which includes 12 features, we used 10 neurons in the hidden layer. We used 20 neurons in the hidden layer when implementing the algorithm of [143]-[144], which includes 24 features. We used 20 neurons in the hidden layer when implementing a method that combines features from [145] and those from Heden et al. [143]-[144]. We adopted the "trainlm" function for back-propagation training to update weight and bias states.

### 5.4.7 Results

Two experiments were designed to investigate the four models. Experiment 1 examined the 4 models on each of the 3 databases individually. Experiment 2 examined cross-database prediction, where a model was trained using one database and tested on another database. Recall again that model 1 adopted the specific decision rules obtained by [145]; therefore, there is no training in this article for model 1. Models 2-4 are trained on current databases using previously presented features.

In order to improve the specificity of their algorithms, the work of [145] and that of [143]-[144] intentionally used imbalanced training data, which included significantly more correct ECG records than misplacement records. The rationale was that a vast majority of clinically collected ECGs are correct ECGs. Thus, an extremely high specificity is desired. Since the goal of this article is to evaluate the overall performance of the algorithms, we used equal numbers of correct and misplacement records in training.

The PTB Database and the StP Database both contain long ECG records. The original long records were divided into many 10-second segments. Therefore, two short records may be highly correlated if they originated from the same long record. To avoid inferences of such correlation, we deliberately designed the training and test sets so that all records from the same parent record belong to either training set or test set but not both.

Results of experiment 1 are shown in Table **5**-**4**, Table **5**-**5** and Table **5**-**6** for the PTB Database, the StP Database, and the Physionet Challenge database, respectively. Model 1 adopted from [145] was directly applied to each database. For models 2-4, we conducted 10-fold cross validation to avoid over-fitting.

63

Standard deviations of the prediction accuracies are computed from the 10-fold tests.

Comparisons in Table **5**-**4**, Table **5**-**5** and Table **5**-**6** show that results of models 2-4 are substantially more accurate than those of model 1. This is probably because the ECG records used in [145] do not represent well the ECG records used here since the latter are from a broader range of qualities and health conditions. Results of model 3 are in general comparable to those of model 2. For the case of LA/LL reversal, model 3 yields better results than model 2; however, the results from both models are less than satisfactory. Results of model 4 are generally better than both models 2 and 3. Table **5**-**4** and Table **5**-**5** show that the results using the PTB Database are significantly more accurate than those using the StP Database. This is probably because the StP Database contains records of arrhythmias patients. In the studies below, we neglect model 1 and compare the performance of models 2-4.

Results of experiment 2 are presented in Table **5**-**7** to Table **5**-**10**). We first trained the models using all records in the PTB Database and then tested the developed models on records from the StP Database (Table **5**-**7**) and from the Physionet Challenge Database (Table **5**-**8**). Similarly, we trained the models using the StP Database and tested the developed models on the PTB Database (Table **5**-**9**) and on the Physionet Challenge Database (Table **5**-**10**). We did not test the model trained using Physionet Challenge on the other two databases because the number of records in Physionet Challenge (383) is too few compared to the other two databases (5520 and 13425).

Table 5-4: Comparison of various models using the PTB Database

| | | $^{LA}_{RL}\mathbf{H}^{RA}_{LL}$ | $^{LL}_{RL}\mathbf{H}^{LA}_{RA}$ | $^{RA}_{RL}\mathbf{H}^{LL}_{LA}$ | $^{LL}_{RL}\mathbf{H}^{RA}_{LA}$ | $^{LA}_{RL}\mathbf{H}^{LL}_{RA}$ |
|---|---|---|---|---|---|---|
| | | LA/RA | RA/LL | LA/LL | RA>LA>LL>RA | RA>LL>LA>RA |
| Model 1 | Accu | 0.571 | 0.525 | 0.500 | 0.631 | 0.599 |
| | Sens | 0.208 | 0.704 | 0 | 0.637 | 0.203 |
| | Spec | 0.934 | 0.346 | 1 | 0.624 | 0.995 |
| Model 2 | Accu | 0.887±0.050 | 0.945±0.033 | 0.684±0.069 | 0.908±0.045 | 0.949±0.027 |
| | Sens | 0.891±0.057 | 0.941±0.037 | 0.685±0.075 | 0.910±0.041 | 0.950±0.031 |
| | Spec | 0.883±0.045 | 0.949±0.029 | 0.682±0.065 | 0.906±0.051 | 0.948±0.023 |
| Model 3 | Accu | 0.955±0.045 | 0.899±0.074 | 0.742±0.169 | 0.906±0.114 | 0.946±0.045 |
| | Sens | 0.961±0.033 | 0.909±0.088 | 0.766±0.115 | 0.921±0.060 | 0.947±0.051 |
| | Spec | 0.949±0.057 | 0.890±0.059 | 0.718±0.214 | 0.891±0.153 | 0.946±0.042 |
| Model 4 | Accu | 0.981±0.025 | 0.972±0.050 | 0.837±0.097 | 0.958±0.038 | 0.988±0.015 |
| | Sens | 0.978±0.027 | 0.965±0.059 | 0.829±0.092 | 0.965±0.030 | 0.987±0.012 |
| | Spec | 0.984±0.022 | 0.979±0.041 | 0.845±0.106 | 0.979±0.046 | 0.990±0.019 |

Table 5-5: Comparison of various models using the StP Database

| | | ${}^{LA}_{RL}\mathbf{H}^{RA}_{LL}$ | ${}^{LL}_{RL}\mathbf{H}^{LA}_{RA}$ | ${}^{RA}_{RL}\mathbf{H}^{LL}_{LA}$ | ${}^{LL}_{RL}\mathbf{H}^{RA}_{LA}$ | ${}^{LA}_{RL}\mathbf{H}^{LL}_{RA}$ |
|---|---|---|---|---|---|---|
| | | LA/RA | RA/LL | LA/LL | RA>LA>LL>RA | RA>LL>LA>RA |
| Model 1 | Accu | 0.5531 | 0.5615 | 0.5000 | 0.3544 | 0.7069 |
| | Sens | 0.1635 | 0.2522 | 0 | 0.3626 | 0.4366 |
| | Spec | 0.9427 | 0.8708 | 1 | 0.3461 | 0.9772 |
| Model 2 | Accu | 0.663±0.111 | 0.902±0.060 | 0.864±0.113 | 0.922±0.065 | 0.931±0.068 |
| | Sens | 0.683±0.126 | 0.901±0.054 | 0.877±0.069 | 0.926±0.066 | 0.924±0.077 |
| | Spec | 0.642±0.097 | 0.902±0.068 | 0.850±0.148 | 0.919±0.067 | 0.937±0.061 |
| Model 3 | Accu | 0.866±0.134 | 0.889±0.141 | 0.860±0.120 | 0.901±0.128 | 0.881±0.159 |
| | Sens | 0.884±0.123 | 0.851±0.164 | 0.861±0.128 | 0.888±0.139 | 0.920±0.100 |
| | Spec | 0.847±0.148 | 0.927±0.110 | 0.858±0.118 | 0.914±0.121 | 0.842±0.199 |
| Model 4 | Accu | 0.876±0.110 | 0.937±0.086 | 0.887±0.098 | 0.920±0.104 | 0.923±0.132 |
| | Sens | 0.865±0.095 | 0.936±0.106 | 0.877±0.123 | 0.892±0.109 | 0.930±0.168 |
| | Spec | 0.887±0.128 | 0.937±0.059 | 0.896±0.064 | 0.948±0.104 | 0.916±0.093 |

Table 5-6: Comparison of various models using records selected from Physionet Challenge.

| | | ${}^{LA}_{RL}\mathbf{H}^{RA}_{LL}$ | ${}^{LL}_{RL}\mathbf{H}^{LA}_{RA}$ | ${}^{RA}_{RL}\mathbf{H}^{LL}_{LA}$ | ${}^{LL}_{RL}\mathbf{H}^{RA}_{LA}$ | ${}^{LA}_{RL}\mathbf{H}^{LL}_{RA}$ |
|---|---|---|---|---|---|---|
| | | LA/RA | RA/LL | LA/LL | RA>LA>LL>RA | RA>LL>LA>RA |
| Model 1 | Accu | 0.516 | 0.596 | 0.500 | 0.582 | 0.441 |
| | Sens | 0.034 | 0.286 | 0 | 0.603 | 0.045 |
| | Spec | 0.998 | 0.906 | 1 | 0.560 | 0.836 |
| Model 2 | Accu | 0.971±0.065 | 0.977±0.033 | 0.610±0.111 | 0.934±0.220 | 0.970±0.035 |
| | Sens | 0.966±0.091 | 0.983±0.038 | 0.641±0.070 | 0.985±0.020 | 0.966±0.040 |
| | Spec | 0.976±0.025 | 0.971±0.027 | 0.578±0.137 | 0.883±0.310 | 0.973±0.031 |
| Model 3 | Accu | 0.965±0.021 | 0.956±0.039 | 0.859±0.171 | 0.961±0.030 | 0.945±0.071 |
| | Sens | 0.966±0.020 | 0.963±0.038 | 0.829±0.214 | 0.963±0.028 | 0.951±0.057 |
| | Spec | 0.963±0.023 | 0.949±0.040 | 0.888±0.119 | 0.958±0.032 | 0.939±0.085 |
| Model 4 | Accu | 0.995±0.010 | 0.984±0.024 | 0.874±0.101 | 0.993±0.013 | 0.991±0.016 |
| | Sens | 0.998±0.008 | 0.988±0.017 | 0.832±0.117 | 0.993±0.016 | 0.988±0.021 |
| | Spec | 0.993±0.012 | 0.980±0.029 | 0.917±0.062 | 0.993±0.012 | 0.995±0.010 |

Table 5-7. Results of the models, which are trained using records in the PTB Database and tested using records from StP Database

| | | ${}^{LA}_{RL}\mathbf{H}^{RA}_{LL}$ | ${}^{LL}_{RL}\mathbf{H}^{LA}_{RA}$ | ${}^{RA}_{RL}\mathbf{H}^{LL}_{LA}$ | ${}^{LL}_{RL}\mathbf{H}^{RA}_{LA}$ | ${}^{LA}_{RL}\mathbf{H}^{LL}_{RA}$ |
|---|---|---|---|---|---|---|
| | | LA/RA | RA/LL | LA/LL | RA>LA>LL>RA | RA>LL>LA>RA |
| Model 2 | Accu | 0.570 | 0.690 | 0.499 | 0.529 | 0.774 |
| | Sens | 0.490 | 0.750 | 0.490 | 0.482 | 0.789 |
| | Spec | 0.651 | 0.630 | 0.508 | 0.576 | 0.759 |
| Model 3 | Accu | 0.738 | 0.778 | 0.400 | 0.686 | 0.614 |
| | Sens | 0.820 | 0.842 | 0.542 | 0.719 | 0.837 |
| | Spec | 0.656 | 0.713 | 0.258 | 0.654 | 0.391 |
| Model 4 | Accu | 0.660 | 0.765 | 0.412 | 0.599 | 0.733 |
| | Sens | 0.671 | 0.546 | 0.374 | 0.615 | 0.546 |
| | Spec | 0.648 | 0.919 | 0.449 | 0.582 | 0.919 |

Table 5-8. Results of the models, which are trained using records in the PTB database and tested using records from the Physionet Challenge Database

| | | $_{RL}^{LA}\mathbf{H}_{LL}^{RA}$ | $_{RL}^{LL}\mathbf{H}_{RA}^{LA}$ | $_{RL}^{RA}\mathbf{H}_{LA}^{LL}$ | $_{RL}^{LL}\mathbf{H}_{LA}^{RA}$ | $_{RL}^{LA}\mathbf{H}_{RA}^{LL}$ |
| | | LA/RA | RA/LL | LA/LL | RA>LA>LL>RA | RA>LL>LA>RA |
|---|---|---|---|---|---|---|
| Model 2 | Accu | 0.361 | 0.370 | 0.537 | 0.425 | 0.391 |
| | Sens | 0.551 | 0.734 | 0.614 | 0.657 | 0.777 |
| | Spec | 0.171 | 0.005 | 0.459 | 0.193 | 0.006 |
| Model 3 | Accu | 0.354 | 0.784 | 0.431 | 0.590 | 0.503 |
| | Sens | 0.132 | 0.823 | 0.327 | 0.489 | 0.426 |
| | Spec | 0.575 | 0.744 | 0.536 | 0.691 | 0.580 |
| Model 4 | Accu | 0.339 | 0.366 | 0.536 | 0.425 | 0.322 |
| | Sens | 0.455 | 0.723 | 0.618 | 0.519 | 0.637 |
| | Spec | 0.224 | 0.009 | 0.454 | 0.332 | 0.007 |

Table 5-9. Results of the models, which are trained using records in the StP Database and tested using records from the PTB Database

| | | $_{RL}^{LA}\mathbf{H}_{LL}^{RA}$ | $_{RL}^{LL}\mathbf{H}_{RA}^{LA}$ | $_{RL}^{RA}\mathbf{H}_{LA}^{LL}$ | $_{RL}^{LL}\mathbf{H}_{LA}^{RA}$ | $_{RL}^{LA}\mathbf{H}_{RA}^{LL}$ |
| | | LA/RA | RA/LL | LA/LL | RA>LA>LL>RA | RA>LL>LA>RA |
|---|---|---|---|---|---|---|
| Model 2 | Accu | 0.575 | 0.585 | 0.460 | 0.422 | 0.640 |
| | Sens | 0.321 | 0.588 | 0.474 | 0.406 | 0.590 |
| | Spec | 0.828 | 0.581 | 0.447 | 0.438 | 0.689 |
| Model 3 | Accu | 0.929 | 0.645 | 0.486 | 0.642 | 0.749 |
| | Sens | 0.911 | 0.625 | 0.426 | 0.646 | 0.798 |
| | Spec | 0.946 | 0.665 | 0.546 | 0.639 | 0.701 |
| Model 4 | Accu | 0.939 | 0.834 | 0.499 | 0.792 | 0.829 |
| | Sens | 0.946 | 0.827 | 0.477 | 0.735 | 0.924 |
| | Spec | 0.932 | 0.840 | 0.521 | 0.850 | 0.734 |

Table 5-10. Results of the models, which are trained using records in the StP Database and tested using records from the Physionet Challenge Database

| | | $_{RL}^{LA}\mathbf{H}_{LL}^{RA}$ | $_{RL}^{LL}\mathbf{H}_{RA}^{LA}$ | $_{RL}^{RA}\mathbf{H}_{LA}^{LL}$ | $_{RL}^{LL}\mathbf{H}_{LA}^{RA}$ | $_{RL}^{LA}\mathbf{H}_{RA}^{LL}$ |
| | | LA/RA | RA/LL | LA/LL | RA>LA>LL>RA | RA>LL>LA>RA |
|---|---|---|---|---|---|---|
| Model 2 | Accu | 0.751 | 0.266 | 0.593 | 0.445 | 0.305 |
| | Sens | 0.617 | 0.507 | 0.585 | 0.457 | 0.581 |
| | Spec | 0.886 | 0.025 | 0.601 | 0.433 | 0.030 |
| Model 3 | Accu | 0.723 | 0.670 | 0.446 | 0.586 | 0.767 |
| | Sens | 0.798 | 0.779 | 0.536 | 0.622 | 0.757 |
| | Spec | 0.649 | 0.562 | 0.356 | 0.550 | 0.777 |
| Model 4 | Accu | 0.883 | 0.377 | 0.621 | 0.575 | 0.450 |
| | Sens | 0.842 | 0.719 | 0.615 | 0.707 | 0.759 |
| | Spec | 0.925 | 0.034 | 0.627 | 0.444 | 0.141 |

The cross database validation yields much worse results compared to single database results. Records within a database are usually collected by a group of people in similar environments, using similar machines, and for subjects with similar conditions. Therefore, ECG records within a database tend to correlate well whereas records from different databases may not correlate well.

### 5.4.8 Summary

Despite its importance and frequent occurrence, electrode misplacement is not well documented in current cardiology textbooks [55]. As a result, doctors are not well trained to identify artifacts caused by cable reversals. Computer algorithms that can automatically detect cable reversals in ECG will facilitate the doctors to make more accurate diagnosis in a more timely manner.

We have conducted extensive numerical studies to compare the performance of the two best available computer algorithms on electrode misplacements: the algorithm of [143]-[144] which is based on features of ECG waves and the algorithm of [145] which is based on correlation between directly collected signals and respectively reconstructed signals. Numerical simulations were performed using 3 databases from Physionet. Accuracies of the algorithms were calculated using 10-fold cross validation for each database.

Numerical studies in this work demonstrate that existing algorithms work well on records of high signal quality and without severe distortions, but the performance is less satisfactory on records with noises and arrhythmias. Challenges can occur due to artifacts and arrhythmias. For carefully chosen records, correlation-based features and wave-based features can both produce promising results. For example, the database based on Physionet Challenge 2011 was purposefully constructed so that only clean signals were included. For this database, the best model produces excellent accuracies (>=0.984) for all misplacements except the LA/LL interchange (0.874); see Table **5**-**6**. However, the accuracies are significantly lower for records with noises and arrhythmias; see Table **5**-**4** and Table **5**-**5**. Our empirical studies also suggest that combining the features from Kors and Herpen and those from Heden et al. may yield more robust and accurate results.

It appears that algorithms developed using one database may not work well for other databases. For example, although the results in [145] are impressive, their method produces poor results when applied to the three databases used in this article; see model 1 in Table **5**-**4**, Table **5**-**5** and Table **5**-**6**. We have also conducted cross-database validation using the three databases here; see Table **5**-**7** to Table **5**-**10**). For the worst scenario, the best accuracies for different types of misplacements range from 0.361 to 0.784. The poor performance in cross-database validation may be due to several reasons. First, the training database and the test database may be significantly different. Second, the model may not be sufficiently complex to account for variances in

the data. Moreover, over-fitting may occur. These problems can be overcome by extending the database, increasing the complexity of the model, and adopting more advanced training methods.

We have assumed that when an electrode is placed on the leg, it is placed at the standard place, i.e. the ankle. In clinical practice, especially for exercise and ambulatory ECG, "leg" electrodes may be placed near the torso according to the Mason-Likar convention. ECGs collected in the Mason-Likar system may be essentially different from the standard ECGs. Algorithms developed using standard ECGs shall be examined and probably modified before they are applied to ECGs collected using the Mason-Likar method. Most importantly, while the potential difference between the two ankles is almost zero, the potential difference may be substantially larger at other places on the legs. Therefore, in the Mason-Likar system, misplacement involving the RL electrode may not be as easily identified as in the standard ECGs. Moreover, the equivalence between layouts shown in Table 5-1 is no longer true.

A recent report from American Heart Association recommends, "Lead-switch detection algorithms should be incorporated into digital ECGs … and suspected misplacements should be identified … in time to correct the problem. If not corrected before recording, a diagnostic statement … should be incorporated into preliminary interpretive reports" [184]. However, the existing techniques cannot be directly applied in clinical settings. More careful studies need to be conducted. Machine learning techniques combined with signal enhancement techniques and more accurate estimation of ECG waves may improve the detection accuracy. Computer algorithms shall also be tested on independent data sets in a blind manner to ensure robust results.

## 5.5 Automatic detection of ECG electrode misplacement under clinical settings

### 5.5.1 Objective

In Section 5.4, we studied the distinction between a certain type of misplacement and the correct ECG once at a time. In other words, the whole detection system will include multiple two-class steps, each of which is designed to detect one specific type of misplacement. However, in practical applications, the type of electrode misplacement in an ECG is not known a priori. Therefore, it is not clear how accurate the algorithms are in practice.

Moreover, we tested the performances of the algorithms using test data sets that contain the same number of correct and misplaced ECGs, which was also how existing publications performed for tests. Recall that misplacements occur in 4% of all ECGs in reality. Thus, performance evaluation based on balanced data sets may be misleading. This section aims to develop automatic misplacement detection algorithms to overcome these challenges.

### 5.5.2 Algorithm overview

Figure **5**-**6** shows the flowchart of the overall algorithm. During the preprocessing stage, artifacts will be removed from the ECG and then the ECG is delineated to detect the heartbeats. The preprocessing techniques we used have been introduced in section 5.4.2.The preprocessed ECG will be evaluated using two sequential steps. The first step determines whether the ECG has been correctly collected. Once electrode misplacement is determined, the second step will examine the ECG to determine what the type of misplacement is. Still two types of features are used. The first type is the physiology based features as explained in section 5.4.3 and the second is the correlation based features introduced in section 5.4.4.

### 5.5.3 Design of classifiers

As shown in Figure **5**-**6**, Step 1 is a two-class classification problem to determine whether the ECG was collected with misplaced electrodes and, if misplacement is detected, Step 2 is a five-class classification problem to determine the type of misplacement. We adopted neural network models for classification in both steps and implemented these models using the artificial neural network toolbox in Matlab [181]. Both network models have two hidden layers, where the first hidden layer has five neurons and the second layer has six neurons. The hyperbolic tangent sigmoid transfer function was used in each layer. The Levenberg-Marquard algorithm [185] was adopted as the training function for both steps, whose cost functions are both defined as the mean-squared error. The model in step 1 has one output node, whose output varies between 0 and 1. We took 0.5 as the discrimination threshold. Therefore, the output of a correct ECG is expected to be less than 0.5 and the output of a misplaced ECG is expected to be otherwise. The model in Step 2 has five output nodes, each of which, varying between 0 and 1, represents the probability for the occurrence of one type of misplacement. Note that the sum of all five outputs in Step 2 equals to 1.

One may naturally ask what if steps 1 and 2 were combined into a single step that consists of 6 output nodes, corresponding to the correct ECG and one of each misplacement type. This idea had been investigated. However, the results were less satisfactory than the use of the two separate steps.

Nonlinear neural networks may have multiple local minima. When training a network, the Matlab toolbox starts from a set of random parameters and the result may converge to one of the local minima [186]. This randomness leads to variations in the classification outcomes. To overcome that problem, we adopted a "voting" strategy [187]. For each classification problem, we trained 20 different neural net classifiers, each of which started from random initial guesses and used the same set of training data. Then, the outputs from the 20 neural net classifiers were averaged to generate the final output. Empirical studies showed that voting can reduce variations and improve the overall performance.

69
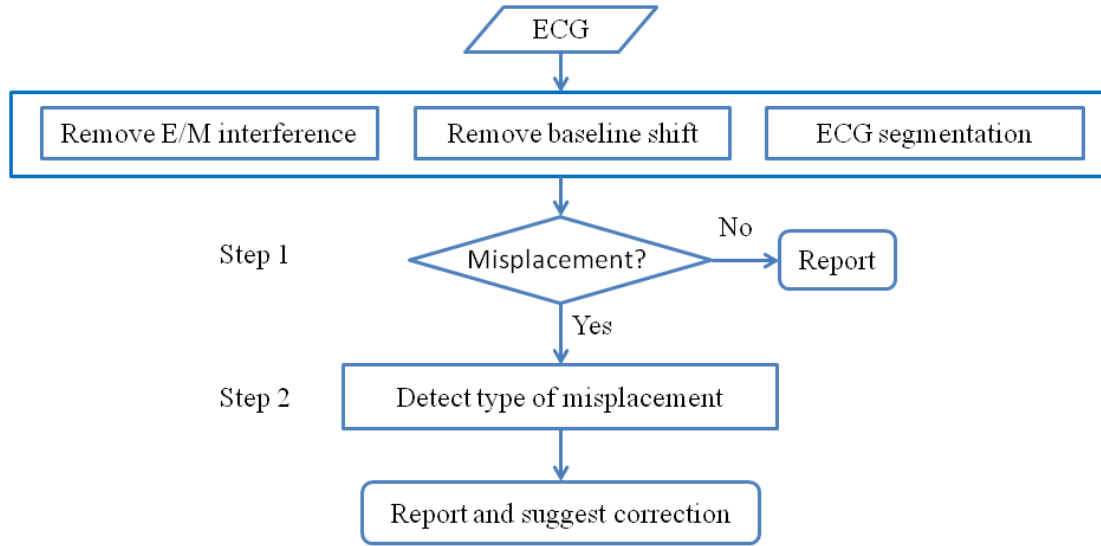
Figure 5-6. Flowchart of the algorithm for automatic ECG electrode misplacement detection. Step 1 is a two-class classification problem and Step 2 is a multi-class classification problem.

### 5.5.4 Performance evaluation

Table **5-11** shows a confusion table [188] for the two-class classification in Step 1. The following metrics are often used for two-class classification:

$$\text{sensitivity} = \frac{\text{TP}}{\text{TP+FN}}, \quad \text{specificity} = \frac{\text{TN}}{\text{TN+FP}}, \quad \text{accuracy} = \frac{\text{TP+TN}}{\text{TP+FP+TN+FN}}.$$

Sensitivity [189], also known as recall, describes how accurately the step can recognize misplaced records. Specificity [190] describes how accurately the step can recognize correct ECGs. Accuracy describes the overall accuracy of the step. Two additional metrics are also useful:

$$\text{PPV} = \frac{\text{TP}}{\text{TP+FP}}, \text{NPV} = \frac{\text{TN}}{\text{TN+FN}},$$

where PPV stands for positive predictive value and NPV stands for negative predictive value. Positive predictive value [191], also known as precision, is the portion of positive predictions that are true positives. A poor (low) precision indicates a high false alarm rate. Negative predictive value [191] is the portion of negative predictions that are true negatives.

Table 5-11. Confusion matrix for classification results

| | | Actual Class | |
| --- | --- | --- | --- |
| | | Positive (Misplaced ECG) | Negative (Correct ECG) |
| Predicted Class | Positive (Misplaced ECG) | True Positive (TP) | False Positive (FP) |
| | Negative (Correct ECG) | False Negative (FN) | True Negative (TN) |

A poor (low) NPV indicates a high false negative rate. For a test set that includes equal number of positive and negative records, it is sufficient to report sensitivity and specificity since high sensitivity and specificity infer to high PPV and NPV. However, for a highly unbalanced test set, PPV and/or NPV should also be reported. Recall that no more than 4% of all ECGs are collected with electrode misplacements in clinical settings [55]. In later section, we will show the importance of PPV and NPV for such an unbalanced classification problem,

Step 2 has multiple outputs. We evaluated the performance using the accuracy for each output.

### 5.5.5 Resampling for discrimination step 1

When studying step 1, resampling was conducted on the test and training sets to better evaluate the classification performances and to improve the performances; see Table 5-12. For the original test and training sets, the ratio between positive (misplaced) and negative (correct) records is 5:1 because five types of electrode misplacements were considered.

Resampling on the test set was to emulate the frequency of misplaced records in clinical settings. We included all negative records from the original test set and randomly selected a number of positive records so that the ratio between positive and negative records is 1:24. To gain statistical significance, the resampling was repeated 100 times and results were averaged average performances were reported.

Table 5-12. The ratio between positive and negative records (P:N) in original data sets and resampled data sets. A resampled test set includes all the negative records in the original test set whereas 1/120th positive records in the original test set are randomly selected to include in a resampled test set. The negative records in the original training set is repeated 8 times to form a resampled training set, which also include randomly selected 1/5th of the positive records from the original training set.

| Data set | Original set | Resampled set |
|---|---|---|
| Test set | P:N = 5:1 | P:N = 1:24 |
| Training set | P:N = 5:1 | P:N = 1:9 |

Resampling on the training set was to improve the overall discrimination performance. We randomly selected 1/5 positive records in the original training set and repeated each negative record 8 times so that the ratio between positive and negative records is 1:9.

### 5.5.6 Results for Step 1: determining whether an ECG record has been correctly collected

Table 5-13 shows the results of step 1 using the original training set. First, the classifiers were evaluated on the original test set. Physiological features yielded excellent scores for all metrics whereas the performance of correlation features was less satisfactory. Combining physiological and correlation features yielded better performance than each individual feature set. Then, the same classifiers were evaluated on the resampled test set. Comparing the results of the two test sets yields interesting observations. The two test sets have the same specificity value for each feature set since they include the same negative records; see Table 5-12. The positive records in the resampled set were randomly selected from the original test set; therefore, the two test sets have almost identical sensitivity values for each feature set. However, PPV on the resampled test set is much worse than that on the original test set for each feature set. This can be understood by comparing the definitions of specificity and PPV. The numbers of FP records are the same for the two test sets. However, the number of TP records in the resampled test set is about 1/24th of that in the original test set, indicating PPV in the resampled test set is much worse than the specificity set. Following a similar argument, one can see that NPV in the resampled set should be better than the sensitivity value. The poor PPV values in the resampled test set implies that classifiers trained in this way will have high false positive rates in clinical settings, where the percentage of positive records is no more than 4%.

Table 5-13. Performance of step 1 using the original training set (P:N=5:1). Results on the resampled set were based on averaging of 100 resampling trials. See Table 3 for descriptions of the data sets.

| Test Set | Features | Accuracy (%) | Sensitivity (%) | Specificity (%) | PPV (%) | NPV (%) |
|---|---|---|---|---|---|---|
| Original (P:N = 5:1) | Physiological | 97.7±0.0 | 99.6±0.0 | 87.9±0.0 | 97.6±0.0 | 97.9±0.0 |
| | Correlation | 89.5±0.0 | 98.7±0.0 | 43.5±0.0 | 89.7±0.0 | 87.3±0.0 |
| | Combined | 98.5±0.0 | 99.7±0.0 | 92.7±0.0 | 98.6±0.0 | 98.2±0.0 |
| Resampled (P:N=1:24) | Physiological | 88.4±0.0 | 99.6±0.1 | 87.9±0.0 | 25.6±0.0 | 100.0±0.0 |
| | Correlation | 45.7±0.0 | 98.9±0.5 | 43.5±0.0 | 6.8±0.0 | 99.9±0.0 |
| | Combined | 93.0±0.0 | 99.6±0.3 | 92.7±0.0 | 36.4±0.1 | 100.0±0.0 |

Motivated by results in Table 5-13, we resampled the training set to reduce the P:N ratio. Due to limitations in computer memory and efficiency, we chose P:N to be 1:9; see Table 5-12 for detailed descriptions. Results using the resampled training set are shown in Table 5-14. Although the NPVs of the original test set are not satisfactory, the performances of all metrics on the resampled set are outstanding, especially using combined features. We re-emphasize that the resampled test set was designed to mimic the ratio of positive records in clinical settings.

### 5.5.7 Results for Step 2: determining the type of misplacement

Once a record was recognized as misplacement, we then applied step 2 to determine the type of misplacement. In step 2, both the training and test sets include equal number of records for each type of misplacement. Results using different features are shown in Table 5-15. Ten-fold cross validation was performed. Average performance with standard deviation is shown here. The best overall performance was obtained using combination of physiological and non-physiological features.

### 5.5.8 Java software

The computer algorithms were implemented into software using Java. A graphical user interface was developed using the Java Swing (Figure **5**-**7**).

### 5.5.9 Summary

We have developed an algorithm that includes two discrimination steps for automatic detection of limb cable reversals in ECG. We used resampling to achieve more reliable evaluations and to improve the overall performance of the algorithm. Resampling the test set is necessary to reveal potential false positive predictions in practical applications. Resampling the training set yields optimal outcomes in all performance metrics.

73

Step 1 of the algorithm determines whether an ECG was correctly collected and Step 2 determines what the misplacement type is. Combing the two steps can warn the ECG operator about potential misplacement and can give suggestions about how to correct the error. The performance of Step 1 is 99.6% accuracy, 91.7% sensitivity, 99.9% specificity, 98.9% positive predictive value and 99.7% negative predictive value. The overall accuracy of Step 2 is 90.4%.

Future work should investigate misplacements involving both limb and precordial electrodes. Since the 10 electrodes produce millions of possible layouts of misplacement, a crucial step will be to determine a feasible set of electrodes that are most likely to be misplaced and the outcomes of their misplacements can seriously interfere subsequent diagnoses by physicians or by computers.

Table 5-14. Performance of Step 1 using the resampled training set (P:N=1:9). See Table 3 for descriptions of the data sets.

| Test Set | Features | Accuracy (%) | Sensitivity (%) | Specificity (%) | PPV (%) | NPV (%) |
|---|---|---|---|---|---|---|
| Original (P:N=5:1) | Physiological | 84.3±0.0 | 81.2±0.0 | 99.9±0.0 | 100.0±0.0 | 51.5±0.0 |
| | Correlation | 67.3±0.0 | 60.8±0.0 | 99.7±0.0 | 99.9±0.0 | 33.7±0.0 |
| | Combined | 93.1±0.0 | 91.7±0.0 | 99.9±0.0 | 100.0±0.0 | 70.6±0.0 |
| Resampled (P:N=1:24) | Physiological | 99.1±0.1 | 80.5±1.3 | 99.9±0.0 | 96.7±0.1 | 99.2±0.1 |
| | Correlation | 98.2±0.1 | 61.2±3.3 | 99.7±0.0 | 89.3±0.5 | 98.4±0.1 |
| | Combined | 99.6±0.0 | 91.7±0.8 | 99.9±0.0 | 98.9±0.0 | 99.7±0.0 |

Table 5-15: Performance of Step 2 based on 10 fold cross validation.

| Placement | Physiological features (%) | Correlation features (%) | Combination (%) |
|---|---|---|---|
| LA/RA | 88.6±0.8 | 76.5±2.4 | 91.2±0.6 |
| RA/LL | 85.5±1.0 | 65.5±3.6 | 88.7±1.2 |
| LA/LL | 90.9±0.9 | 79.4±1.6 | 94.7±0.5 |
| RA>LA>LL>RA | 85.4±1.0 | 59.7±1.9 | 86.9±1.1 |
| RA>LL>LA>RA | 86.7±1.0 | 55.4±3.1 | 90.3±0.7 |
| Overall Accuracy | 87.4±0.3 | 67.3±0.3 | 90.4±0.2 |
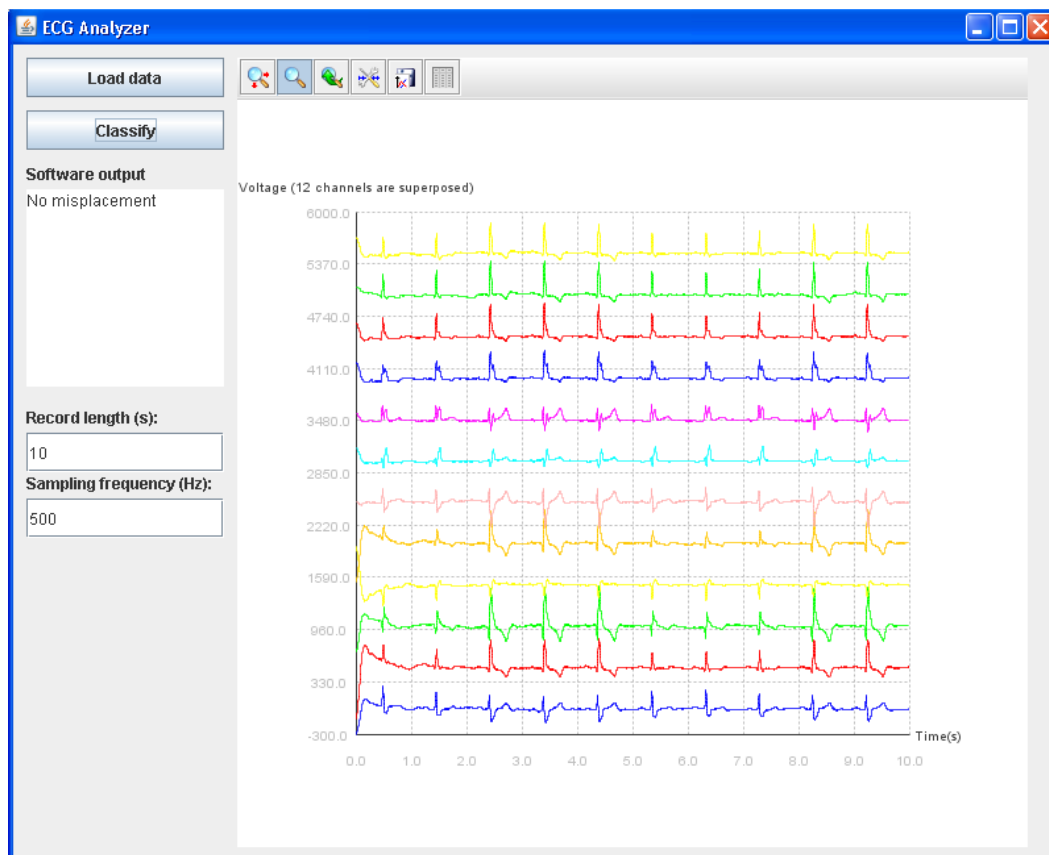
Figure 5-7: Java software for automatic electrode misplacement detection

# CHAPTER 6
# EVALUATION OF ECG QUALITY

## 6.1 Overview

In Chapter 5, an algorithm for automatic detection of electrode misplacement during ECG collection was developed and evaluated. However, ECG signals are also susceptible to many other kinds of artifacts, such as physiological artifacts caused by muscular activities or patient motion, non-physiological artifacts caused by electromagnetic interference and so on. Those artifacts may lead to wrong diagnosis and thus mistreatment. It is of great clinical challenge and significance to differentiating ECG artifacts from patterns of diseases.

In this chapter, a computational framework, called matrix of regularity, will be proposed to evaluate the quality of ECGs. The matrix of regularity is a novel mechanism to fuse results from multiple tests of signal quality. Moreover, this method can produce a continuous grade, which can more accurately represent the quality of an ECG. When tested on a data set from Computing in Cardiology/Physionet Challenge 2011 (the training data set a), the algorithm achieves up to 95% of accuracy. The area under the receiver operating characteristic curve is 0.97. The developed framework and computer program have the potential to improve the quality of ECGs collected using conventional and portable devices.

Moreover, we will also present a method based on image processing in this chapter. Various image patterns are used as features to distinguish between low- and high-quality signals. When tested on a data set from the Physionet Challenge 2011 (the training data set a), the analyses yield up to 94.36% accuracy. This method provides an interesting alternative for ECG quality evaluation. This technique will have particular use for ECGs scanned from paper recordings.

In the last section of this chapter, we will present a web system developed by us for ECG monitoring and analysis. Recent advances in mobile technology and cloud computing have inspired numerous designs of cloud-based health care services and devices. Within the cloud system, medical data could be collected and transmitted automatically to medical professionals from anywhere and feedbacks could be returned to the patients through the network. In this work, we developed a cloud-based system with clients for mobile devices or web browsers. Specially, we attempted to address the issues regarding the usefulness of the ECG data collected from patients themselves. Algorithms for ECG enhancement, ECG quality evaluation and ECG parameters extraction were implemented in the system. The system was demonstrated by a use case, in which ECG data was uploaded to the web server from a mobile phone at a certain frequency and

analysis was performed in real time in the server. The system has been proven to be functional, accurate and efficient.

## 6.2 Data

The Computing in Cardiology/Physionet Challenge 2011 [142] calls for improving the quality of ECGs by developing computer algorithms to detect errors and artifacts in ECGs. The Challenge ECGs are sampled at 500 Hz with 16-bit resolution. The records have a minimum length of 10 seconds. These records were recorded by nurses, technicians, and volunteers with varying amounts of training to generate a collection of recordings of different qualities. The ECGs were annotated in blinded fashion by a group of reviewers with varying amounts of expertise in ECG analysis. Each ECG was reviewed by as few as 3 annotators and as many as 18 annotators. When examining an ECG, the reviewer assigned it a letter grade according to its quality: A (0.95) for excellent, B (0.85) for good, C (0.75) for adequate, D (0.60) for poor or F (0) for unacceptable. Then, the ECG was assigned to one of the 3 groups according to the averaged grade. The acceptable group includes all ECGs whose average grade is not less than 0.7 and has at most one F grade. The indeterminate group includes all ECGs whose average grade is not less than 0.7 but has two or more F grades. The unacceptable group includes all ECGs whose average grade is less than 0.70.

The Challenge ECGs were divided into 3 data sets: sets A, B, and C. Data in set A are for training of the algorithms and the reference quality assessments were provided to the participants. Reference quality assessments for data sets B and C were withheld for 3 Challenge events. Results in this work are obtained using data in set A.

## 6.3 Matrix of Regularity (MoRE)

### 6.3.1 Overview

A variety of signal quality indices have been explored by various authors. A few authors have explored methods to assess ECG qualities. Quantitative measurements like the number of times the ECG exceeds a preset limit (out-of-range events, ±4 mV) and the frequency content of the ECG in low frequency band (0.05–0.25 Hz) were proven to be useful for evaluating signal quality [83]. Alfaouri and Daqrouq (2008) [192] proposed two techniques, the piecewise method and the analytical approach, to determine the percent difference, the signal-noise-ratio and the compression ratio in evaluating the quality of ECG signals. Redmond et al. (2008) [193] developed algorithms to detect four types of artifacts: rail contact, high frequency noise, low power mask, and sudden baseline shift. Clifford and associates [194]-[195] developed various signal quality indices (SQIs) to evaluate the quality of ECGs and to robustly estimate heart rate from multiple asynchronous noisy sources.

Several authors have obtained excellent results in classification of ECG qualities using machine learning techniques [196]-[198]. An alternative, probably more intuitive, approach is to develop rule-based algorithms, which have also yielded comparable classification results [199][200]. Immediately, the most straightforward algorithm can be designed by serially examining an ECG record against a number of different tests, see Figure **6**-**1**. Here, one can run an ECG through a sequence of tests, and regard a record as acceptable if it passes all the tests or unacceptable if it fails any test. This approach has limitations. First, since the output of the algorithm is a yes-no type of classification, it does not accurately reflect the quality of an ECG. For example, it is not possible to distinguish between an ECG of perfect quality and one that barely passes all tests. Moreover, some records may pass all tests individually but they shall be labeled as unacceptable when multiple tests are considered simultaneously. Therefore, the main objective of this work is to develop a framework that can generate a graded score for ECGs by simultaneous consideration of multiple tests. The integration of multiple tests is known as data fusion in signal classification. There are many different ways for signal fusion.

Here, we propose a framework, called matrix of regularity; see the schematic representation in Figure **6**-**2**. The algorithm includes a preprocessing operation, which consists of multiple, optional processes. Then, the processed ECG undergoes a number of different tests, the results of which are systematically organized into a matrix, which represents the regularity of the record. Finally, a "score" can be computed as a measurement of the matrix of regularity to represent the quality of the ECG.

### 6.3.2 Preprocessing
As shown in Figure **6**-**2**, the preprocessing includes three steps. The first and second steps are respectively to remove baseline shift and electromagnetic interference which is typically manifested by high frequency noise from the signals. The algorithm for performing these tasks has been introduced in section 5.4.2. The third step of the preprocessing is ECG signal segmentation. This is also introduced earlier in section 5.4.3. For concision, they are not introduced again in this chapter.
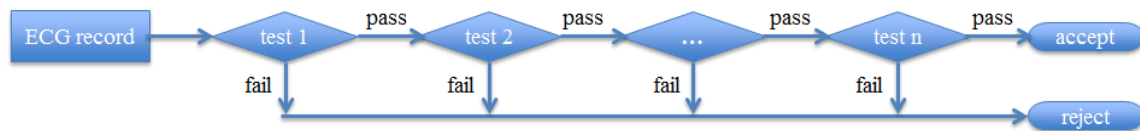
Figure 6-1. Schematic of a serial framework for ECG quality evaluation
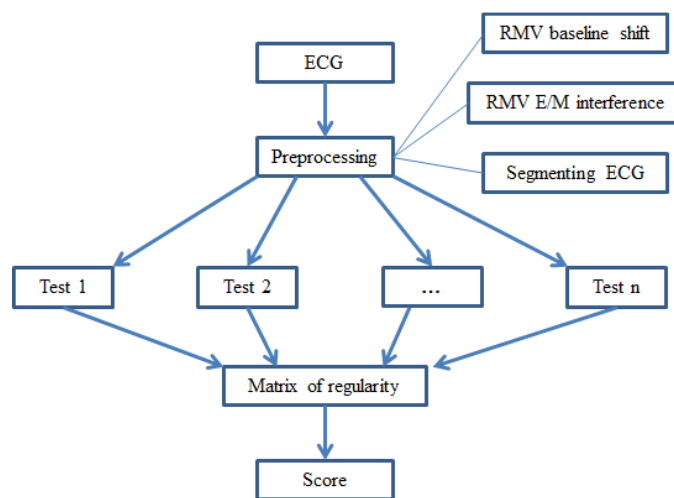


Figure 6-2. A parallel framework for evaluation of ECG quality. Here, RMV represents "remove."

### *6.3.3 Matrix of regularity*

To evaluate the quality of an ECG, we introduce a matrix of regularity (MoRE), denoted by R, to measure the degree of irregularities (artifacts) in the ECG. R is a 12x12 matrix, where each column corresponds to one lead of the ECG. For a given column and its corresponding lead, the diagonal element represents the influences of irregularities in the corresponding lead to itself and the other elements represent the influences of irregularities in the other leads to the present lead. For example, the element (1,1) represents influences to the quality of lead I due to artifacts in lead I whereas the element (2,1) represents influences to the quality of lead I due to artifacts in lead II. For an ECG of perfect quality, R is a zero matrix since there is no irregularity. When the degree of artifacts induced irregularities increases, the matrix R will become further "away" from the zero matrix. In the following, we illustrate the construction of the matrix of regularity using examples of a few tests. We note that the matrix of regularity is an open framework, which can be easily extended by including other signal indices [196]-[200]. We also note that one can skip the filtering in preprocessing and incorporate influences of powerline noises and baseline shift into the matrix of regularity.

*Missing Signals*

When a segment of a lead is a flatline or off the ECG chart, we say that segment of signal is "missing." A flatline lead is the hallmark of improper connection of electrodes or electrode placement errors [194][201]. Hoffman reported a case of bilateral arm-to-leg electrode interchange, where the arm leads are switched with the foot leads [202]. This misplacement leads to inversions of P and T waves in leads II, III, and aVF. Moreover, such a bilateral lead switch causes a flatline lead I. An off-chart lead may be caused by large patient motion or saturation of the acquisition amplifier [193].

We describe how to represent missing signals in the matrix of regularity. First, we discuss the off-chart scenario. Denote by p the percentage that the signals of a lead are off the chart. To represent this irregularity in the matrix of regularity, the value p is added to the diagonal element of matrix R corresponding to the lead. When a lead is missing, not only the reviewer does not know the behavior of this lead but it also affects the reviewer's capability to examine this lead's correlation to all remaining leads. To account for this interference, when a percentage p of a lead is missing, we assume it influences the regularity of all other lead in the amount of p/11. For example, if a percentage p of lead I is missing, we add p to the element (1,1) and p/11 to all the other elements in the first row. The flatline scenario is handled in a slightly different fashion. We first divide the 10-second signal of a lead into 10 segments of 1 second. If the range of a segment is less than a prescribed threshold value, that segment is regarded as a flatline. The percentage of the flatline segments is computed and the matrix of regularity is correspondingly updated.

*Overlaps between Leads*

In an ECG chart, the 12 leads are laid out properly so that a normal ECG will have no significant overlaps between leads. Artifacts and diseases may cause large amplitude signals in one or more leads. These large amplitude signals manifest as irregular overlaps between leads, which makes the ECG hard to interpret. Through empirical observation on the training data, we find the overlaps due to artifacts are more severe and irregular than those due to diseases. Here, we consider algorithms to detect overlaps between leads due to artifacts. An example of lead overlaps is shown in Figure 6-3. Here, overlaps caused by artifacts in lead V1 make parts of other leads hard to view. For purpose of demonstration, we calculate the frequency of overlap to lead I, denoted by p, and add p to the element (7,1) of the regularity matrix. When lead V1 overlaps with other leads, it affects the normal visibility of V1 itself. Therefore, the influence of overlap to V1 is the summation of overlaps with all other channels.

*Irregular Beats*

One of the signal quality indices proposed by Li et al. (2008) [195] is to evaluate the beat quality of an ECG lead using power spectral density. Specifically, this quality index is defined as the spectral distribution ratio (SDR), which is the ratio of the spectral power of the lead signal between the frequencies of 5 Hz and 14 Hz to that between the frequencies of 5 Hz and 50 Hz. Li et al. showed that low SDR values are likely to correspond to muscle artifacts and high SDR values are often due to QRS-like artifacts caused by electrode motion. They suggested that an intermediate range of SDR (0.5<=SDR<=0.8) indicates good ECG quality. The quality index SDR can be incorporated into the matrix of regularity. For example, we define $\rho = \max(0.5 - SDR, SDR - 0.8, 0)$. Then, it follows that $\rho = 0$ when 0.5<=SDR<=0.8 and $\rho > 0$ otherwise. A positive value of $\rho$ indicates artifacts in the channel. To account for the influences of such artifacts, one can introduce $\rho$ to the corresponding diagonal and off-diagonal positions. Properly weights may be introduced to account for the relevant significance compared to other signal quality measurements.
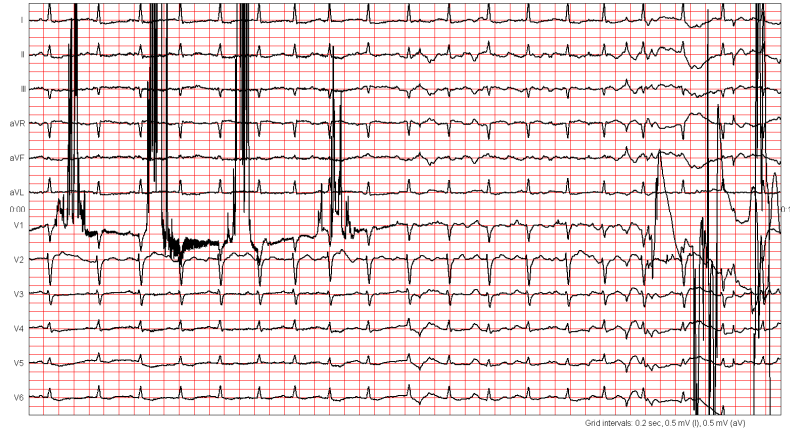
Figure 6-3. An example ECG, where artifacts in lead V1 cause overlaps with other leads.

### 6.3.4 Grading the ECG

We compute properties of the matrix of regularity as scores to grade the quality of the ECG. This can be done in several ways. For example, the summation of all elements in the matrix represents overall influences to the whole ECG chart combining all the tests. The column summation represents the channel that is subject to most severe disturbances. Another interesting score is the spectral radius of the matrix of regularity, which is the largest magnitude of all eigenvalues. Note that these scores are nonnegative real numbers. Since a score is a continuous number, it allows ECG qualities be divided into different levels, yielding more accurate representation of ECG quality than "yes-no" type of classification. Note that the score of the ECG computed from the regularity matrix can be regarded as a natural fusion of grades from the individual tests. By way of design, a zero score corresponds to perfect signal quality and increased scores correspond to decreased ECG quality.

### 6.3.5 Results: numerical accuracy and Android software

*Numerical accuracy*

We apply the developed algorithm to the Physionet Challenge training set (set A). This set includes 1000 records. All records were reviewed by volunteer annotators following the process described in Section 6.2. Based on the annotation, 773 records were assigned to the acceptable group, 225 records were assigned to the unacceptable group, and 2 records were assigned to the indeterminate group. To verify the accuracy of the developed algorithm, we exclude the 2 indeterminate records.

Matrices from individual metrics are multiplied by different weighting coefficients and then summed together to form an overall matrix of regularity. First, we form a matrix using all metrics discussed in the method section. Then,

intensive parameter studies are carried out to select an optimal set of parameters that produces the best classification results. When comparing matrices formed with and without the preprocessing steps, we find that, for the Challenge dataset, matrices without the preprocessing step generally produce better results than their counterparts with preprocessing. Therefore, numerical results in Figure **6**-**4** are obtained without the filtering process. Nevertheless, filtering may be a useful option for other datasets and applications.

To represent the numerical results, we compute a score for each record as the spectral radius of the matrix of regularity. Then, a threshold of the score is selected to classify the records into acceptable and unacceptable categories. Recall that the regularity matrix is conceived to be a zero matrix for perfect ECGs and artifacts are represented as disturbances to the matrix. Therefore, larger scores represent lower quality levels. We mark the records with scores less than the prescribed threshold as acceptable and those with scores greater than the threshold as unacceptable. Three common quantities are commonly used to measure classification performance. Accuracy is the overall probability of correct prediction, sensitivity is the probability that an unacceptable record is correctly classified as unacceptable, and specificity is the probability that an acceptable record is correctly classified as acceptable. Figure **6**-**4** (left panel) shows the dependence of accuracy, sensitivity, and specificity on the score threshold. As the threshold increases, the sensitivity increases whereas the specificity decreases. The best accuracy is 0.951, at which sensitivity=0.884 and specificity=0.970; see red circle in Figure **6**-**4**. The right panel of Figure **6**-**4** shows a receiver operating characteristic (ROC) curve (Fawcett 2006), which is a plot of the true positive rate (sensitivity) versus the false positive rate (1-specificity) under variation of the discrimination threshold. The perfect classification, corresponding to 100% sensitivity and 100% specificity, is represented by the upper left corner in the receiver operating characteristics space. Classification methods based on random guess would lie along the dashed diagonal line in ROC. Thus, the diagonal line is also referred to as the no-discrimination line. ROC can be used to represent the accuracy of a test. For example, the area under the ROC curve, also known as area under curve (AUC), has been widely used for model comparison. An area of 1 represents a perfect test and an area of 0.5 represents a worthless test. The AUC for the algorithm developed here is 0.97, indicating excellent diagnostic accuracy.
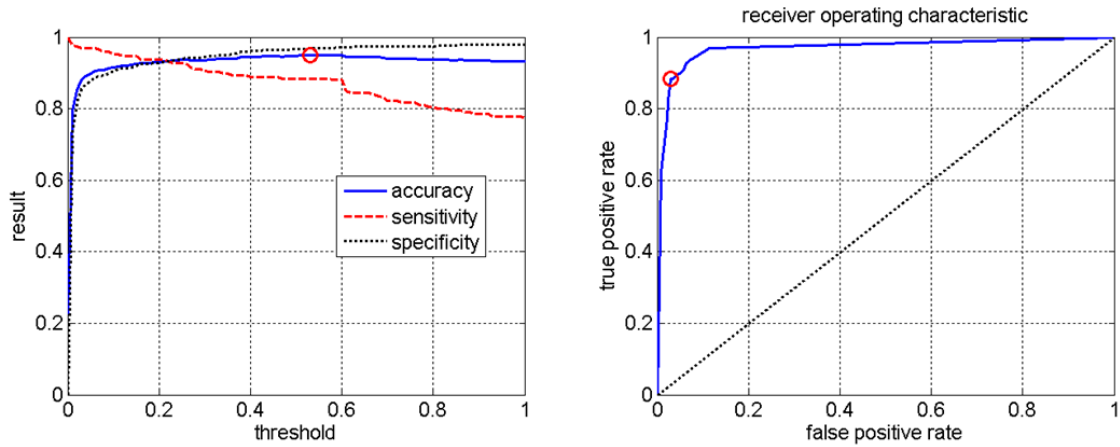
Figure 6-4. Classification result: dependence of accuracy on the threshold (left) and receiver operating characteristic curve (right). The best classification result is represented by a red circle in both panels.

*Android software*

The Android is a software stack for mobile devices that includes an operating system, middleware and key applications, belonging to the Google Inc. As part of a Challenge, a Java program has been developed on an Android emulator and tested on an Android phone.

Developing programs for a phone is different from developing desktop applications, web sites, or back-end server processes. Especially, CPU speed and memory are usually limited in mobile phones. In order to reduce computational time, we adopt a simplified version of the matrix of irregularity. Here, we neglect the preprocessing operations and incorporate only the missing signal test in the regularity matrix. Using this simplified model, the best classification accuracy is 0.929 and the corresponding sensitivity and specificity are 0.809 and 0.964, respectively. Note that the comprehensive model and the simplified model yield similar prediction accuracies. This is probably because the training data set is limited and not all artifacts are well represented.

When tested on an Android simulator (Eclipse Helios Service Release 2 with Android 2.3.3) on a computer with 2 cores (2.40GHz and 2.39GHz) and 3.62G of Ram, on average, it takes 1.918 seconds to load an ECG record of 10 seconds and it takes 0.16 seconds to form the regularity matrix and compute the grade.

### 6.3.6 Summary

We have developed a novel data fusion framework, called matrix of regularity (MoRE), to assess the quality of ECGs. We have used a few example

tests to demonstrate how test results can be incorporated into MoRE. The algorithm proves to be accurate and robust using ECG records from the Computing in Cardiology/Physionet Challenge 2011 [142]. Artifacts in ECGs may cause wrong diagnosis. A computer algorithm that can improve the quality of ECGs may have significant clinical relevance. Such algorithms can also be implemented in portable ECG devices to improve the quality of health care for those who do not have easy access to regular, high-quality clinics.

Compared to a conventional multi-step test algorithm, the algorithm developed here provides integrative consideration of multiple quality tests. The results can be regarded a natural fusion of multiple tests. Moreover, the algorithm generates continuous grades, which allows more accurate representation of the quality of an ECG. This algorithm can be combined with ROC analysis to help choose the optimal model for ECG evaluation. A user can choose different thresholds for different purposes. It is little or no additional cost to retake an ECG when the patient is at site. The cost of error for false positive is low. Thus, a practical algorithm may choose to have higher sensitivity to guarantee the quality of collected ECGs.

It is interesting to note that matrices are often used to represent network graph and vice versa [203]-[204]. Here, we speculate the representation of the matrix of regularity using a network graph. For example, we use an open circle to represent a lead of good quality and arrange the 12 circles in a clockwise direction so that the circle representing lead I is at the position of 1 o'clock and that representing lead V6 is at the position of 12 o'clock; see Figure 6-5 (left panel). To represent a nonzero value at one diagonal position of MoRE, we can darken the face of the corresponding circle to a level proportional to the diagonal value in the matrix. Off diagonal elements of MoRE can be represented by drawing lines between the corresponding circles. For example, the right panel of Figure 6-5 shows a graph representing an ECG, where leads V5 and V6 are missing. Black circles at 11 o'clock and 12 o'clock represent the two missing leads. A line is drawn from each of the missing leads to all the other leads to represent the reduced correlation due to loss of that lead. The simple example here suggests a potential connection between ECG quality and graph theory.

The size of the data set used in this study is limited and not all types of artifacts are well represented. Since the Physionet ECGs were annotated by a group of volunteer reviewers with a wide range of expertise in ECG, the reference classifications show inconsistency and large variances. More careful annotations on these data may be necessary for future research to further improve the algorithms for physiological signal quality evaluation. Annotating is a subjective process. We believe consistent references rely on a systematic method of annotating. A consensus in rules has to be achieved beforehand to reduce variances between reviewers and records. It will also be interesting to

study the cross correlations between the classifications by different groups of annotators, as indicated by statistics in [142].



Figure 6-5. Graphical representation of evaluation based on matrix of regularity. The left corresponds to an ECG of perfect quality. The right represents an ECG where leads V5 and V6 are missing.

# 6.4 Image based ECG quality evaluation

### 6.4.1 Overview

In this section, we will present an ECG quality evaluation method based on image processing. We first use simple rules to find out obviously poor signals. Then we convert the remaining records to images and extract features from the images. Finally we use machine learning techniques for feature selection and classification.

### 6.4.2 Extraction of ECG Image Features

We convert the digital record of a 12-lead ECG into a binary image and extract five groups of various image features to represent its quality. First, we notice large amplitude baseline wandering, motion artifact, noises, and large range of lead variation may cause readings of neighboring leads to become interwoven. Such interwoven patterns can be characterized by the number of connected components [205]. A connected component is a subgraph in which any two vertices are connected to each other by paths. Figure **6**-**6** shows an example of a graph with two connected components.
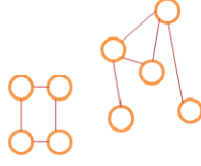
Figure 6-6. A graph with two connected components.

Another feature commonly used for image quality is the texture descriptor [206] that characterizes image textures or regions. They are descriptions of the visual features of the contents, such as the shape, the color, and the texture. The third feature is from the covariance analysis [207] of the vector population derived from the image representation of the ECG recording. First, the image is represented by an Nx2 matrix, where each row represents the x and y coordinates of a black pixel, and N is the number of pixels. Then, the covariance matrix is computed for the Nx2 matrix. Finally eigenvalues and eigenvectors of the covariance matrix are used as features of the image.

By observing the good vs. bad quality ECG images, we see that the good quality image present many small spikes while the bad quality ones do not. This feature promotes the frequency-domain analysis. We perform Fourier transformation on the image and extract features from frequency domain. The Fourier transformation on an image is represented as [206] Equation 6.1, in which, x and y are spatial coordinates, L(x,y) being the distribution of brightness on the spatial space, and $f_x$ and $f_y$ are spatial frequencies in the horizontal and vertical directions.

$$F\left(f_x, f_y\right) = \int_{-\infty}^{\infty} \int_{-\infty}^{\infty} L(x, y) e^{-j2\pi(f_x x + f_y y)} dx\, dy \qquad (6.1)$$

The last group of features we consider is from the wavelet analysis of the image [206], which provides time-frequency analysis of the ECG image. It is extremely useful when the image is non-stationary, i.e., the frequency component does not exist across the spatial domain of the entire image that different frequency components appear at different locations of the image. Wavelet analysis is a multi-resolution technique. For each scale we obtain three groups of wavelet coefficients for high frequency components and one group of wavelet coefficients for low frequency components. A wavelet is a wave-like oscillation which has non-zero values only in a small range. Wavelets usually have specific properties that make them useful for extracting information from unknown non-stationary signals. The continuous wavelet transformation of a 2d signal f(x,y) using a mother wavelet $\Phi$(x,y) is defined as Equation 6.2 where s is positive and defines the scale, and a and b are any real number and they define the shift [208].

$$\text{cwt}(s, a, b) = \frac{1}{\sqrt{s}} \iint f(x, y) \, \Phi \left( \frac{x-a}{s}, \frac{y-b}{s} \right) dxdy \qquad (6.2)$$

Following the ideas introduced above, five feature groups have been obtained. They are explained one by one as following.

**Feature group 1**: It is observed that over 93% of the good ECG records have less than 20 connected components (left of Figure **6**-**7**), while over half of the bad ECG records have many more than 20 connected components (right of Figure **6**-**7**). Also, the maximum and minimum areas of the connected components for good and bad records are pretty well separated.

**Feature group 2**: Six image features are computed to describe the image textures: average gray level, average contrast, smoothness, third-order moment, measure of uniformity, and entropy. Take the average gray level as an example, over 98% of the good ECG records have an average gray level of 240~250 (left of Figure **6**-**8**), while only 67% of the bad ECG records have an average gray level in that range (right of Figure **6**-**8**).

**Feature group 3**: The covariance analysis yields another group of features. The eigenvalues of vector population for good and bad records show obvious difference. Figure **6**-**9** shows that, the largest eigenvalue is more evenly distributed for bad records.

**Feature group 4**: After performing Fourier transformation on images, we first compute the proportion of the components which have zero frequency in horizontal directions as shown in Equation 6.3 where $(f_x = 0, f_y)$ represents the frequency components of which the frequencies in horizontal directions are zero, and $\text{sum}(F(f_x = -50 : 50, f_x \neq 0, f_y))$ is the sum of the frequency components where the frequencies in horizontal directions are nonzero and are in the range of -50:50.

$$F(f_x = 0, f_y) / \text{sum}(F(f_x = -50 : 50, f_x \neq 0, f_y)) \qquad (6.3)$$

For each image, we will obtain a vector, and then we use the mean and standard deviation of the vector as features. Figure **6**-**10** shows a plot of these features, with blue representing acceptable records and red indicating unacceptable records.

**Feature group 5**: Figure 6-11 shows the 2-level 2-dimensional fast wavelet transform of an acceptable record (left) and an unacceptable record (right). Both images are decomposed by passing through high and low pass filters in a cascading way. The high and low pass filters are generated from the

Daubechies 4 wavelet. Define the coefficient decomposition vector as C = [ a h(n) v(n) d(n) h(n-1) ... v(1) d(1) ], where a, h, v, and d are column vectors containing approximation, horizontal, vertical, and diagonal coefficient matrices, respectively and n is the decomposition level. We have utilized the mean and the standard deviation of a, h(i),v(i) and d(i), with $1 \leq i \leq n$, as features.
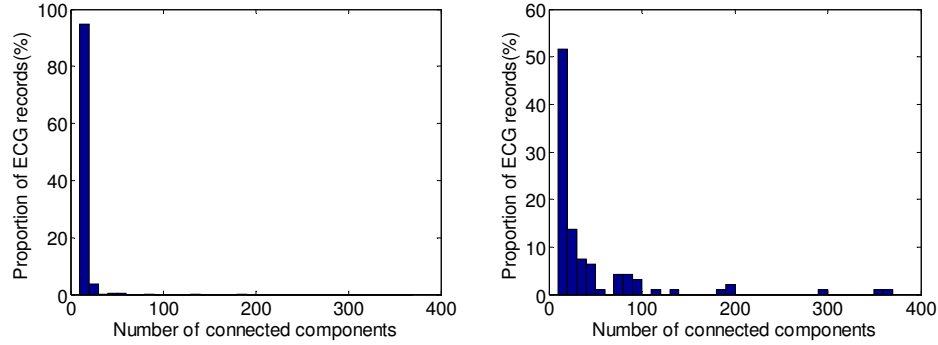


Figure 6-7. Number of connected components for good records (left) and poor records (right)
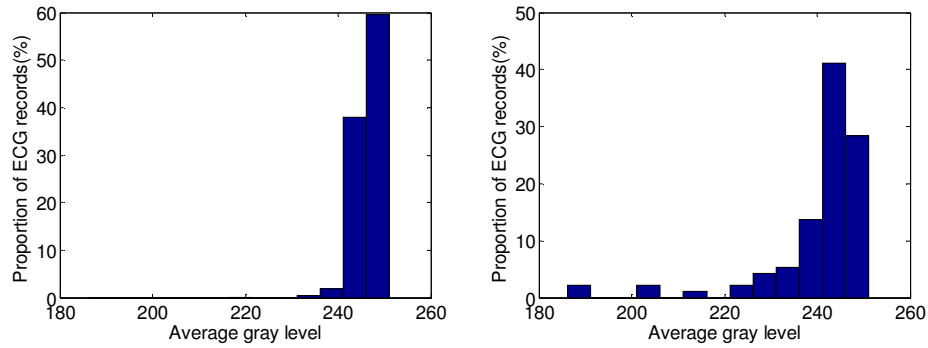


Figure 6-8. Average gray level for good records (left) and poor records (right)
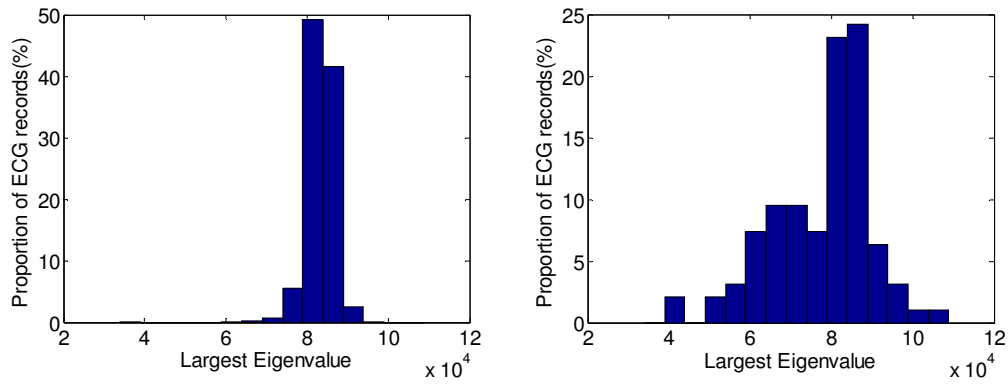
Figure 6-9. Largest eigenvalue of vector population for good records (left) and poor records (right)
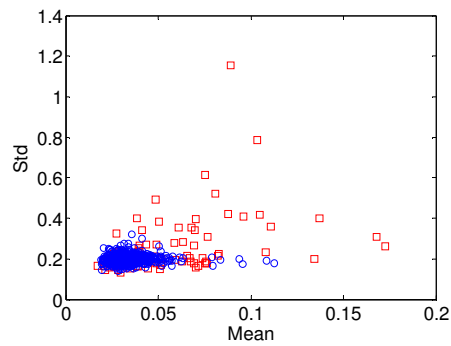


Figure 6-10. Features from frequency space. Blue symbols represent good records and red indicate bad ones
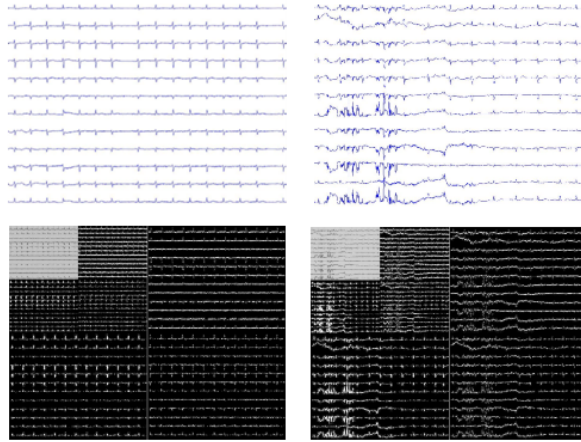
Figure 6-11. An example of the 2D wavelet transform of a good-record image (left) and a bad-record image (right). Each original image is high-pass filtered horizontally, vertically and diagonally and it generates the three large detail images, and then each is low-pass filtered generating an approximate image. The approximation image is further high and low-pass filtered to produce the three smaller detail images and the final approximation image in the upper-left

### 6.4.3 Feature selection and feature fusion methods

The principal component analysis [209] is a widely used technique in exploratory data analysis and making predictive model. It can expose the internal structure of a data set. If an object has N aspects, very possibly some of the aspects are correlated. So it is not necessary to observe the object from all the N aspects, but only from a few of the most "principal" aspects. The PCA uses orthogonal transformation to convert a set of observations which might be correlated to a set of uncorrelated observations. In this procedure, the dimension is reduced. Thus, it is a reliable and convenient technique for feature selection. During the procedure of the PCA, the first principal component has as high a variance as possible. Succeeding components are orthogonal and thus uncorrelated to the preceding component and they also have the highest variances.

Another widely used technique for feature selection is the independent component analysis (ICA). The ICA separates a signal into subcomponents which are non-Guassian [210] and statistically independent. During the analysis, independent components are estimated to maximize the statistical independence. The independence can be defined in many ways. Most often they are defined as the minimization of mutual information (MMI) or the maximization of non-Gaussianity. The MMI is typically quantified by measures like Kullback-Leibler Divergence [211] and maximum-entropy [212], and the Non-Gaussianity is often computed by measures like kurtosis [213] and negentropy [214]. Another technique we use is the adaptive boosting algorithm for feature fusion. The adaptive boosting algorithm aims to compose a "committee of

experts" of multiple algorithms, called classifiers, such that the committee's result is better than a single vote from each individual classifier. In our work, each group of features yields a classifier.

For demonstration, denote an ECG record by $x_i$ and denote the prediction of this record from the $j^{th}$ classifier by $k_j(x_i)$. We introduce the convention that an ECG of acceptable quality is assigned a value +1 and an ECG of unacceptable quality is assigned a value -1. A committee will be formed using linear combination of the n classifiers as Equation 6.4 where $\alpha_i$ is the weight assigned to the prediction of each classifier. The result of the committee is determined by the sign of $C(x_i)$.

$$C(x_i) = \alpha_1 k_1(x_i) + \alpha_2 k_2(x_i) + \cdots \alpha_n k_n(x_i) \qquad (6.4)$$

A cost will be defined for each prediction $k_j(x_i)$. If the prediction is incorrect, a heavier cost is charged; otherwise, a light cost is charged. The total cost is the sum of the costs for all test records from all algorithms. The goal is therefore to choose the optimal weighting coefficients to minimize the total cost. This can be solved using any optimization method. In general, an iterative process is preferred since it is easy to expand the committee to include new classifiers.

### 6.4.4 Classification Process
A flowchart of the classification process is shown in Figure **6**-**12**.To improve the computational efficiency, an ECG with at least one flatline channel is labeled as unacceptable. Likewise, an ECG with at least one lead that is off the chart is labeled as unacceptable. Then, we extract various image features of an ECG. Finally, the obtained features are classified using a support vector machine [215].
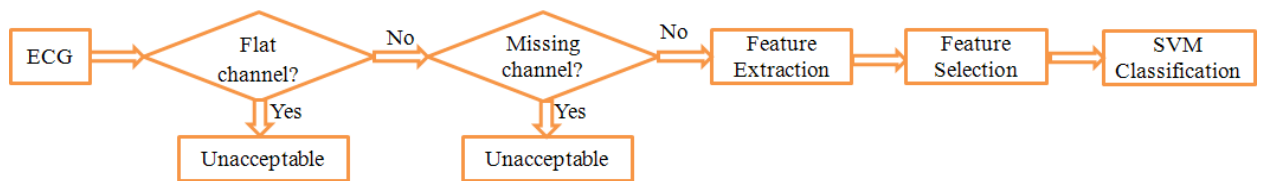


Figure 6-12. A flowchart of the classification process

A support vector machine [216] is a supervised learning method that analyzes data and recognizes patterns, used for classification and regression analysis. In a space, a support vector machine constructs a hyperplane that has the largest distance to the nearest training data points of any class so that different classes can be best separated to minimize the generalization error of the classifier. We conduct support vector machine analysis using the SVM toolbox in Matlab [181]. We apply a non-linear support vector machine, using the Gaussian radial basis function [217] as the kernel function.

### 6.4.5 Classification accuracy

We first carry out classification analysis using one group of features at a time. The classification accuracy is evaluated using a randomized 10-fold cross-validation. Table **6**-**1** shows the classification accuracy for each group of features.

Furthermore, features are selected using the techniques of principal component analysis, independent component analysis and the adaptive boosting respectively. Table **6**-**2** shows the classification accuracies after feature selection with the PCA. Different numbers of principal components (PC) are used as features, and it is observed that using 5 principal components yields the best accuracy of 92.5%. Table **6**-**3** shows the results using independent component analysis for feature selection. The best accuracy of 93.4% is obtained when 8 components are used.

Finally, we used the adaptive boosting for feature fusion. With randomized 10-fold cross-validation, we obtained an accuracy of 93.60%, with sensitivity as 78.11% and specificity as 98.31%. This is the best accuracy we've got so far.

### 6.4.6 Summary

We have explored various image processing techniques to evaluate the quality of an ECG record. Different kinds of features from images are extracted and the support vector machine is used for classification. Feature selection and feature fusion techniques are explored to improve the performance. The best two accuracies are 93.6% and 93.4%. The former was obtained using the adaptive boosting algorithm and the latter was obtained after feature selection using the independent component analysis.

For many years, researchers have strived to make the medical diagnosis process automated. To make the automation reliable and efficient, computer-implemented algorithms should emulate how human beings make diagnosis. Clinically, heart doctors need to inspect different leads simultaneously to make diagnosis. Processing the ECG as an image provides a natural way of interpreting the ECG readings simultaneously and may help retrieve global information from the 12-lead ECG.A promising idea is to combine the two

techniques, 1-dimensional ECG signal processing and 2-dimensional ECG image processing, simultaneously on ECG data to study the CVD.

Table 6-1. Classification accuracy for each group of features. Accuracy is based on 10-fold cross-validation.

| Feature group | Dimension | Accuracy | Sensitivity | Specificity |
|---|---|---|---|---|
| Connected component | 4 | 0.9330 | 0.7854 | 0.9778 |
| Texture descriptor | 6 | 0.9200 | 0.6996 | 0.9870 |
| Covariance analysis | 3 | 0.9250 | 0.7639 | 0.9739 |
| Spectral Analysis | 4 | 0.9220 | 0.7082 | 0.9870 |
| Wavelet analysis | 14 | 0.9230 | 0.6953 | 0.9922 |

Table 6-2. Classification accuracy after feature selection with PCA. Accuracy is based on 10-fold cross-validation.

| Number of PC | Accuracy | Sensitivity | Specificity |
|---|---|---|---|
| 1 | 0.9190 | 0.6910 | 0.9883 |
| 2 | 0.9210 | 0.6953 | 0.9896 |
| 3 | 0.9160 | 0.6910 | 0.9844 |
| 4 | 0.9180 | 0.6953 | 0.9857 |
| 5 | 0.9250 | 0.7253 | 0.9857 |
| 6 | 0.9080 | 0.6438 | 0.9883 |
| 7 | 0.9030 | 0.6094 | 0.9922 |
| 8 | 0.9050 | 0.6009 | 0.9974 |

Note: PC represents principal components

Table 6-3. Classification accuracy after feature selection with ICA. Accuracy is based on 10-fold cross-validation

| Number of IC | Accuracy | Sensitivity | Specificity |
|---|---|---|---|
| 1 | 0.9200 | 0.6695 | 0.9961 |
| 2 | 0.9230 | 0.7167 | 0.9857 |
| 3 | 0.9210 | 0.7253 | 0.9804 |
| 4 | 0.9190 | 0.7468 | 0.9713 |
| 5 | 0.9240 | 0.7382 | 0.9804 |
| 6 | 0.9240 | 0.7468 | 0.9778 |
| 7 | 0.9270 | 0.7768 | 0.9726 |
| 8 | 0.9340 | 0.7940 | 0.9765 |
| 9 | 0.9230 | 0.7167 | 0.9857 |

Note: IC represents independent components

# 6.5 Cloud ECG

### 6.5.1 Overview

In chapter 5, an algorithm for detecting electrode misplacement automatically was presented. In previous sections of this chapter, we presented an algorithm for automatic ECG quality evaluation. Next, we will introduce a web system for ECG monitoring and analysis. Algorithms for ECG enhancement, ECG quality evaluation and ECG parameters extraction were implemented in the system. Within the cloud system, medical data could be collected and transmitted automatically to medical professionals from anywhere and feedbacks could be returned to the patients through the network.

### 6.5.2 Cloud-Software Design

Figure **6**-**13** shows the schematic overview of the cloud system. The system is designed to be accessible from anywhere using any device, such as a smart phone, a tablet, a desktop or a laptop. The final applications were deployed on a server in the Amazon cloud using the Amazon web service and the Amazon related database service. It has both a doctor console and a patient console.

Figure 6-14 shows a schematic representation of the cloud environment's architecture. The web application was developed under a framework called "Spring", which is said to be "the most popular application development framework for enterprise Java™" [218]. Techniques of HTML [219], jquery [220], AJAX and java server pages [221] were used. The Tomcat server [222] was used to contain the application. The web application was designed in the architecture of "model-view-controller" [223]. The final application was deployed and tested on the Amazon cloud using the Amazon web service and the Amazon related database service. The transmission of data between the client and the server is through the protocol of the Hypertext Transfer Protocol Secure (HTTPS) [224] to ensure security. The core functions of the system include ECG enhancement, ECG visualization, ECG quality evaluation, ECG measurements and ECG data management.
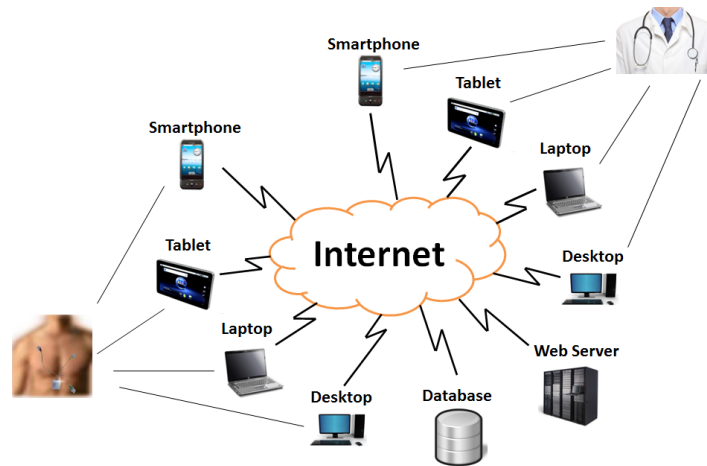
Figure 6-13. Schematic cloud environment
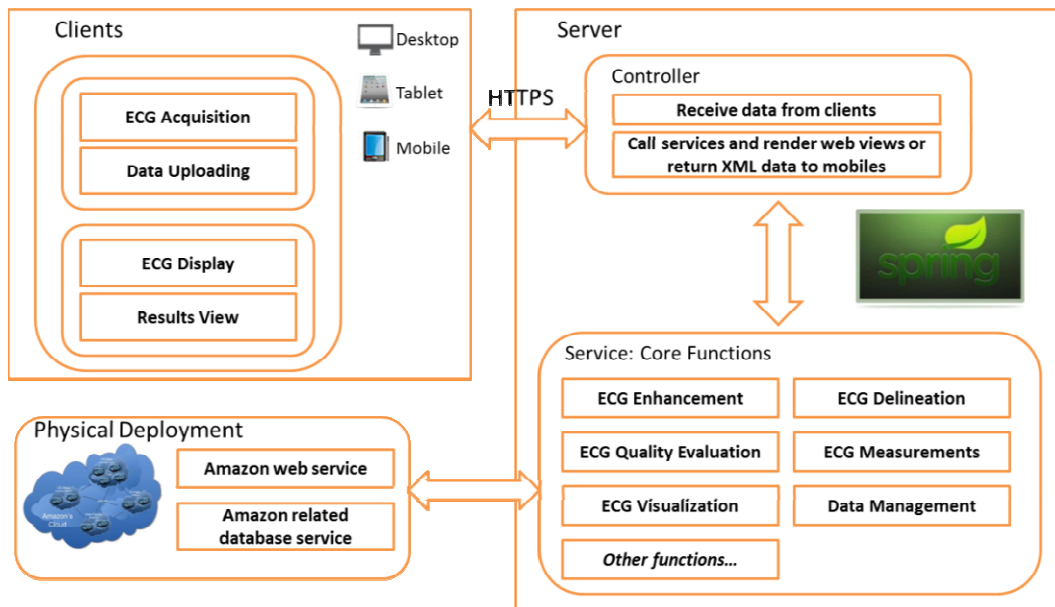


Figure 6-14. Schematic architecture of the cloud environment.

The overall functionality of the system includes:

1. *ECG signals are collected using wearable ECG devices or other devices. If using a wearable ECG device, the data can be transmitted to a mobile phone through Bluetooth automatically.*
2. *The users can get access to the cloud system through a mobile client or a desktop/web client. The ECG record is uploaded from the client to the web server.*
3. *Overall quality of an ECG record is evaluated by the system. Types of artifacts and potential electrode misplacement will be identified and reported.*
4. *ECG records can be viewed online.*
5. *Critical parameters like the heart beat rate and RR interval are estimated*
6. *A patient can browse his or her previous ECG records.*
7. *A patient can submit selected ECGs to a health professional for diagnosis.*
8. *A doctor can have access to records of the users that have registered with him/her.*
9. *A doctor can make tentative decision about a patient and ask for a second opinion from a colleague wile withholding the patient's personal information.*
10. *Once a final decision is made by a doctor, the related patient will immediately have access to the results.*
11. *A doctor can also upload reference ECGs (open-source) to be accessed by patients, fellow physicians, or scientists for purpose of education and research.*

A preliminary design of the patient console is shown in Figure **6**-**15**. The doctor console (not shown) has a similar interface. Figure **6**-**16** shows a preliminary design of the "History" panel.

Figure **6**-**17** shows an interface for the mobile client. It was developed with Java in Android. A user can set the frequency for uploading. In our test, ECG records were uploaded to the web server every 10 seconds. The WIFI was used for internet access. After ECG records were uploaded to the server, they were analyzed in real time. In this test, we used the WIFI for internet access, and it normally took less than 1 second for each uploading. Note that, for demonstration purpose, we saved 12-channel ECG records, each of which was about 118KB containing 10-second ECG signals, in the cell phone in advance. In future work, we will use wearable ECG devices to collect signals and the signals will then be transmitted to mobile phones via Bluetooth.
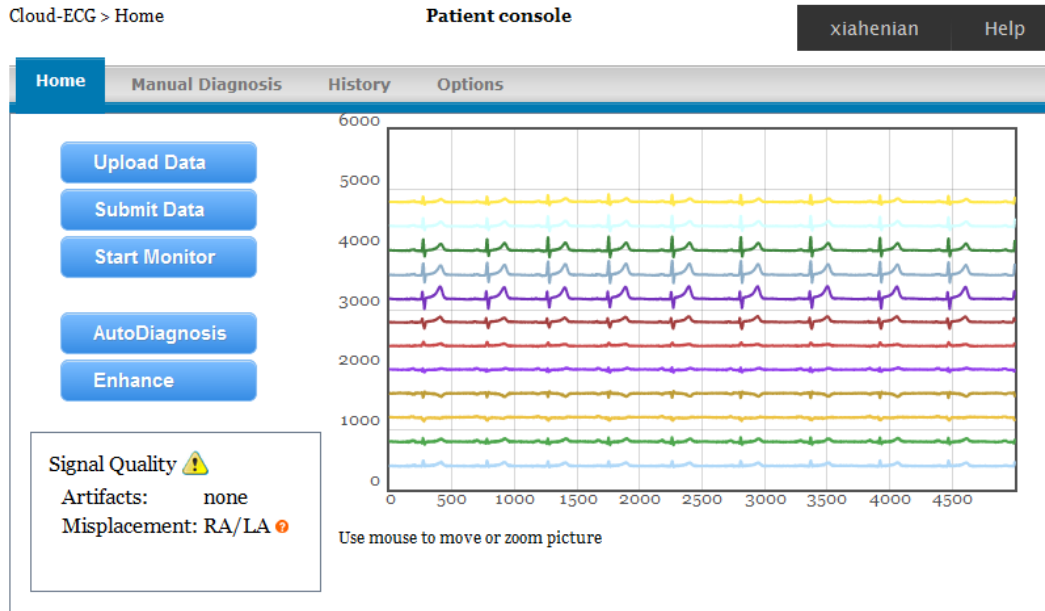
**Patient console**

xiahenian    Help

Home    Manual Diagnosis    History    Options

Upload Data

Submit Data

Start Monitor

AutoDiagnosis

Enhance

Signal Quality ⚠
Artifacts:        none
Misplacement: RA/LA ❷

Use mouse to move or zoom picture

Cloud-ECG © 2012, Nonlinear BioDynamics Laboratory at University of Tennessee, Knoxville

Figure 6-15. A preliminary design of the patient console of the cloud-ECG software. A doctor console has a similar interface.

Cloud-ECG > Home

**Patient console**

xiahenian    Help

Home    Manual Diagnosis    History    Options

| Upload time | Quality grade | Artifacts | Misplacements |
|---|---|---|---|
| 2012/01/20 12:49:53 | -8 | None | None |
| 2012/01/20 12:46:57 | -8 | None | None |
| 2012/01/18 18:02:50 | -9 | None | None |
| 2012/01/18 18:01:27 | -8 | None | None |
| 2012/01/18 17:52:50 | -8 | None | None |
| 2012/01/18 17:23:58 | 10 | None | None |
| 2012/01/18 17:21:03 | -8 | None | None |
| 2012/01/18 15:54:46 | -8 | None | None |
| 2012/01/18 15:54:15 | -8 | None | None |
| 2012/01/18 15:53:35 | -8 | None | None |

1  2  3

Cloud-ECG © 2012, Nonlinear BioDynamics Laboratory at University of Tennessee, Knoxville

Figure 6-16. A preliminary design of the "History" panel

98
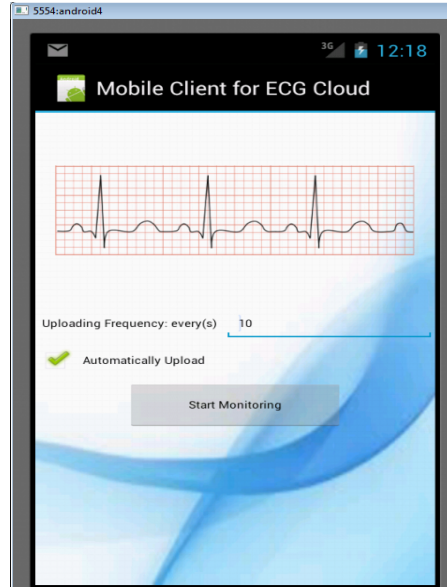
Figure 6-17. Mobile client for the cloud system

### 6.5.3 Summary

In this work, we have presented a cloud-based system for real-time ECG monitoring and analysis. We have attempted to address the issues regarding the usefulness of the ECG data collected from patients themselves. Algorithms for ECG enhancement, ECG quality evaluation and ECG parameters extraction were implemented in the system. The system was demonstrated by a use case, in which ECG data was uploaded to the web server from a mobile phone at a certain frequency and signal analysis was performed in real time after the signal was uploaded to the server. The system has been proven to be functional, accurate and efficient in monitoring and analyzing the ECG data.

# CHAPTER 7
# ICU MORTALITY PREDICTION USING ARTIFICIAL NEURAL NETWORKS

## 7.1 Overview

In this chapter, an algorithm based on artificial neural network was developed for prediction of in-hospital mortality in ICU. Two hundred and five features were extracted from thirty-five time-series physiological variables. They were ranked according to their respective performance in ten ten-fold cross validation tests and the worst thirty-eight features were abandoned. An effective and efficient greedy algorithm for feature selection was developed to select the best feature subset from the remaining one hundred and sixty-seven features. The final chosen feature subset contained forty-seven features. When applying to a data set with 4000 ICU records, an accuracy of $(86.23\pm0.14)\%$, a sensitivity of $(50.29\pm0.22)\%$, a specificity of $(92.01\pm0.21)\%$, a positive prediction value of $(50.29\pm0.50)\%$, a negative prediction value of $(92.01\pm0.00)\%$, and a Lemeshow score of $119.55\pm9.87$ were obtained. The results were based on five 10-fold cross validation tests. To overcome the local minima frequently encountered during neural network training, 100 classifiers were trained each time and their outputs were averaged for final forecasting. A much better Lemeshow score was achieved when using 100 best classifiers out of 3000. An accuracy of $(86.17\pm0.00)\%$, a sensitivity of $(49.75\pm0.59)\%$, a specificity of $(92.03\pm0.15)\%$, a positive prediction value of $(50.07\pm0.24)\%$, a negative prediction value of $(91.93\pm0.00)\%$, and a Lemeshow score of $41.3981\pm3.41$ were obtained using the latter approach. An optimization approach was used to calibrate the predictive probabilities and it improved the Lemeshow score to $27.51\pm4.38$.

## 7.2 Data

The Physionet Challenge 2012 [225] provides 12000 records. Each of them was from an ICU stay. The 12000 records were divided into three data sets A, B and C, each containing 4000 records. Set A was the training data set. Both the data of measurement and the observed outcome of each record in Set A were available for every participant of the challenge. The Set B was for validation, and its data was available to participants too, but the outcome was not open. The Set C was used for final evaluation of each participant's algorithm and neither the data nor the outcome was available. Algorithms in this work were mostly trained and evaluated using the Set A. Evaluations were based on repeated 10-fold cross validation to ensure reliability.

The records were collected from four types of ICUs: coronary care unit, cardiac surgery recovery unit, medical ICU and surgical ICU. All the ICU stays lasted for at least 48 hours. Four static variables were collected on admission. They are "Age (years)", "Gender (0: female, or 1: male)", "Height (cm)", and "ICU type". Thirty-seven time series variables were collected once, more than once, or

not at all in each record. For example, in Set A, the variable HR (heart rate) is collected in 97% of the 4000 records, while the variable Lactate is only collected in 55% of the 4000 records. In Figure 7-1, the number of occurrence of each of the thirty-seven time-series variables in records of the Set A were displayed. This information is important because variables should be avoided if they are very rarely measured. Note that, variables TropI (Troponin-I) and TropT (Troponin-T) were never measured in any record of Set A. So there were thirty-five time series variables in fact.

## 7.3 Method

### 7.3.1 Imputation

Up to 41 different types of variables are available, including 37 time series variables and 4 static variables. Among them, some were very rarely collected and all variables were not collected in every ICU stay. For classification, the feature space must be consistent for every record. For example, if the maximum value of the heart rate is extracted as a feature from one record, that should be extracted from all other records too. Consequently, it is necessary to handle the missing data properly. In this work, the missing data was handled using an imputation method based on gender. For a given variable, its medians were calculated for all females and all males respectively. Suppose the median of a variable is $v1$ in all females and $v2$ in all males. Then a missing variable of that type is imputed as $v1$ if it's a female record or $v2$ if it's a male record. If the gender is unknown for a record, the imputation was calculated as $c1*v1+c2*v2$, where $c1$ and $c2$ are the frequencies of female and male patients in the set respectively. The reason for imputing missing values in this way is the significant difference observed between female and male patients. For example, the median of the variable Cholesterol in female records is 158.5mg/dL, but is 146mg/dL in male records.
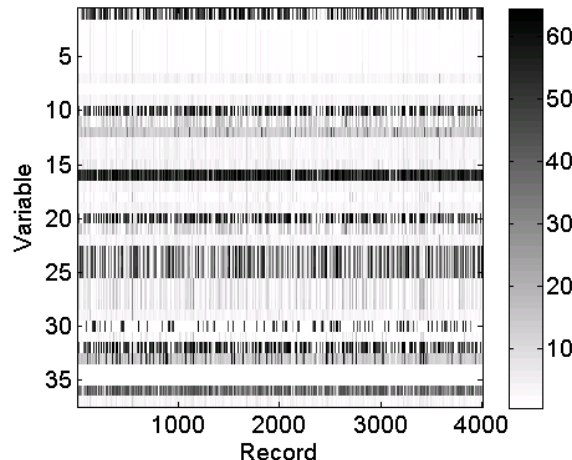


Figure 7-1. Number of occurrence of each variable in Set A's 4000 records. Thirty-seven time series variables are presented here.

### 7.3.2 Performance evaluation

Table 7-1 shows a confusion matrix [188]. The following metrics are often used for two-class classification:

$$\text{sensitivity} = \frac{\text{TP}}{\text{TP+FN}}, \quad \text{specificity} = \frac{\text{TN}}{\text{TN+FP}}, \quad \text{accuracy} = \frac{\text{TP+TN}}{\text{TP+FP+TN+FN}}.$$

Sensitivity [189], also known as recall, describes how accurately the mortality can be predicted. Specificity [190] describes how accurately the algorithm can recognize the survivor. Accuracy describes the overall accuracy. Two additional metrics are also useful:

$$\text{PPV} = \frac{\text{TP}}{\text{TP+FP}}, \text{NPV} = \frac{\text{TN}}{\text{TN+FN}},$$

where PPV stands for positive predictive value and NPV stands for negative predictive value. Positive predictive value [191], also known as precision, is the portion of positive predictions that are true positives. A poor (low) precision indicates a high false alarm rate. Negative predictive value [191] is the portion of negative predictions that are true negatives. A poor (low) NPV indicates a high false negative rate. For a test set that includes equal number of positive and negative records, it is sufficient to report sensitivity and specificity since high sensitivity and specificity infer to high PPV and NPV. However, for a highly unbalanced test set, PPV and/or NPV should also be reported.

Table 7-1: Confusion matrix for classification results.

| | | Observation | |
|---|---|---|---|
| | | Died in-hospital (Positive) | Survivor (Negative) |
| Prediction | Died in-hospital (Positive) | True Positive (TP) | False Positive (FP) |
| | Survivor (Negative) | False Negative (FN) | True Negative (TN) |

Another metric commonly used is the Hosmer-Lemeshow statistic [227]. A lower Hosmer-Lemeshow score represents a better goodness-of-fit. It assesses whether real event rates match predicted event rates. The calculation of the Hosmer-Lemeshow score follows the method below [225]:

1. Sort mortality risks predicted;

2. Bin corresponding records into deciles designated by g=1,2,3,…10, so that decile g=1 contains records with lowest predicted risk, while decile g=10 contains records with highest predicted risk

3. Compute the score by

$$H = \sum_{g=1}^{10} \frac{(O_g - E_g)^2}{N_g \pi_g (1 - \pi_g) + 0.001}$$

where for each decile g, $O_g$ is the real number of deaths, $E_g$ is the predicted number of deaths, $N_g$ is the number of records, and $\pi_g$ is the mean estimated risk for records in the decile.

In the Computing in Cardiology/Physionet Challenge 2012 "Predicting Mortality of ICU Patients" [225], two performance evaluation metrics were defined, respectively for challenge event 1 and challenge event 2. The event 1 score is defined as the minimum of the sensitivity and the positive predictive value. The event 2 score is defined to be the Lemeshow score. They measure an algorithm from two aspects and they will be used throughout this paper.

### 7.3.3 Features

*Feature definitions*

Thirty-five time series variables were available. Structured features should be extracted from them. Typical time series signal analysis techniques include Fourier analysis methods [228], wavelet analysis methods [229], autoregressive (AR) model [230], etc. But none of those approaches fits our problem because all the variables were too sparsely sampled and none of them was sampled at a constant rate. Thus six statistical features were computed for each variable, which were the minimum, maximum, average, standard deviation, estimated trend, and the last measurement. The meanings for all the statistics are obvious except the estimated trend. The estimated trend measures how the variable changes over time in general. In each record, a linear regression model is fitted for all measurements of a variable and the slope of the fitted line is estimated as the trend of that variable. For example, Figure 7-2 shows the estimation of the trend for heart rate in a record.

The six statistics were not computed for all time-series variables. Inspired by the physiological importance, the sum of the urine measurements over forty-eight hours is considered as one feature, and the above six statistics were not computed for the urine variable. Our studies also showed that the static variables

didn't help the prediction. Thus they are not included in the features. A total of 205 features were computed consequently.

*Feature ranking*

Among the 205 features, it was suspected that some of them would not help the prediction and useless features may even work as noise and impair the ability of classification of the model. Thus each single feature was applied independently first to see how they would perform. To overcome the local minima problem frequently encountered during neural network training, 100 classifiers were trained each time and their outputs were averaged for final forecasting. The 205 features were then be ranked according to their average performances in ten 10-fold cross validation tests. The event 1 score which is the minimum of the sensitivity and PPV were used as the criterion for ranking.

*Feature selection*

After feature ranking, 38 features with the worst event 1 scores were abandoned and 167 features remained. We guaranteed that all 35 time series variables were present except the variable "MechVent". MechVent is the mechanical ventilation respiration. It has two values 0 and 1, respectively for false and true. It was found to be 1 for almost every record and thus was not helpful. To find the optimal subset among the 167 features, a greedy algorithm was proposed. Figure 7-3 shows the detailed algorithm.
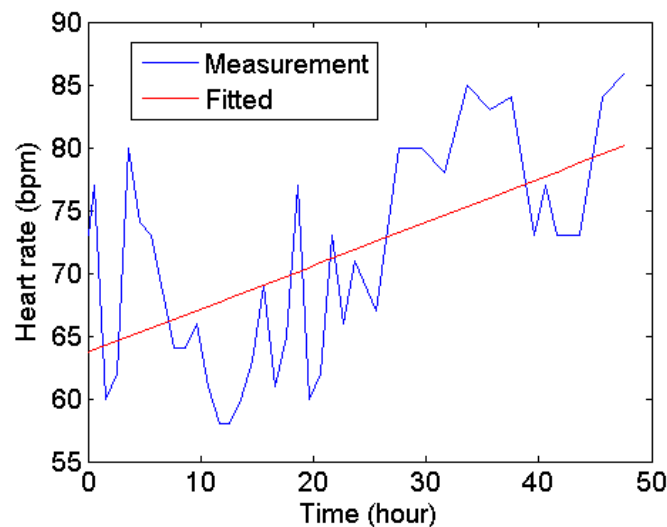


Figure 7-2: Trend estimation: the measurements were fitted to a linear line, and the slope of the line was used for the trend estimation

The idea is to add one feature in each round. Let's denote the set of unselected features as USF and the set of selected features as SF. Before feature selection, SF is empty and USF contains all features. In each round, every feature in USF is added to SF successively, forming a number of subsets. For example, 167 subsets were formed in the first round, 166 subsets in the second round, and so on. One hundred classifiers are trained for each subset. As mentioned earlier, the neural networks can frequently be stuck in local minima, resulting in very fluctuating performances. To evaluate different feature combinations reliably, a large number of neural networks have to be trained and the average performance of the networks would be used as the criterion for comparison. When training a classifier, the training data is divided to training, validation and test subsets, and the classifier is evaluated by its event 1 score on the test subset. A subset is evaluated by the average score of the one hundred classifiers and the subset with the highest score is chosen in each round. The best subset is then tested again using ten-fold cross validation. If the current round's best subset yields a worse result in the cross validation than the last two rounds' best subsets did, the algorithm would be stopped.

### 7.3.4 Classification

Among different kinds of data mining techniques, the artificial neural network is one of the most successful methods. It is widely used because of its capabilities like nonlinear learning, multi-dimensional mapping and noise tolerance [187]. In this work, our models were implemented using the artificial neural network toolbox in Matlab. The network models have one hidden layer with 15 neurons. The hyperbolic tangent sigmoid transfer function was used in both the hidden layer and the output layer. The Levenberg-Marquard algorithm [185] is adopted as the training function. The default cost function in Matlab ANN toolbox is the mean square error. For a binary classification problem, it was hypothesized that using maximum likelihood cost function would be better. That hypothesis was proved by five 10-fold cross validation tests in which the maximum likelihood cost function was observed to be clearly better in the five tests on average. The maximum likelihood cost function is defined as:

$$L = \frac{1}{m} \sum_{i=1}^{m} [-t_i \log(p_i) - (1 - t_i) \log(1 - p_i)]$$

In the function, $p_i$ represents the model's prediction for the ith sample, $t_i$ represents the true output for the ith sample, and $m$ is the number of samples.

### 7.3.5 Voting
*Random Voting*

As already mentioned in earlier sections, during neural network training, the optimization could often be stuck in local minima and result in very poor

classification accuracy [235]. In this work, a commonly used "voting" strategy was adopted to overcome that problem [179]. The method is described as below:

1.  Repeatedly train n neural networks (n=100 in this work)
2.  For an input record, each of the n neural networks generates an output for it
3.  The final output is the average of the n intermediate outputs generated in step 2

Figure 7-4 shows the flowchart of the ICU mortality prediction based on voting neural network classifiers. After obtaining the final output which is the average of the n intermediate outputs, a record is classified as died in-hospital if the output exceeds a predetermined threshold. Otherwise, it is classified as survivor. The threshold is not necessarily 50% because amounts of positive and negative records are not balanced in the data set. In this work, the threshold was determined from experimental experience.

*Voting Using Selected Models*

Alternative to the random voting strategy, a method of selecting classifiers was also proposed. The approach is summarized as following:

1.  Divide the training data into three subsets, respectively for training, validation and testing
2.  Train a classifier using the training data
3.  Evaluate the classifier's maximum likelihood cost function on the testing subset
4.  Go back to 1, and repeat steps 1-3 for a large number of times (3000 in this work)
5.  Choose 100 classifiers with the smallest costs from the large number of classifiers

Using this approach, not all of the n classifiers shown in Figure 7-4 will be used for voting, but only the 100 classifiers with the smaller costs will be used.
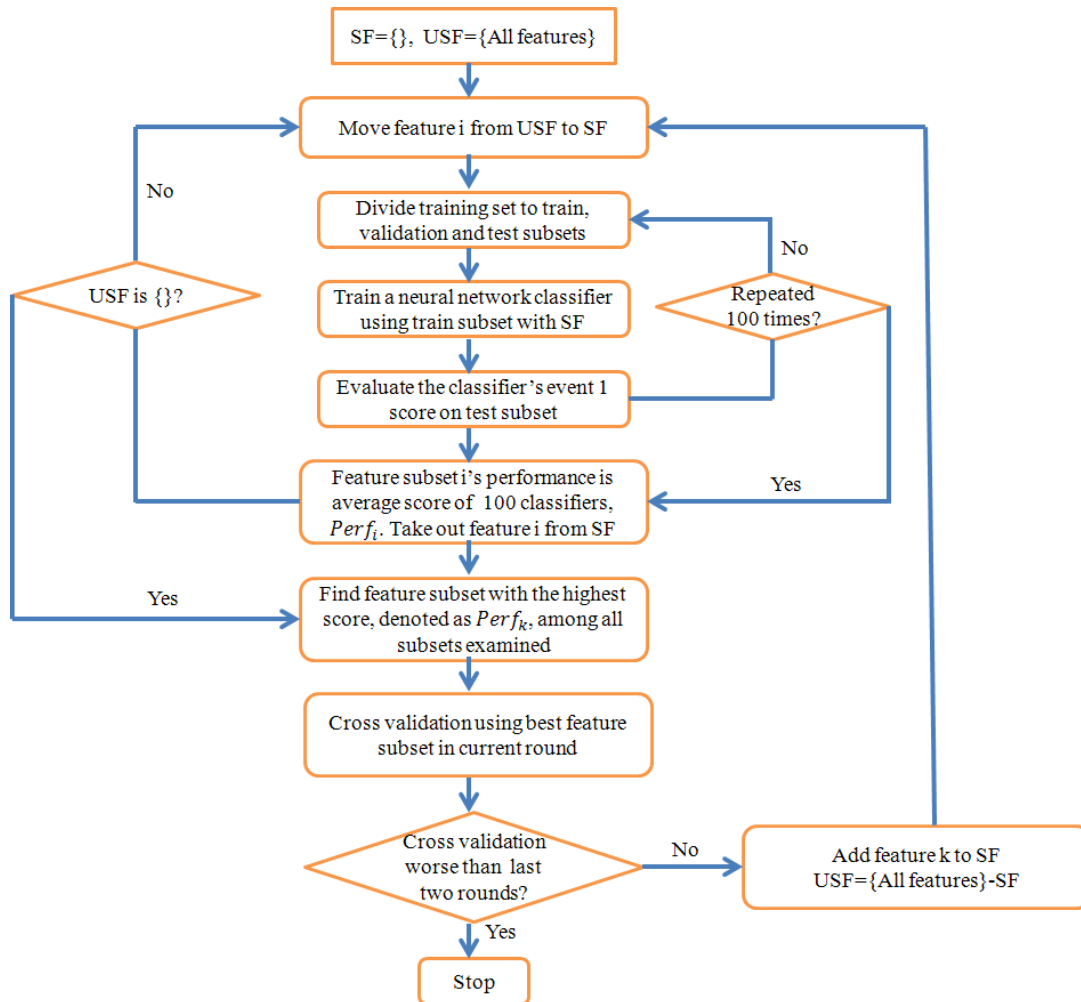
Figure 7-3: Flow chart of feature selection for neural network. Here, USF represents the set of "unselected features", and SF represents the set of "selected features."
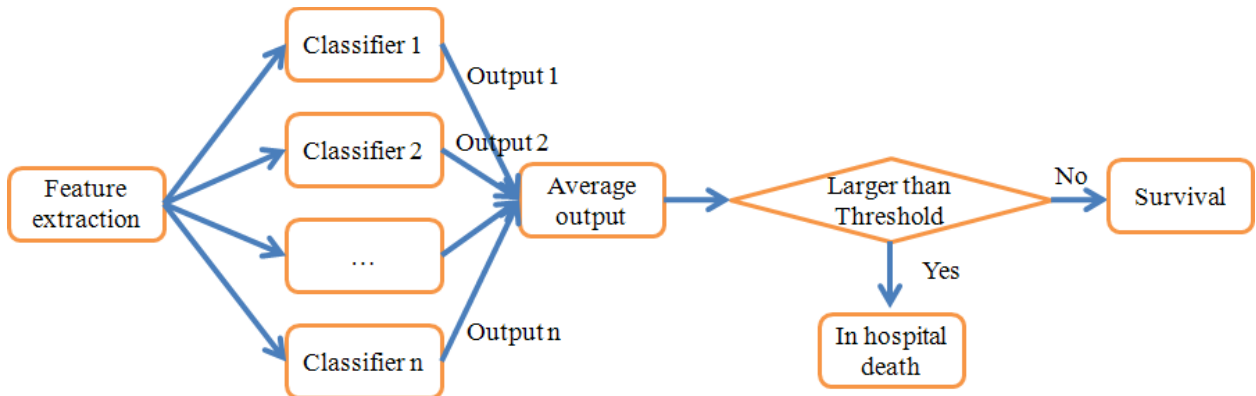
Figure 7-4: Flowchart for the ICU mortality prediction based on voting neural network classifiers

## 7.4 Results

### 7.4.1 Feature ranking

Each of the 205 features was used for classification independently. Figure 7-5 shows the performances of each individual feature. We also showed the twenty best individual features in Table 7-2. It shows that the variables "GCS", "Urine", "BUN" and "HCO3" are the most significant variables. To make sure every time-series variable appears at least once, 167 features which had better event 1 scores were kept, with the rest 38 abandoned.

### 7.4.2 Feature selection

Following the feature selection algorithm, a well performing subset including 47 features was identified. The four best individual variables "GCS", "Urine", "BUN" and "HCO3" were all included in the first 25 rounds.

In each round, 100 neural networks are trained, each with random initialization, and each has its own division of the train, validation and test subsets. The event 1 scores on the test subsets from the 100 networks can fluctuate largely. To reliably compare different feature combinations, the average of the 100 networks' performances were taken as the criterion for selecting the best one in each round. It is denoted as $\text{Perf}_k$ in Figure 7-3. These scores are used for selecting the best features in each round, but they can't be used to determine when to stop. Figure 7-6 shows the best test-subset event 1 score in each round. That score is not always increasing actually. This is because, at the beginning, there were 167 feature combinations, and thus the probability of a certain combination performing extraordinarily well was larger than when there were, for example, only 100 feature combinations left.

108
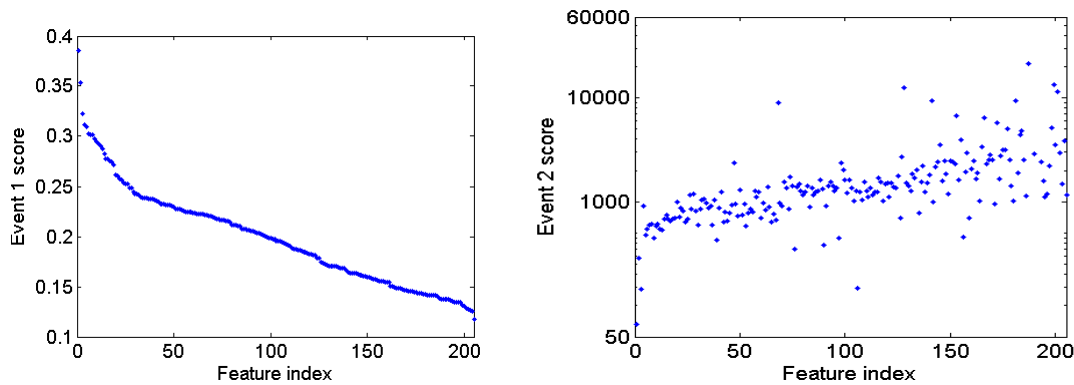
Figure 7-5: Performances of each individual feature. Left: the event 1 scores (minimum of sensitivity and PPV) obtained from each single feature in descending order; right: the event 2 scores from each single feature in ascending order

The cross validation performance was used to determine the stopping time. The cross validation tests may not be performed at every round, because it can be time consuming. These tests are performed using each round's best subset. To robustly measure the performance of a chosen feature combination, it has to be tested in multiple 10-fold cross validation tests to reduce randomness. These scores are used to determine when to stop the feature selection. In this work, an event 1 score of 0.5029 was achieved at the 47th round. After that, two continuous lower cross validation scores, 0.4978 and 0.4964 were obtained. See the red curve in Figure 6. Thus the algorithm was stopped and the first 47 chosen features were considered as the best subset.

Table 7-3 shows the results from using all 167 features and from using the chosen 47 features. It clearly shows that the chosen subset yields a much better classification performance. The thresholds for classifying between in hospital death and survivor are set as 0.26 for 47-feature algorithm and 0.27 for 167-feature algorithm. The thresholds are determined from experimental experience so that the event 1 score is maximized.

109

Table 7-2: Best 20 individual features

| Variable | Type of feature | Event 1 score (%) | Event 2 score |
|---|---|---|---|
| GCS | Last measurement | 38.57 | 66.06 |
| GCS | Average | 35.32 | 284.22 |
| GCS | Maximum | 32.24 | 142.29 |
| Urine | Sum | 31.18 | 914.16 |
| BUN | Last measurement | 30.93 | 480.43 |
| BUN | Minimum | 30.28 | 541.07 |
| HCO3 | Minimum | 30.15 | 596.11 |
| BUN | Average | 30.11 | 602.87 |
| BUN | Maximum | 29.80 | 448.89 |
| HCO3 | Average | 29.47 | 581.86 |
| PaCO2 | Average | 29.28 | 610.18 |
| Creatinine | Last measurement | 29.04 | 547.60 |
| HCO3 | Last measurement | 28.72 | 528.16 |
| GCS | Estimated trend | 28.27 | 683.25 |
| Creatinine | Minimum | 27.80 | 740.24 |
| Creatinine | Maximum | 27.73 | 682.28 |
| Creatinine | Average | 27.56 | 646.84 |
| PaCO2 | Last measurement | 27.43 | 679.46 |
| HCO3 | Maximum | 27.12 | 694.13 |
| ALP | Average | 26.14 | 993.01 |

Note: GCS represents Glasgow Coma Score (3-15), BUN represents Blood urea nitrogen (mg/dL), HCO3 represents Serum bicarbonate (mmol/L), ALP represents Alkaline phosphatase (IU/L), PaCO2 represents partial pressure of arterial CO2 (mmHg)

Table 7-3: Results from using all 167 features and from using the chosen 47 features

| | Accuracy (%) | Sensitivity (%) | PPV (%) | Event 1 score (%) | Event 2 score |
|---|---|---|---|---|---|
| All 167 features | 85.69±0.30 | 47.87±0.62 | 48.33±1.06 | 47.49±0.26 | 122.48±10.20 |
| Chosen 47 features | 86.23±0.14 | 50.29±0.22 | 50.29±0.50 | 50.29±0.22 | 119.55±9.87 |

Note: Average and standard deviation of five 10-fold cross validation tests are presented here
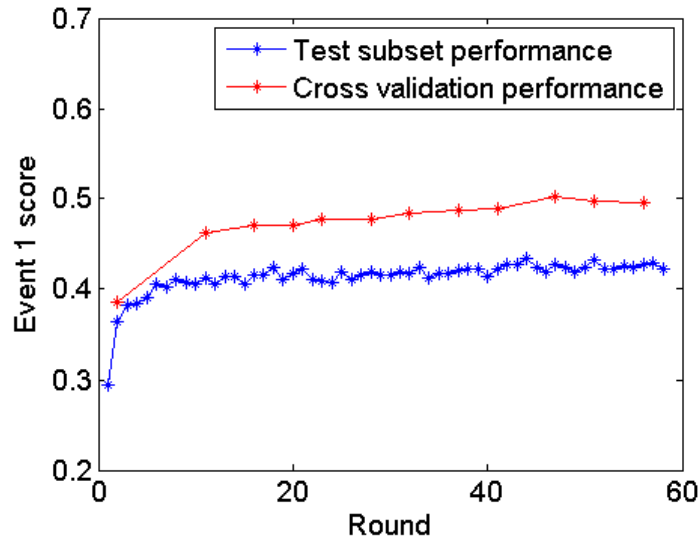
Figure 7-6: Performances on the test subset and on the cross validation. Blue: the best event 1 scores on the test subsets in each round; red: cross validation performances which are used to determine when to stop

### 7.4.3 Model selection

The voting strategy has been proved to be robust and well performing. However, this method didn't do well in the goodness of fit test, which was measured using the event 2 score. This may be caused by the influence of some really bad classifiers during voting. For example, Figure 7-7 shows that although most of the classifier gave fairly good event 2 scores, there were 12 extremely bad classifiers. If all 100 classifiers were used for voting, those extremely bad ones may harm the final event 2 score seriously. On the other hand, however the classification accuracy was not getting better after model selection. When selecting the 100 best classifiers from about 4000 trained classifiers, the event 2 score was significantly better but the event 1 scores was slightly worse. Table 7-4 compares the methods of random voting and model selection. The thresholds for classifying between in hospital death and survivor are set as 0.26 for random voting algorithm and 0.317 for model selection algorithm.

111

Table 7-4: Comparison between the methods of random voting and model selection

|  | Accuracy (%) | Sensitivity (%) | PPV (%) | Event 1 score (%) | Event 2 score |
|---|---|---|---|---|---|
| Random voting | 86.23±0.14 | 50.29±0.22 | 50.29±0.50 | 50.29±0.22 | 119.55±9.87 |
| Model selection | 86.17±0.00 | 49.75±0.59 | 50.07±0.24 | 49.75±0.58 | 41.39±3.41 |
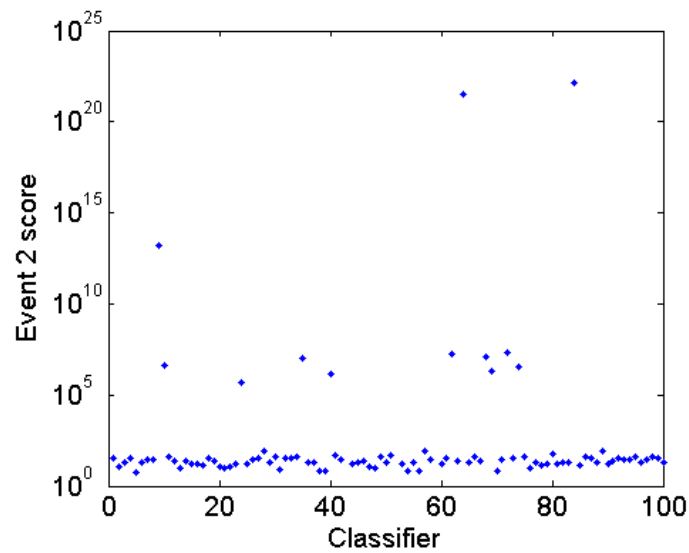


Figure 7-7: Event 2 scores of 100 classifiers. All classifiers are trained using the same data, each with random initialization. Most of the classifiers gave event 2 scores around 100, but there are 12 classifiers which gave event 2 sores larger than 105

### 7.4.4 Calibration

An optimization approach was proposed to calibrate the scores output from the neural network model. The scores were mapped to probabilities through a fourth degree polynomial function:

$$p = x_1 \cdot \text{score} + x_2 \cdot \text{score}^2 + x_3 \cdot \text{score}^3 + (1 - x_1 - x_2 - x_3) \cdot \text{score}^4$$

Coefficients $x_1$, $x_2$ and $x_3$ were determined by minimizing the event 2 score computed using $p$. Figure 7-8 shows a transfer function fitted. Figure 7-9 shows the effect of the conversion. After the transfer, scores of negative samples were more concentrated in the area of low scores. Scores of positive samples were also distributed more evenly.

When applying the calibration approach to the scores obtained using the neural network model selection algorithm. The event 2 score was observed to be further improved significantly. Figure 7-10 shows an example. After the calibration, the event 2 score was improved from 38.8562 to 23.2555. On average, the event 2 score was improved to 27.51±4.38 after the calibration.
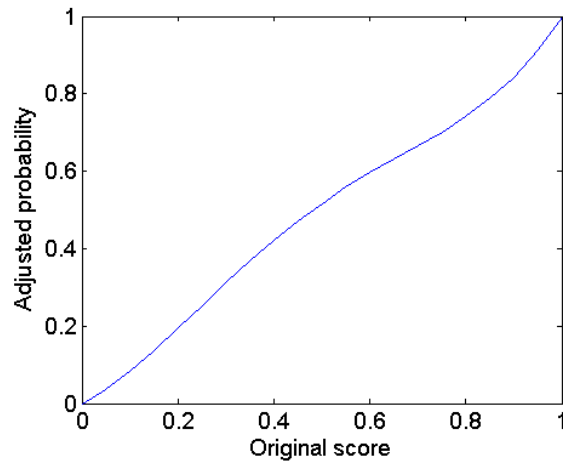
Figure 7-8: Transfer function from score to risk
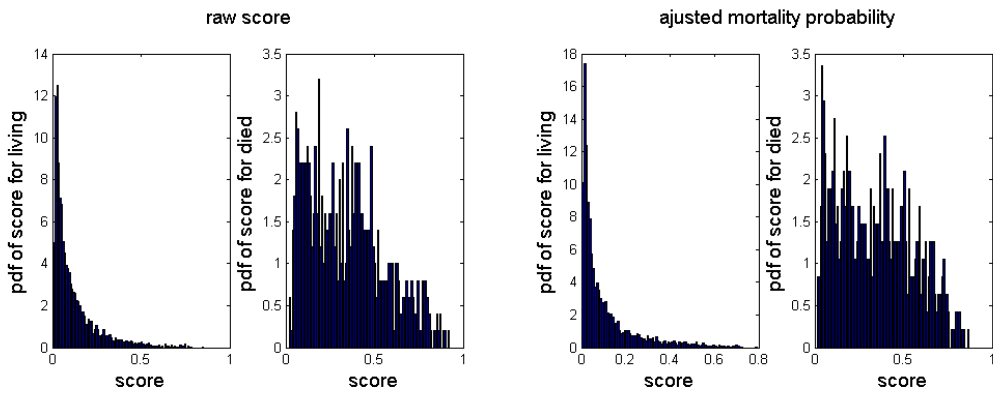


Figure 7-9: Probability density functions for raw scores (left) and adjusted mortality probabilities (right)
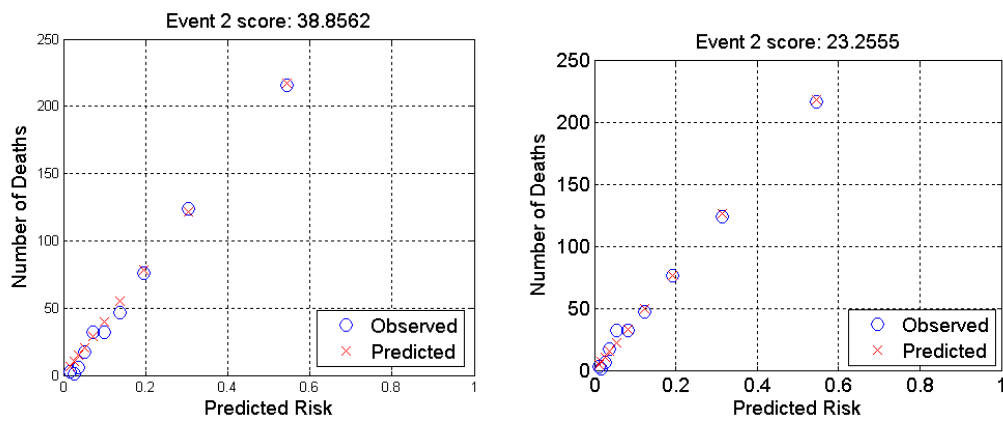


Figure 7-10: Event 2 score before (left) and after (right) calibration

114

# 7.5 Summary

In this chapter, an algorithm based on artificial neural network was developed for prediction of in-hospital death. Challenges from different perspectives were tackled.

The first challenge is that physiological variables were collected in an unstructured way. In different patients, they were collected at various moments and for various times. This requires to extract structured information from the data.

The second challenge is that missing measurements were common. It was not unusual that a variable was gathered from one patient but not from another one. An imputation method was thus necessary. We imputed the missing measurements based on a patient's gender. If a patient was male, a missing variable of that patient would be imputed by the median of that variable's values in all male patients, vice versa for female patients. If a patient's gender was unknown, imputation of a variable was the mean of that variable's medians in male and female patients, weighted by the frequencies of the males and females.

The third challenge came from the high dimension of the extracted features. A total of 205 features were extracted from the raw data. Each of the 205 features was used for the classification independently and the best feature yielded an event 1 score of 0.3857. The worst 38 features were abandoned. However, when using all the remaining 167 features, an event 1 score of only 0.4749 on average was achieved. This was understandable because among the 167 features, some of them didn't contain much useful information. In contrast, they could act as noise and cause the training data to be overfitted. Consequently, a greedy algorithm was proposed for feature selection. The algorithm added the best feature at each round. To decide when to stop the algorithm, cross-validation of the best subset at each round was performed.

After the feature selection, forty-seven features were selected. When applying to a data set with 4000 ICU records, we've got an accuracy of $(86.23\pm0.14)\%$, a sensitivity of $(50.29\pm0.22)\%$, a specificity of $(92.01\pm0.21)\%$, a positive prediction value of $(50.29\pm0.50)\%$, a negative prediction value of $(92.01\pm0.00)\%$ and a Lemeshow score of $119.55\pm9.87$ using the random voting strategy for classification. A much better Lemeshow score was achieved when using the 100 best classifiers out of 3000. An accuracy of $(86.17\pm0.00)\%$, a sensitivity of $(49.75\pm0.59)\%$, a specificity of $(92.03\pm0.15)\%$, a positive prediction value of $(50.07\pm0.24)\%$, a negative prediction value of $(91.93\pm0.00)\%$ and a Lemeshow score of $41.3981\pm3.41$ were obtained using the latter approach. An optimization approach was used to calibrate the predictive probabilities. The Lemeshow score was further reduced by 33%, from $41.3981\pm3.41$ to $27.51\pm4.38$.

# CHAPTER 8
# CONCLUSIONS AND RECOMMENDATIONS

## 8.1 Conclusions

In this dissertation, a fully coupled electromechanical model was first developed. This model accurately solved the electromechanics of the heart by fully coupling the cardiac electrophysiology and the cardiac mechanics in the same equations. Realistic electrophysiology models were adopted. Then the model was used to investigate two important problems numerically: the influence of sodium channel blocker on cardiac alternans and the influence of electro-mechanical coupling on discordant alternans. The sodium channel blocker was shown to lower the onset heart rate for cardiac alternans. The electromechanical coupling was found to influence the formation of discordant alternans significantly. Those new findings will improve the understanding of cardiac dynamics.

In the latter part of the dissertation, a well performing algorithm for detection of electrode misplacement during ECG collection was first developed. The dissertation then stated a new problem with current approaches in evaluating the electrode misplacement detection algorithms. Methods were proposed and they successfully resolved the problem.  Then a novel algorithm was developed to quantitatively evaluate the quality of ECG records and the algorithm achieved outstanding accuracy. Finally the dissertation proposed a novel and effective algorithm for the prediction of mortality in ICUs.

### 8.1.1 Computer simulation of heart dynamics

In this dissertation, a fully coupled electromechanical model of the heart was first presented. It has been a common approach in the literature to solve the electromechanics problem in an iterative manner. In each step, the electrical problem is solved first and then the results from the electrical solution are submitted into the mechanical problem, whose solution is then used to solve the electrical problem in the next step. Differently, in this work, a fully coupled scheme was developed to accurately solve the electromechanics of the heart. Realistic physiological models were adopted to describe the electrical and mechanical functions in the heart. The model was numerically solved using an implicit, finite element-based approach. Numerical simulations were conducted using parallel simulation in tissues of different geometries. The cardiac mechanics was described by the updated Lagrangian approach, which views the problem from the current configuration and takes derivatives and integrals with respect to the spatial coordinates. In perspective of mesh description, the updated Lagrangian description is characterized by making the material points remain coincident with mesh points. The developed model and computer codes were validated at each step using simple test examples to ensure accuracy in numerical computations. Multiple simulations were conducted using various meshes and parameters to ensure numerical robustness of the developed model.

Using the above mentioned model, the effects of sodium channel blockers were investigated. Multi-scale simulations were accomplished, and significant differences between different scales were observed, indicating the necessity of a multi-scale study upon cardiac issues. The drugs were found to significantly change the critical pacing period corresponding to the onset of alternans as well as the alternans' amplitude, but the effect of the drugs was found not consistent in three different electrophysiological models. On the whole, the drug has shown an adverse effect upon the electrical alternans. In addition, the changes in the onset of alternans were found to be dependent on the length of a fiber or the size of a tissue. Moreover, coexistence of multiple solutions in the tissues of the Shiferaw model was observed.

Moreover, the effects of the electro-mechanical coupling on cardiac alternans were investigated. The results showed that, the discordant alternans can be induced by the interaction of conduction velocity and action potential duration restitution at high pacing rates, no matter whether contraction is considered or not; however, when contraction is considered, the formation of the discordant alternans is in a very different way, and it's dependent on the boundary conditions.

### 8.1.2 Biomedical informatics and telemedicine

In this dissertation, an algorithm that includes two discrimination steps for automatic detection of limb cable reversals in ECG was developed and presented. The resampling was used to achieve more reliable evaluations and to improve the overall performance of the algorithm. Resampling the test set is necessary to reveal potential false positive predictions in practical applications. Resampling the training set yields optimal outcomes in all performance metrics. In the algorithm, Step 1 determines whether an ECG was correctly collected and Step 2 determines what the misplacement type is. Combing the two steps can warn the ECG operator about potential misplacement and can give suggestions about how to correct the error. The performance of Step 1 is 99.6% accuracy, 91.7% sensitivity, 99.9% specificity, 98.9% positive predictive value and 99.7% negative predictive value. The overall accuracy of Step 2 is 90.4%.

In this dissertation, a novel data fusion framework, called matrix of regularity (MoRE) was also presented to assess the quality of ECGs. The algorithm proved to be accurate and robust using ECG records from the Computing in Cardiology/Physionet Challenge 2011 [142]. Artifacts in ECGs may cause wrong diagnosis. A computer algorithm that can improve the quality of ECGs may have significant clinical relevance. Such algorithms can also be implemented in portable ECG devices to improve the quality of health care for those who do not have easy access to regular, high-quality clinics.  Compared to a conventional multi-step test algorithm, the algorithm developed in this dissertation provides integrative consideration of multiple quality tests. The

results can be regarded a natural fusion of multiple tests. Moreover, the algorithm generates continuous grades, which allows more accurate representation of the quality of an ECG. This algorithm can be combined with ROC analysis to help choose the optimal model for ECG evaluation. A user can choose different thresholds for different purposes. It is little or no additional cost to retake an ECG when the patient is at site. The cost of error for false positive is low. Thus, a practical algorithm may choose to have higher sensitivity to guarantee the quality of collected ECGs.

In this dissertation, an algorithm based on artificial neural network was developed for prediction of in-hospital mortality in ICU. Two hundred and five features were extracted from thirty-five time-series physiological variables. They were ranked according to their respective performance in ten ten-fold cross validation tests and the worst thirty-eight features were abandoned. An effective and efficient greedy algorithm for feature selection was developed to select the best feature subset from the remaining one hundred and sixty-seven features. An optimization approach was also used to calibrate the predictive probabilities

## 8.2 Recommendations for future work

### 8.2.1 Computer simulation of heart dynamics

The computations for cardiac simulation typically involve millions of nodes. The current framework of electrometrical model has limitations for real-time applications. In future studies, people can further improve the performance of the model using more efficient PDE solvers or implementing the model in CUDA [124]. In this dissertation, a simplified fiber configuration was adopted, where the normal of the fiber was assumed to point toward the geometric center of the heart. More realistic heart shape and fiber configurations should be utilized in future work for physiologically faithful parameter studies. Moreover, since Lagrangian meshes deform with material, the mesh may become distorted if the deformation of the heart is too large. Future work may also consider more detailed models for active stresses such as the hybrid model [110]. In the hybrid model, the active force is dependent on the [Ca2+]i, rather than the transmembrane potential, and this is more biophysically reasonable. Moreover, the hybrid model also takes into consideration binding of intracellular Ca2+ to troponin C, configuration change of tropomyosin, and interaction of actin and myosin, which is a more accurate description on excitation contraction interaction. Numerical simulations have been carried out for purpose of validating the model implementation in this paper, but more numerical experiments will be executed using the platform to investigate the interaction of electrical and mechanical functions in the heart and their influences to cardiac arrhythmias.

In this dissertation, the effects of the electro-mechanical coupling on cardiac alternans were investigated and some interesting phenomena were observed. In the future, the studies can be extended to tissues and the difference

in the APD distributions as well as in the formation of APD nodal line between tissues with and without mechanics can be investigated. More interesting results can be revealed by such studies.

### 8.2.2 Biomedical informatics and telemedicine

In this dissertation, an algorithm which is well developed and evaluated was presented. In the future, people should investigate misplacements involving both limb and precordial electrodes. Since the 10 electrodes produce millions of possible layouts of misplacement, a crucial step will be to determine a feasible set of electrodes that are most likely to be misplaced and the outcomes of their misplacements can seriously interfere subsequent diagnoses by physicians or by computers.

The algorithm for automatic evaluation of ECG signal quality won the first place in the Cardiology/Physionet Challenge 2011 [142]. However, the size of the data set used in this study is limited and not all types of artifacts are well represented. Since the Physionet ECGs were annotated by a group of volunteer reviewers with a wide range of expertise in ECG, the reference classifications show inconsistency and large variances. More careful annotations on these data may be necessary for future research to further improve the algorithms for physiological signal quality evaluation. Annotating is a subjective process. We believe consistent references rely on a systematic method of annotating. A consensus in rules has to be achieved beforehand to reduce variances between reviewers and records. It will also be interesting to study the cross correlations between the classifications by different groups of annotators, as indicated by statistics in [142].

The ICU prediction algorithm presented in this dissertation gave a very good performance, but it is still not perfect. In the next step, ensemble algorithms can be explored in order to combine individual weaker classifiers to a strong classifier for better classification accuracy.

# LIST OF REFERENCES

[1]     Kochanek KD, Xu J, Murphy SL, Miniño AM and Kung HC 2011 Deaths: Final Data for 2009 *National Vital Statistics Report* **60:** 3

[2]     Kelly BB, Valentin F 2010 Promoting Cardiovascular Health in the Developing World: A Critical Challenge to Achieve Global Health *Washington, D.C: National Academies Press ISBN 0-309-14774-3*

[3]     Anthea 1993 Human Biology and Health *Englewood Cliffs, New Jersey: Prentice Hall ISBN 0-13-981176-1*

[4]     Centers for Disease Control and Prevention 2008 CDC-DHDSP-Heart Disease Risk Factors *Centers for Disease Control and Prevention: http://cdc.gov/heartdisease/risk_factors.htm*

[5]     Centers for Disease Control and Prevention 2008 FASTSTATS – Hypertension *Centers for Disease Control and Prevention: htttp://www.cdc.gov/nchs/fastats/hyprtens.htm*

[6]     Mayo Clinic 2008 Arteriosclerosis/atherosclerosis *Mayo Clinic.com: http://www.mayoclinic.com/health/arteriosclerosis-atherosclerosis/DS00525*

[7]     Mayo Clinic 2008 Diabetes: Complications *Mayo Clinic.com: http://www.mayoclinic.com/health/diabetes/DS01121/DSECTION=complications*

[8]     U.S. Census Bureau 2009 US POPClock Projection *U.S. Census Bureau: http://www.census.gov/population/www/popclockus.html*

[9]     Mendis S, Puska P and Norrving B 2011 Global Atlas on cardiovascular disease prevention and control *ISBN 978-92-4-156437-3*

[10]    Vadakkumpadan F, Gurev V, Constantino J, Arevalo H and Trayanova N 2010 Modeling of whole-heart electrophysiology and mechanics: Towards patient-specific simulation *Patient Specific Modeling of the Cardiovascular System Ed. Roy C. P. Kerckhoffs, Springer Science+Business Media* 145-165

[11]    Hodgkin A and Huxley A 1952 A quantitative description of membrane current and its application to conduction and excitation in nerve *J. Physiol.* **117**: 500–544

[12]    Fenton FH and Cherry EM 2008 Models of cardiac cell *Scholarpedia* **3**(8): 1868

[13]    Nash MP, Panfilov AV 2004 Electromechanical model of excitable tissue to study reentrant cardiac arrhythmias *Prog Biophys Mol Biol* **85**: 501–522

[14]    FitzHugh R 1955 Mathematical models of threshold phenomena in the nerve membrane *Bull. Math. Biophysics* **17**: 257—278

[15]    Niederer S, Hunter P and Smith N 2006 A Quantitative Analysis of Cardiac Myocyte Relaxation: A Simulation Study *Biophysical Journal* **90**: 1697-1722

[16]    Gurev V, Lee T, Constantino J, Arevalo H and Trayanova NA 2010 Models of cardiac electromechanics based on individual hearts imaging data: image-based electromechanical models of the heart *Biomech Model Mechanobiol* **10**(3): 295-306

[17]    Göktepe S and Kuhl E 2010 Electromechanics of the heart: a unified approach to the strongly coupled excitation-contraction problem *Computational Mechanics* **45**: 227-243

[18] Doyle MG, Tavoularis S, and Bourgault Y 2010 Application of Parallel Processing to the Simulation of Heart Mechanics *High Performance Computing Systems and Applications, Lecture Notes in Computer Science* **5976**: 30-47

[19] Lafortune P, Arís R, Vázquez M and Houzeaux G 2012 Coupled electromechanical model of the heart: Parallel finite element formulation *Int. J. Numer. Meth. Biomed. Engng* **28**: 72–86

[20] Fenton F and Karma A 1998 Vortex dynamics in three-dimensional continuous myocardium with fiber rotation: Filament instability and fibrillation *Chaos* **8**: 20-47

[21] Clayton RH, Bernus O, Cherry EM, Dierckx H, Fenton FH, Mirabella L, Panfilov AV, Sachse FB, Seemann G, Zhang H 2011 Models of cardiac tissue electrophysiology: progress, challenges and open questions *Prog. Biophys. Mol. Biol.* **104**: 22–48

[22] Kohl P, Sachs F 2011 Mechanoelectric feedback in cardiac cells *Phil. Trans. R. Soc. Lond. A* **359**: 1173–1185.

[23] Cherubini C, Filippi S, Nardinocchi P, Teresi L 2008 An electromechanical model of cardiac tissue: constitutive issues and electrophysiological effects *Prog. Biophys. Mol. Biol.* **97**: 562–573

[24] N. H. L. Kuijpers, H. M. M. ten Eikelder, P. H. M. Bovendeerd, S. Verheule, T. Arts, P. A. J. Hilbers 2007 Mechanoelectric feedback leads to conduction slowing and block in acutely dilated atria: a modeling study of cardiac electromechanics Am. J. Physiol. Heart Circ. Physiol. 292: H2832–2853.

[25] http://en.wikipedia.org/wiki/File:Gray501.png

[26] Hoffman and Rosen 1981 Cellular mechanisms for cardiac arrhythmias *Circulation Research* **49**:1

[27] Guyton and Hall 2010 Text book of medical physiology, 10th edition *W.B. Saunders Company*

[28] Krinsky 1966 Spread of excitation in an inhomogeneous medium (state similar to cardiac fibrillation) *Biophysics-USSR* **11**(4): 676-683

[29] Nattel and Carlsson 2006 Innovative approaches to anti-arrhythmic drug therapy *Nature Reviews Drug Discovery* **5**

[30] Morrow, Cannon, and Reiffel 2007 New antiarrhythmic drugs for establishing sinus rhythm in atrial fibrillation: What are our therapies likely to be by 2010 and beyond *Am Heart J* **154**: 824-9

[31] Hammwöhner, Smid, Lendeckel and Goette 2008 New drugs for atrial fibrillation *J Interv Card Electrophysiol* **23**:15–21

[32] Nattel, Takeshita, Brundel, and Rivard 2005 Mechanisms of Atrial Fibrillation: Lessons From Animal Models *Progress in Cardiovascular Diseases* **48**(1): 9-28

[33] Cardiac Arrhythmia Suppression Trial Investigators 1989 Preliminary report: Effect of encainide and flecainide on mortality in a randomized trial of arrhythmia suppression after myocardial infarction *New Eng. J. Med.* **321**: 406-412

[34] Cardiac Arrhythmia Suppression Trial-II Investigators 1992 Effect of the antiarrhythmic agent moricizine on survival after myocardial infarction *N. Eng. J. Med.* **327**: 227-233

[35] Starmer 2002 How antiarrhythmic drugs increase the rate of sudden cardiac death *International Journal of Bifurcation and Chaos* **12**(9): 1953-1968

[36] Zhao 2008 Indeterminacy of Spatiotemporal Cardiac Alternans *Physical Review E* **78**: 011902

[37] Berger, Zhao, Schaeffer, Krassowska, Dobrovolny, and Gauthier 2007 Period-doubling bifurcation to alternans in paced cardiac tissue: Crossover from smooth to border-collision characteristics *Physical Review Letters* **99**: 058101

[38] Riccio, Koller and Gilmour 1999 Electrical Restitution and Spatiotemporal Organization During Ventricular Fibrillation *Circulation Research* **84**: 955-963

[39] Koller, Riccio, and Gilmour 1998 Dynamic restitution of action potential duration during electrical alternans and ventricular fibrillation *Am J Physiol Heart Circ Physiol* **275**: H1635-H1642

[40] Smith, Clancy, Valeri, Ruskin and Cohen 1988 Electrical alternans and cardiac electrical instability *Circulation* **77**:110-121

[41] Weiss, Karma, Shiferaw, Chen, Garfinkel and Qu 2006 From Pulsus to Pulseless: The Saga of Cardiac Alternans *Circ Res* **98**: 1244-1253

[42] Watanabe, Fenton, Evans, Hastings and Karma 2001 Mechanisms for Discordant Alternans *Journal of cardiovascular electrophysiology* **12**(2)

[43] Rosenbaum DS, Jackson LE, Smith JM, Garan H, Ruskin JN, Cohen RJ 1994 Electrical alternans and vulnerability to ventricular arrhythmias *N Engl J Med* **330**: 235-241.

[44] Estes NAM, Michaud G, Zipes DP, El-Sherif N, Venditti FJ, Rosenbaum DS, Albrecht P, Wang PJ, Cohen RJ 1997 Electrical alternans during rest and exercise as predictors of vulnerability to ventricular arrhythmias *Am J Cardiol* **80**: 1314-1318

[45] Pastore JM, Girouard SD, Laurita KR, Akar FG, Rosenbaum DS 1999 Mechanism linking T-wave alternans to the genesis of cardiac fibrillation *Circulation* **99**: 1385-1394

[46] Kohl P and Ravens U 2003 Cardiac mechano-electric feedback: past, present, and prospect *Prog. Biophys. Mol. Biol.* **82**: 3–9

[47] Dean JW, Lab MJ 1989 Arrhythmia in heart failure: role of mechanically induced changes in electrophysiology *Lancet* **1**: 1309–1311

[48] Calaghan SC, White E 1999 The role of calcium in the response of cardiac muscle to stretch *Prog Biophys Mol Biol.* **71**(1): 59-90

[49] Allen DG, Eisner DA, Orchard CH 1984 Characterization of oscillations of intracellular calcium concentration in ferret ventricular muscle *J. Physiol.* **352**: 113–28

[50] Kohl P, Hunter P, Noble D 1999 Stretch-induced changes in heart rate and rhythm: clinical observations, experiments and mathematical models *Prog. Biophys. Molec. Biol.* **71**: 91–138

[51] Lab MJ, Seed WA 1993 Pulsus alternans *Cardiovasc. Res.* **27**: 1407–1412

[52] Pye MP, Cobbe SM 1996 Arrhythmogenesis in experimental models of heart failure: the role of increased load *Cardiovasc. Res.* **32**: 248–257

[53] Braunwald E 2001 Heart Disease: A Textbook of Cardiovascular Medicine, Fifth Edition *Philadelphia, W.B. Saunders Co.* p108

[54] Dubin D 2000 Rapid interpretation of EKG's *Hong Kong, Cover Inc*

[55] Rudiger A, Hellermann JP, Mukherjeec R, Follath F and Turina J 2007 Electrocardiographic artifacts due to electrode misplacement and their frequency in different clinical settings *American Journal of Emergency Medicine* **25**: 174-8

[56] Criley JM and Nelson P 2006 Virtual tools for teaching electrocardiographic rhythm analysis *J Electrocardiol* **39**: 113–9

[57] Thaler T and Rudiger A 2011 How to Diagnose ECG artifacts due to electrode misplacements *Intensive Care Med* **37**: 891-2

[58] Tam HW and Webster JG 1977 Minimizing Electrode Motion Artifact by Skin Abrasion *IEEE Trans. on Biomedical Engineering* **24**: 134-9

[59] Clochesy JM, Cifani L and Howe K 1991 Electrode site preparation techniques: a follow-up study *Heart Lung* **20**: 27-30

[60] Drew BJ 1991 Bedside electrocardiographic monitoring: state of the art for the 1990s *Heart Lung* **20**: 610-23

[61] Batchvarov VN, Malik M, and Camm AJ 2007 Incorrect electrode cable connection during electrocardiographic recording *Europace* **9**: 1081-90

[62] Castellanos A, Pastor JA, Zambrano JP and Myerburg RJ 2002 Left bundle-branch block with technical right-axis deviation *Circulation* **106**: 2288-9

[63] Dhingra RC, Wyndham C, Ehsani AA and Rosen KM 1975 Left anterior hemiblock concealing diaphragmatic infarction and simulating anteroseptal infarction *Chest* **67**: 713-15

[64] Green J and Palma E 2003 Variable pattern of preexcitation: what is the mechanism? *J Cardiovasc Electrophysiol* **14**: 435-6

[65] Chanarin N, Caplin J and Peacock A 1991 'Pseudo reinfarction': a consequence of electrocardiogram lead transposition following myocardial infarction *Clin Cardiol* **13**: 668-9

[66] Marafioti V and Variola A 2004 Pseudo infarction pattern by misplacement of electrocardiographic precordial leads *Am J Emerg Med* **22**: 62-3

[67] Akel R, Saeed M, Ware DL, Chamoun AJ and Birnbaum Y 2004 Unusual evolution of ST elevation acute myocardial infarction *Ann Noninvas Electrocardiol* **9**: 410-4

[68] Horwitz S and Medrano G 1976 Left anterior hemiblock or inadvertent lead misplacement? *Chest* **69**: 449-50

[69]  Rudiger A, Schoob L and Follath F 2003 Influence of electrode misplacement on the electrocardiographic signs of inferior myocardial ischemia *Am J Emerg Med* **21**: 574-7

[70]  Haisty WK, Pahlm O and Edenbrandt L 1993 Recognition of electrocardiographic electrode misplacements involving the ground (right leg) electrode *Am J Cardiol* **71**: 1490-95

[71]  Macfarlane PW and Lawrie TDV 1989 Comprehensive electrocardiology *Oxford: Pergamon Press Inc* **3**: 1529-30.

[72]  Marquette Electronics 1988 Physicians Guide to Marquette Electronics Resting ECG Analysis *Milwaukee*

[73]  Heden B 2001 Electrocardiographic lead reversal *Am J Cardiol* **87**: 126-7

[74]  Surawicz B and Knilans TK 2001 Misplacement of leads and electrocardiographic artifacts *Surawicz B, Knilans TK eds, Chow's Electrocardiography in Clinical Practice. Philadelphia: WB Saunders* p569-82

[75]  Zielinski J 1976 Negative P wave in lead I due to right atrial enlargement and displacement of the heart in the chest *Lung* **153**: 197-201

[76]  Friedman WF 1980 Congenital heart disease in infancy and childhood 1980 *Brawnwald E, ed. Heart Disease. A Textbook of Cardiovascular Medicine. Philadelphia: WB Saunders* p1035

[77]  Abdollah H and Milliken JA 1997 Recognition of electrocardiographic left arm/left leg lead reversal *Am J Cardiol* **80**: 1247-49

[78]  Ho KKL and Ho SK 2001 Use of the sinus P wave in diagnosing electrocardiographic limb lead misplacement not involving the right leg (ground) electrode *J Electrocardiol* **34**: 161-71

[79]  Baranchuk A, Shaw C, Alanazi H, Campbell D, Bally K, Redfearn DP, Simpson CS and Abdollah H. 2009 Electrocardiography pitfalls and artifacts: the 10 commandments *Crit Care Nurse.* **29**: 67-73.

[80]  Riddle W 2008 Misleading: The clinical implications of misplaced ECG leads *Journal of Emergency Medical Services* **33**: 9-56

[81]  Feldman CL, Hubelbank M, Haffajee CI and Kotilainen P 1979 A new electrode system for automated ECG monitoring *Computers in Cardiology* pp 285–8

[82]  Sheffield LT, Prineas R, Cohen HC, Schoenberg A and Froelicher V 1978 Task Force II: Quality of electrocardiographic records *Am. J. Cardiol.* **41**: 146–5

[83]  Allen J and Murray A 1996 Assessing ECG signal quality on a coronary care unit *Physiol. Meas.* **17**: 249–58

[84]  Riddle W 2008 Misleading: The clinical implications of misplaced ECG leads *JEMS* **33**: 56-62

[85]  Anderson G and Hussey PS 2001 Comparing health system performance in OECD countries *Health Aff* **20**: 219-32

[86]  National Academy of Engineering 2011 Grand challenges for engineering http://www.engineeringchallenges.org/cms/8996.aspx

[87] Jones V, Halteren A V, Widya I, Dokovsky N, Bults R, Konstantas D, Herzog R 2006 Mobihealth: Mobile Health Services Based on Body Area Networks, in: Topics in Biomedical Engineering, *Springer US*, Boston, MA

[88] Buyya R, Yeoa C S, Venugopala S, Broberga J and Brandic I 2008 Cloud computing and emerging IT platforms: Vision, hype, and reality for delivering computing as the 5th utility *Future Generation Computer Systems* **25**: 599-616

[89] Armbrust M, Fox A, Griffith R, Joseph A D, Katz R, Konwinski A, Lee G, Patterson D, Rabkin A, Stoica I and Zahari M 2010 A view of cloud computing *Communications of the ACM* **55**: 50-58

[90] Deelman E, Singh G, Livny M, Berriman B and Good J 2008 The cost of doing science on the cloud: the montage example *in: Proceedings of the 2008 ACM/IEEE Conference on Supercomputing, IEEE Press* pp. 1–12

[91] International Data Corporation 2009 http://blogs.idc.com/ie/wpcontent/uploads/2009/12/ idc_cloud_challenges_2009.jpg

[92] Gartner Inc. 2012 http://www.gartner.com/technology/home.jsp

[93] Hoang D B and Chen L 2010 Mobile Cloud for Assistive Healthcare (MoCAsH) *IEEE Asia-Pacific Services Computing Conference (APSCC)* p325 - 332

[94] McGregor C, Heath J and Ming Wei 2005 A Web services based framework for the transmission of physiological data for local and remote neonatal intensive care The 2005 *IEEE International Conference Proceedings on e-Technology, e-Commerce and e-Service* 496-501

[95] Pandeya S, Voorsluys W, Niua S, Khandoker A and Buyyaa R 2012 An autonomic cloud environment for hosting ECG data analysis services *Future Generation Computer Systems* **28**: 147–54

[96] Hanson C, Marshall B 2001 Artificial intelligence applications in the intensive care unit. Crit Care Med **29**(2):1—9

[97] Dasta JF, McLaughlin TP, Mody SH, Piech CT 2005 Daily cost of an intensive care unit day: the contribution of mechanical ventilation *Crit Care Med.* **33**(6):1266-71.

[98] Knaus WA, Zimmerman JE, Wagner DP, Draper EA, Lawrence DE 1981 APACHE-acute physiology and chronic health evaluation: a physiologically based classification system *Crit Care Med.* **9**(8): 591-7.

[99] Knaus WA, Draper EA, Wagner DP, Zimmerman JE 1985 APACHE II: a severity of disease classification system *Critical Care Medicine* **13**(10): 818–29

[100] LeGall JR, Loirat P, Alperovitch A, Glaser P, Granthil C, Mathieu D, Mercier P, Thomas R, Villers D 1984 A simplified acute physiology score for ICU patients *Crit Care Med.* **12**(11): 975-7.

[101] Lemeshow S, Klar J, Teres D, Avrunin JS, Gehlbach SH, Rapoport J, Rué M. 1994 Mortality probability models for patients in the intensive care unit for 48 or 72 hours: a prospective, multicenter study *Crit Care Med.* **22**(9): 1351-8.

[102] Dybowski R,Weller P, Chang R, Gant V 1996 Prediction of outcome in critically ill patients using artificial neural network synthesised by genetic algorithm *Lancet* **347**(9009): 1146—50.

[103] Nimgaonkar A, Sudarshan S 2004 Predicting hospital mortality for patients in the intensive care unit: a comparison of artificial neural networks with logistic regression models *Intensive Care Med* **30**: 248—53

[104] Cios K, Moore G 2002 Uniqueness of medical data mining *Artif Intell Med* **26**:1—24.

[105] Hand D, Mannila H, Smyth P 2001 Principles of data mining *Cambridge, MA, USA: MIT Press*

[106] Haykin S 1999 Neural networks — a comprehensive foundation, 2nd ed, *New Jersey, USA: Prentice-Hall*

[107] Silva A, Cortez P, Santos MF, Gomes L, Neves J 2006 Mortality assessment in intensive care units via adverse events using artificial neural networks *Artificial Intelligence in Medicine* **36**: 223—234

[108] Wong L, Young J 1999 A comparison of ICU mortality prediction using the APACHE II scoring system and artificial neural networks *Anaesthesia* **54**:1048—54

[109] Beeler and Reuter 1977 Reconstruction of the action potential of ventricular myocardial fibers *J. Phyaiol* **268**: 177-210

[110] Knutsson H 1989 Representing local structure using tensors *Proceedings 6th Scandinavian Conf. on Image Analysis* pp. 244–251

[111] Sachse FB, Glanzel KG and Seemann G 2003 Modeling of protein interactions involved in cardiac tension development *International Journal of Bifurcation and Chaos* **13**(12): 3561-3578

[112] Guharay F and Sachs F 1984 Stretch-activated single ion channel currents in tissue-cultured embryonic chick skeletal muscle *J. Physiol.* **352**: 685-701

[113] Keldermann R, Nash M, Panfilov A 2007 Pacemakers in a reaction–diffusion mechanics system *J Stat Phys* **128**: 375–392

[114] Bjorhus M 1988 Operator Splitting for abstract Cauchy problems *IMA Journal of Numerical Analysis* **18**: 419-443.

[115] Leonhard Euler 1769 Institutionum calculi integralis, Volume 2 *imp. Acad. imp. Saènt*

[116] Gaidamour J and Hénon P 2010 INRIA team-project Scalapplix, http://hips.gforge.inria.fr/index.html

[117] Message Passing Interface (MPI) standard 2012, http://www.mcs.anl.gov/research/projects/mpi/

[118] Karypis G 2012 http://glaros.dtc.umn.edu/gkhome/views/metis

[119] Heroux M, Bartlett R, Howle V, et al. 2003 An Overview of Trilinos, Sandia National Laboratories, http://trilinos.sandia.gov/TrilinosOverview.pdf

[120] Saad Y and Schultz MH 1986 GMRES: A generalized minimal residual algorithm for solving nonsymmetric linear systems *Siam J. Sci. Stat. Comput.* **7**(3): 856-869

[121] Kraken 2012 National Institute for Computational Sciences(NICS), http://www.nics.tennessee.edu/

[122] Department of Energy (DOE) 2012 Advanced Simulation and Computing Initiative (ASCI) https://wci.llnl.gov/codes/visit/

[123] Kohl P, Ravens U 2003 Cardiac mechano-electric feedback: past, present, and prospect *Prog. Biophys. Mol. Biol.* **82**: 3–9

[124] Hunter PJ, Nielsen PM, Smaill BH, LeGrice IJ, Hunter IW 1992 An anatomical heart model with applications to myocardial activation and ventricular mechanics *Crit Rev Biomed Eng.* **20**(5-6): 403-26.

[125] NVIDIA 2012 http://www.nvidia.com/object/cuda_home_new.html

[126] Fox, McHarg and Gilmour 2002 Ionic mechanism of electrical alternans, *Am J Physiol Heart Circ Physiol* **282**: H516–H530

[127] Shiferaw 2003 Model of Intracellular Calcium Cycling in Ventricular Myocytes *Biophysical Journal* **85**: 3666–3686

[128] Rudy et al. 2008 Systems Approach to Understanding Electromechanical Activity in the Human Heart: A National Heart, Lung, and Blood Institute Workshop Summary *Circulation* **118**: 1202-1211

[129] Winslow, Rice, Jafri, Marban and Rourke 1999 Mechanisms of altered excitation-contraction coupling in canine tachycardia-induced heart failure. II. Model studies *Circ Res* **84**: 571-586.

[130] Qu and Garfinkel 1999 An Advanced Algorithm for Solving Partial Differential Equation in Cardiac Conduction *IEEE Transactions on Biomedical Engineering* **46**: 9

[131] Strang 1968 On the Construction and Comparison of Difference Schemes *SIAM Journal on Numerical Analysis* **5**(3): 506-517

[132] Elharrar and Surawicz 1983 Cycle length effect on restitution of action potential duration in dog cardiac fibers *Am J Physiol Heart Circ Physiol* **244**: H782-H792

[133] Moss and Gielen 2001 Handbook of Biological Physics *Elsevier B.V.* **4**(7): 229-255

[134] Kalb SS, Dobrovolny HM, Tolkacheva EG, Idriss SF, Krassowska W, Gauthier DJ 2004 The restitution portrait: a new method for investigating rate-dependent restitution *J Cardiovasc Electrophysiol* **15**: 698–709

[135] Echebarria and Karma 2002 Instability and Spatiotemporal Dynamics of Alternans in Paced Cardiac Tissue *Physical Review Letters* **88**(20)

[136] Echebarria and Karma 2007 Amplitude equation approach to spatiotemporal dynamics of cardiac alternans *Physical Review E* **76**: 051911

[137] Panfilov AV, Keldermann RH, Nash MP 2005 Self-organized pacemakers in a coupled reaction-diffusion mechanics system *Phys Rev Lett* **95**: 258

[138] Aliev RR and Panfilov AV 1996. A simple two-variable model ofcardiac excitation *Chaos, Solitons and Fractals* **7**(3): 293–301

[139] Goldberger AL, Amaral L, Glass L, Hausdorff JM, Ivanov P, Mark RG, Mietus JE, Moody GB, Peng CK and Stanley HE 2000 PhysioBank, PhysioToolkit, and PhysioNet: Components of a New Research Resource for Complex Physiologic Signals *Circulation* **101**: e215-e220

[140] Bousseljot R, Kreiseler D, Schnabel A 1995 Nutzung der EKG-Signaldatenbank CARDIODAT der PTB über das Internet *Biomedizinische Technik* **40**: S317-S318

[141] Tihonenko V and Khaustov A 2007 http://physionet.org/pn3/incartdb

[142] Silva I, Moody GB and Celi L 2011 Improving the Quality of ECGs Collected Using Mobile Phones: The PhysioNet / Computing in Cardiology Challenge 2011 *Computing in Cardiology* **38**: 273-6

[143] Heden B, Ohlsson M, Edenbrandt L, Rittner R, Pahlm O and Peterson C 1995 Artificial Neural Networks for Recognition of Electrocardiographic Lead Reversal *Am. J Cardiol* **75**: 929-933

[144] Heden B, Ohlsson M, Holst H, Mjijman M, Rittner R, Pahlm O, Peterson C, and Edenbrandt L 1996 Detection of Frequently Overlooked Electrocardiographic Lead Reversals Using Artificial Neural Networks *The American Journal of Cardiology* **78**: 600-4

[145] Kors J A and Herpen G 2001 Accurate automatic detection of electrode interchange in the electrocardiogram *Am J Cardiol* **88**: 396-9

[146] Oppenheim AV 1975 Digital Signal Processing *Prentice Hall; US edition*

[147] Leski JM and Henzel N 2005 ECG baseline wander and powerline interference reduction using nonlinear filter bank *Signal Processing* **85**: 781-93

[148] Clifford G, Azuaje F and McSharry P 2006 Advanced methods and tools for ECG data analysis Artech *House Publishers* 1 edition 304-311

[149] Legarreta I R, Addison P S, Reed M J, Grubb N, Clegg G R, Robertson C E and Watson J N 2005 Continuous wavelet transform modulus maxima analysis of the electrocardiogram: beat characterisation and beat-to-beat measurement *International Journal of Wavelets, Multiresolution and Information Processing* **3**: 19-42

[150] Laguna P, Jané R and Caminal P 1994 Automatic Detection of Wave Boundaries in Multilead ECG Signals: Validation with the CSE Database *Computers and Biomedical Research* **27**: 45-60

[151] Huhta JC and Webster J G 1973 60-Hz interference in electrocardiography *IEEE Trans. Biomed. Eng.* **20**: 91–101

[152] Murray A, Campbell RWF and Julian DG 1978 Optimum ECG morphology and quality for increased accuracy in automatic analysis of 24 hour ECG recordings *Computers in Cardiology* 225–8

[153] Zywietz C, Bemmel JH and Degani R 1990 Evaluation of ECG interpretation systems: Signal analysis *Methods Inform. Med.* **29**: 298–30

[154] Bemmel JH and Weide H 1966 Detection procedure to represent the foetal heart rate and electrocardiogram *IEEE Trans. Biomed. Eng.* **13**: 175–82

[155] Oehler M, Ling V, Melhorn K and Schilling M 2008 A multichannel portable ECG system with capacitive sensors *Physiol. Meas.* **29**: 783–93

[156] Oppenheim A and Schafer R 2009 Discrete-Time Signal Processing, 3rd ed. *Englewood Cliffs, NJ: Prentice Hall*

[157] Abboud S and Sadeh D 1989 Spectral analysis of the fetal electrocardiogram *Comput. Biol. Med.***19**: 409–15

[158] Bailey J, Berson A, Garson A, Horan L, Macfarlane P, Mortara D, and Zywietz C 1990 Recommendations for standardization and specifications in automated electrocardiography: Bandwidth and digital signal processing. A report for health professionals by an ad hoc writing group of the Committee on Electrocardiography and Cardiac Electrophysiology of the Council on Clinical Cardiology, American Heart Association *Circulation* **81**: 730–39

[159] Vullings R, Vries B and Bergmans JWM 2011 An Adaptive Kalman Filter for ECG Signal Enhancement *IEEE Transactions on Biomedical Engineering* **58**: 1094-1103

[160] Ferdjallah M and Barr RE 1994 Adaptive digital notch filter design on the unit circle for the removal of powerline noise from biomedical signals *IEEE Trans. Biomed. Eng.* **41**: 529–36

[161] Fodor J and Roubens M 1994 Fuzzy Preference Modelling and Multicriteria Decision Support *Springer*

[162] Alste JA, Eck W and Herrmann OE 1986 ECG baseline wander reduction using linear phase filters, *Comput. Biomed. Res.* **19**: 417–27

[163] Ciarlini P and Barone P 1988 A recursive algorithm to compute the baseline drift in recorded biological signals *Comput. Biomed. Res.* **21**: 221–26

[164] Riccio ML and Belina JC 1992 A versatile design method off ast, linear-phase FIR filtering systems for electrocardiogram acquisition and analysis systems *Computers in Cardiology 1992 Proceedings* pp. 147–150.

[165] Bellanger M 2000 Digital Processing of Signals: Theory and Practice 3rd edition *New York: Wiley & Sons*

[166] Clifford GD, Lopez D, Li Q and Rezek I 2011 Signal Quality Indices and Data Fusion for Determining Acceptability of Electrocardiograms Collected in Noisy Ambulatory Environments *Computing in Cardiology* **38**: 285-8

[167] Pan J and Tompkins WJ 1985 A real-time QRS detection algorithm *IEEE Trans. Biomed. Eng.* **32**(3) : 230-6

[168] Xue Q and Reddy S 1998 Algorithms for computerized QT analysis *Journal of Electrocardiology* **30**: 181-6

[169] Mahmoud SS, Fang Q, Davidovic DM and Cosic I 2006 A Time-Frequency Approach for the Analysis of Normal and Arrhythmia Cardiac Signals *Proceedings of the 28th IEEE EMBS Annual International Conference New York City, USA, Aug 30-Sept 3, 2006*

[170] Xue Q, Hu YH and Tompkins WJ 1992 Neural-network-based adaptive matched filtering for QRS detection *IEEE Transactions on Biomedical Engineering* **39**: 317-29

[171] Gacek A and Pedrycz W 2003 A Genetic Segmentation of ECG Signals *IEEE Transactions on Biomedical Engineering* **50** 1203-1208

[172] Sahambi JS, Tandonz SN and Bhatt RKP 1997 Using Wavelet Transforms for ECG Characterization *IEEE Engineering in Medicine and Biology Magazine* **16**: 77-83

[173] Ghasemi M, Ghaffari A, SadAbadi H and Golbayani H 2010 QT interval measurement using RMED curve; a novel approach based on wavelet techniques *Comput Methods Biomech Biomed Engin*. **13**: 857-64

[174] Addison PS 2005 Wavelet transforms and the ECG: a review *Physiological Measurements* **26**: 155-99

[175] Lang WC and Forinash K 1998 Time-frequency analysis with the continuous wavelet transform *Am. J. Phys.* **66**: 9

[176] Jane R et al. 1997 Evaluation of an automatic threshold based detector of waveform limits in Holter ECG with the QT database *Computers in Cardiology* 295-8

[177] Spooner JT, Maggiore M, Ord R, and Passino KM 2002 Stable Adaptive Control and Estimation for Nonlinear Systems: Neural and Fuzzy Approximator Techniques *John Wiley and Sons, NY*

[178] Sivapathasekaran C, Mukherjee S, Ray A, Gupta A and Sen R 2010 Artificial neural network modeling and genetic algorithm based medium optimization for the improved production of marine biosurfactant *Bioresource Technology* **101**: 2884-7

[179] McBride J, Sullivan A, Xia H, Petrie A and Zhao X 2011 Reconstruction of physiological signals using iterative retraining and accumulated averaging of neural network models *Physiol Meas* **32**: 661-75

[180] Dastidar GS, Adeli H and Dadmehr N 2008 Principal Component Analysis-Enhanced Cosine Radial Basis Function Neural Network for Robust Epilepsy and Seizure Detection *IEEE Transactions on Biomedical Engineering* **55**: 512-18

[181] MathWorks Inc 1994-2012 http://www.mathworks.com/

[182] Moody BE 2011 A rule-based method for ECG quality control *Computing in Cardiology* **38**: 361–3

[183] Breiman L, Friedman JH, Olshen RA, Stone CJ 1984 Classification and Regression Trees *Belmont, Wadsworth International Group*

[184] Kligfield P, Gettes LS, Bailey JJ, et al. 2007 Recommendations for the standardization and interpretation of the electrocardiogram: a scientific statement from the American Heart Association; the American College of Cardiology Foundation; and the Heart Rhythm Society *Circulation* **115**: 1306-24.

[185] Levenberg K 1944 A Method for the Solution of Certain Non-Linear Problems in Least Squares *Quarterly of Applied Mathematics* **2**: 164–168

[186] Nielsen RH 1989 Theory of the backpropagation neural network *International Joint Conference on Neural Networks* **1**: 593-605

[187] Haykin S 1999 Neural Networks: A comprehensive Foundation *New Jersey, Prentice Hall*

[188] Stehman SV 1997 Selecting and interpreting measures of thematic classification accuracy *Remote Sensing of Environment* **62**: 77–89

[189] Powers DMW 2007 Evaluation: From precision, recall and f-factor to roc, informedness, markedness & correlation *Technical Report SIE-07-001, School of Informatics and Engineering, Flinders University, Adelaide, Australia*

[190] Jones KS 1972 A statistical interpretation of term specificity and its application in retrieval *Journal of Documentation* **28**: 11–21

[191] Altman DG and Bland JM 1994 Diagnostic tests 2: Predictive values *British Medical Journal* **309**: 102

[192] Alfaouri M and Daqrouq K 2008 Quality Evaluation Techniques of Processing the ECG Signal *American Journal of Applied Sciences* **5**: 1737-41

[193] Redmond SJ, Lovell NH, Basilakis J and Celler BG 2008 ECG quality measures in telecare monitoring *Conf Proc IEEE Eng Med Biol Soc.* 2869-72

[194] Hug C and Clifford GD 2007 An Analysis of the Errors in Recorded Heart Rate and Blood Pressure in the ICU Using a Complex Set of Signal Quality Metrics *Computers in Cardiology* **34**: 641-5

[195] Li Q, Mark RG and Clifford GD 2008 Robust heart rate estimation from multiple asynchronous noisy sources using signal quality indices and a Kalman filter *IOP Physiol. Meas.* **29**: 15-32

[196] Zaunseder S, Huhle R and Malberg H 2011 CinC Challenge – Assessing the Usability of ECG by Ensemble Decision Trees *Computing in Cardiology* **38**: 277-80

[197] Langley P, Marco LD, King S, Maria CD, Duan W, Bojarnejad M, Wang K, Zheng D, Allen J and Murray A 2011 An Algorithm for Assessment of ECG Quality Acquired Via Mobile Telephone *Computing in Cardiology* **38**: 281–4

[198] Noponen K, Karsikas M, Tiinanen S, Kortelainen J, Huikuri H and Seppänen T 2011 ECG Quality Classification based on Robust Best Subsets Linear Prediction Error *Computing in Cardiology* **38**: 365-8

[199] Hayn D, Jammerbund B and Schreier G 2011 Real-time Visualization of Signal Quality during Mobile ECG Recording *Computing in Cardiology* **38**: 353-6

[200] Moody GB 2010 The PhysioNet/Computing in Cardiology Challenge 2010: Mind the Gap, *Computing in Cardiology*, **37**: 305-308

[201] Harrigan RA 2006 Electrode misconnection, misplacement, and artifact *Emerg Med Clin North Am* **24**: 227-35

[202] Hoffman I 2008 A flatline lead I results from bilateral arm-to-leg electrode exchange *Journal of Electrocardiology* **41**: 388–90

[203] Bondy JA, Murty USR 2008 Graph Theory *New York, Springer*

[204] Newman M 2010 Networks: An Introduction *Oxford University Press*

[205] Hopcroft J, Tarjan R 1973Efficient algorithms for graph manipulation *Communications of the ACM* **16** (6): 372–378

[206] Gonzalez RC and Woods RE 2002 Digital Image Processing (2nd ed)

[207] Jolliffe I T2002 Principal Component Analysis, Series: Springer Series in Statistics, 2nd ed., *Springer, NY, XXIX, 487 p. 28 illus*

[208] Torrence C and Compo G P 1998 Practical Guide to Wavelet Analysis *American Meteorological Society*

[209] Wold S 1987 Principal component analysis *Chemometrics and Intelligent Laboratory Systems* **2**: 37–52

[210] Samorodnitsky G 1994 Stable Non-Gaussian Random Processes: Stochastic Models with Infinite Variance (Stochastic Modeling Series) *Chapman and Hall/CRC*; 1 edition

[211] Kullback S and Leibler RA 1951 On Information and Sufficiency *Annals of Mathematical Statistics* **22**(1): 79–86

[212] Jaynes ET 1957 Information Theory and Statistical Mechanics *Physical Review Series II* **106**(4): 620–630

[213] Joanes DN and Gill CA 1998 Comparing measures of sample skewness and kurtosis *Journal of the Royal Statistical Society (Series D): The Statistician* **47**(1): 183–189

[214] Brillouin L 1953 Negentropy Principle of Information *J. of Applied Physics* **24**(9): 1152-1163

[215] Press WH, TeukolskySA, Vetterling WT, Flannery BP 2007 Section 16.5.Support Vector Machines Numerical Recipes: The Art of Scientific Computing (3rd ed.) *New York: Cambridge University Press. ISBN 978-0-521-88068-8.*

[216] Cristianini N and Shawe J 2000 An Introduction to Support Vector Machines and Other Kernel-based Learning Methods *Cambridge University Press;* 1 edition

[217] Lukaszyk S 2004A new concept of probability metric and its applications in approximation of scattered data sets *Computational Mechanics* **33**: 299-3004

[218] Spring 2012 http://www.springsource.org/

[219] Graham I S 1995 The HTML Source Book *John Wiley & Sons, Inc. New York, NY, USA*

[220] Bibeault B and Katz Y 2008 jQuery in Action *Manning Publications Co. Greenwich, CT, USA*

[221] Fields D K, Kolb M A and Bayern S 2011 Web Development with Java Server Pages *Manning Publications Co. Greenwich, CT, USA*

[222] Chopra V, Li S, Genender J 2007 Professional Apache Tomcat 6 *John Wiley & Sons*

[223] Leff A. and Rayfield J.T. 2001 Web-application development using the Model/View/Controller design pattern *Enterprise Distributed Object Computing Conference, 2001. EDOC '01. Proceedings. Fifth IEEE International*

[224] Callegati F, Cerroni W and Ramilli M 2009 Man-in-the-Middle Attack to the HTTPS Protocol *Security & Privacy, IEEE* **7**: 78-81

[225] Physionet 2012 http://www.physionet.org/challenge/2012/

[226] Vincent JL, Moreno R, Takala J, Willatts S, De Mendonça A, Bruining H, Reinhart CK, Suter PM, Thijs LG 1996 The SOFA (Sepsis-related Organ Failure Assessment) score to describe organ dysfunction/failure. On behalf of the Working Group on Sepsis-Related Problems of the European Society of Intensive Care Medicine *Intensive Care Med* **22**(7):707-10

[227] Hosmer DW, Lemeshow S 2000 Applied Logistic Regression *New York : Wiley, ISBN 0-471-61553-6*

[228] Reed M, Simon B 1980 Methods of Modern Mathematical Physics: Functional analysis, Volume 1 *Academic Press*

[229] Percival DB, Walden AT 2006 Wavelet Methods for Time Series Analysis *Cambridge University Press*

[230] Wang GCS, Jain CL 2003 Regression Analysis: Modeling & Forecasting *Institute of Business Forec*

[231] McLachlan, G. J. 2005 Frontmatter, in Discriminant Analysis and Statistical Pattern Recognition *John Wiley & Sons, Inc., Hoboken, NJ, USA. doi: 10.1002/0471725293.fmatter*

[232] Safavian SR 1991 A survey of decision tree classifier methodology *IEEE Transactions on Systems, Man and Cybernetic*s **21**: 660-74

[233] Mittal A and Kassim A 2007 Bayesian Network Technologies: Applications and Graphical Models *Idea Group Inc (IGI)*

[234] Rosenblatt M 1956 Remarks on some nonparametric estimates of a density function *Annals of Mathematical Statistics* **27**: 832–837

[235] Gori M and Tesi A 1992 On the Problem of Local Minima in Backpropagation *IEEE Transactions on Pattern Analysis and Machine Intelligence archive* 14(1): 76-86

[236] Prechelt L 1998 Automatic early stopping using cross validation: quantifying the criteria *Neural Networks* 11(4): 761–767

[237] Ng AY 1997 Preventing "Overfitting" of Cross-Validation Data *Proceedings of the Fourteenth International Conference on Machine Learning* Pages 245 – 253

[238] Chawla NV, Bowyer KW, Hall LO and Kegelmeyer WP SMOTE: Synthetic Minority Over-sampling Technique *Journal of Artificial Intelligence Research* **16**: 321-357

# VITA

Henian Xia was born in Chaohu, China. He graduated in July 2008 with a Bachelor of Engineering Degree in Electrical Engineering from the University of Science and Technology of China. In August 2008, he began his graduate studies in the department of Mechanical, Aerospace and Biomedical Engineering at the University of Tennessee, in Knoxville, Tennessee, where he was directed by Dr. Xiaopeng Zhao. His research and coursework were in the areas of Biomedical Signal Processing, Computational Biology, Mathematical Modeling, Machine Learning, Parallel Computing, and Finite Element.